The QED coupling at the Z pole and jet studies of small χ dynamics

Outhwaite, John

The QED coupling at the Z pole and jet studies of small x dynamics.

A thesis presented for the degree of

Doctor of Philosophy

by

John Outhwaite

Physics Department

University of Durham

December 2000

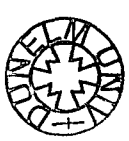

Abstract

In the first half of this thesis, motivated by significant progress in both theoretical and empirical studies of e^+e^- annihilation into hadrons, we perform a reevaluation of the running of the QED coupling to the Z-pole, paying particular attention to the hadronic contribution to vacuum polarization. We use a comprehensive collection of the presently available data and perturbative QCD expressions.

This new determination of the running of the coupling is then used as input into a global fit to electroweak data to estimate a preferred value of the Standard Model Higgs boson. An estimate is obtained of $M_H = 110$ GeV, marginally above the zone excluded by direct searches at LEP2.

We then investigate the potential for further constraining the hadronic contribution to the vacuum polarization function through mechanisms incorporating analytic continuation from the timelike domain of $s > 0$ around a large semicircle into the spacelike domain of $s < 0$. Intrinsic sensitivity in the QCD description to the pole masses force us to conclude there is no advantage to be gained in comparison with the direct timelike estimation, although by demanding consistency between the complementary approaches we can both generate an estimate of the charm mass and elucidate low energy data ambiguities, finding a preferred value of $m_c = 1.4$.

In the latter half of the thesis, we examine forward jet and pion production in electron - proton deep inelastic scattering in the small x region of the HERA collider at DESY. We demonstrate the imposition of physically motivated dominant subleading corrections to all orders on the leading logarithmic BFKL equation, and that this leads to stable phenomenological predictions.

We compare the calculations of differential cross-section distributions incorporating the higher order effects with the experimental profiles for a single jet, an identified π^0 and dijets in the very forward region and investigate the sensitivity of the calculation to residual parametric freedom.

Declaration

I declare that no material presented in this thesis has previously been submitted for a degree at this or any other university.

The work described in this thesis has been carried out in collaboration with Professors A.D. Martin, J. Kwieciński and M.G. Ryskin. The journal publications which correspond to the material in Chapters 1 and 2 are

- *The R ratio in e^+e^-, the determination of $\alpha(M_Z^2)$ and a possible non-perturbative gluonic contribution.*
  A.D. Martin, J. Outhwaite, M.G. Ryskin, J. Phys. **G26** (2000) 600
- *A new determination of the QED coupling $\alpha(M_Z^2)$ lets the Higgs off the hook.*
  A.D. Martin, J. Outhwaite, M.G. Ryskin, Phys. Lett. **B492** (2000) 69
- *Improving $\alpha(M_Z^2)$ and the charm mass by analytic continuation*
  A.D. Martin, J. Outhwaite, M.G. Ryskin, in preparation.

Publications associated with the material in Chapters 4, 5 and 6 are

- *Small x QCD effects in DIS with a forward jet or a forward π^0.*
  J. Kwieciński , A.D. Martin and J. Outhwaite, Eur. Phys. J. **C9** (1999) 611
- *Forward jet production as a probe of low x dynamics.*
  J. Outhwaite, *In Tegernsee 1999, New trends in HERA physics 111-123.*
- *Azimuthal decorrelation of forward and backward jets at the TEVATRON.*
  J. Kwieciński , A.D. Martin and J. Outhwaite, in preparation.

Acknowledgements

I must first express my profound gratitude to my supervisor, Professor Alan Martin, and his colleagues, Professors Jan Kwieciński and Misha Ryskin who collectively have coaxed me through the pitfalls of perturbative QCD with characteristic good grace and inexhaustible patience.

I think many others could lay an honest claim to inclusion in a litany of gratitude for making my postgraduate Durham incarnation as fulfilling an experience as it has been, but an exhaustive list seems self-indulgent. In lieu of comprehensiveness, I'll simply extend thanks to everyone - you'll know if you merit it, and single out four groups of people deserving of particular praise...

Firstly, many thanks individually to Matt Szyndel, erstwhile partner in crime, Neil Smart, compatriot old boy in north-eastern exile, Magnus Bebbington, fellow disciple of the gentle way, and Lou Watkinson who have each, in their own inimitable fashions, enriched my time here more than my words do justice to.

Next, I must heartily thank my friends of office 307 - Physics couldn't have been the same without the whimsical discussions, melodic humming or office cricket during those distant halcyon days - so collectively to Matt Cullen, Ania Kulesza and Pete Watson, I'm finally catching up!

Thirdly, an en masse thanks to everyone who has trained with me at Durham University Judo Club in the last few years, and who have endured my self-proclaimed reign of tyranny and questionable coaching abilities without (too much) question - always choose the way of the Chosi-waza, and I hope the future proves fruitful for you all.

Finally, I wouldn't find myself in the position I am now without the constant encouragement of my family, Mum, Dad and Kate, who have stoically endured the lows and ceded the limelight for the highs with the same unwavering care and support - thank you.

Die Welt ist alles, was der Fall ist. *L. Wittgenstein*

Contents

Chapter 1

Determination of the QED coupling

In this chapter we examine the charge screening phenomenon of Quantum Electrodynamics and in particular the hadronic contribution, which is in principle given by Quantum Chromodynamics. We qualitatively introduce the concepts involved, and subsequently describe the theoretical machinery which is used to quantitatively enumerate their physics content. By appealing to certain fundamental properties of scattering theory, we are able to circumvent the need for QCD calculations in intrinsically non-perturbative domains through the use of dispersion relations, which require us to implement an interpolation through data for the famous R-ratio. We present an up-to-date compilation of the available data, and illustrate how disparate data sets are most effectively amalgamated to minimize their collective error. Moreover, in the regions where we can be assured of the safety of a perturbative approach, we present the most sophisticated $\mathcal{O}(\alpha_s^3)$ QCD description of the vacuum polarization, which permits a dramatic reduction in the global uncertainty. We contrast this reevaluation of the running QED coupling to a benchmark standard in order to discuss explicitly the improvements manifest in this determination. The chapter concludes with a brief resumé of the minimal Standard Model Higgs mechanism, and the ramifications for this of the current reevaluation.

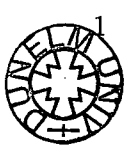

1.1 Vacuum polarization and the fine structure constant

Within the framework of a quantum field theory (for introductory texts see [1, 2]) we are no longer entitled to treat any constituent object as a simple isolated entity. In particular, for the example of an electrically charged particle, we allow the possibility of the creation of virtual particle anti-particle pairs, through the emission and subsequent annihilation of a spontaneously generated photon. The act of dressing the vacuum in this manner alters its role from a classically passive arena to a dynamic participant in all physical processes. A new picture arises of the vacuum as a pseudodielectric medium bubbling with a maelstrom of virtual particles. Qualitatively, the electrically charged particle pairs position themselves as oriented dipoles, which have the effect of shielding the bare charge from an experimental probe. The electric charge that is observed will increase with the extent to which an experiment, ultimately characterized by the behaviour of a proximal test charge, penetrates the cloud. The phenomenon is known as *vacuum polarization*, and its effects feed into a wide variety of electroweak processes, from radiative corrections to indirect constraints on the mass of unseen heavy particles.

We are able to specify the electroweak sector of the Standard Model [3] with three parameters, which are usually taken to be $G_F = 1.16637(1) \cdot 10^{-5}$ GeV^{-2}, the Fermi coupling constant, determined from the muon lifetime formula [4], $M_Z = 91.1872(21)$ GeV, the mass of the Z^0 boson, extracted from the Z lineshape scan at LEP 1 [5], and the least well known of the three, the quantum electrodynamic (QED) coupling at the Z-pole, $\alpha(M_Z^2)$, whose determination and uncertainty we shall be concerned with in this chapter.

Precision tests of the electroweak sector demand that these parameters are known as accurately as possible, so a precise evaluation of the comparatively ill-known magnitude of the vacuum polarization is of paramount importance for phenomenological applications. We shall present a brief discussion, [2], of the machinery by which we enumerate the physics encompassed by the phenomenon. A *vacuum polarization amplitude*, $\Pi^{\mu\nu}(q)$, is defined to quantify this effect, it is the Fourier transform of the contraction of the electromagnetic currents $j^{\mu}(q^2)$ in the vacuum,

$$\Pi^{\mu\nu}(q) = i \int d^4x e^{iq\cdot x} \langle 0|T j^{\mu}(x) j^{\nu}(0)|0\rangle.$$

The tensor structure of the two-point function can be extracted generally from those quantities

available to us, $q^\mu q^\nu$ and the spacetime metric $g^{\mu\nu}$. We write the vacuum polarization amplitude as this generic tensor with a non-singular scalar function $\Pi(q^2)$, of the Lorentz invariant square of the four-momentum, factored out,

$$\Pi^{\mu\nu}(q) = \left(q^2 g^{\mu\nu} - q^\mu q^\nu\right)\Pi(q^2). \tag{1.1}$$

The *exact* photon two-point function illustrated by the 'blob' below is now given by a sum of serially coupled one particle irreducible[1] graphs, inserted in the photon propagator in series,

we then explicitly perform and sum over these insertions (1.1) into the photon propagator factor, $-\frac{ig_{\mu\nu}}{q^2}$ (in the Feynman gauge), to obtain an expression for the exact propagator, which can be expressed as a power series in the polarization function, $\Pi(q^2)$. This is resummed by taking it into the denominator,

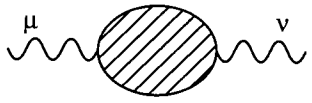

$$\begin{aligned} &= -\frac{ig_{\mu\nu}}{q^2} - \frac{ig_{\mu\rho}}{q^2}\left(\delta^\rho_\nu - \frac{q^\rho q_\nu}{q^2}\right)\left(\Pi(q^2) + \Pi^2(q^2) + ...\right) \\ &= \frac{-i}{q^2\left(1-\Pi(q^2)\right)}\left(g_{\mu\nu} - \frac{q_\mu q_\nu}{q^2}\right) - \frac{i}{q^2}\left(\frac{q_\mu q_\nu}{q^2}\right). \end{aligned}$$

Appealing to the Ward identity, $q\cdot\Pi = 0$, which is an expression of current conservation, enables this last expression to be simplified. We recognize that in any physical calculation, the photon propagator must terminate with a fermion line, and the identity then guarantees that any part of the propagator proportional to q^μ or q^ν will vanish identically. In the context of a practical calculation, we are at liberty to unilaterally discard these terms from the start, which leaves a complete propagator of the form,

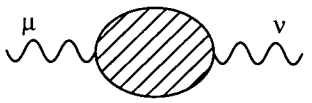

$$= \frac{-ig_{\mu\nu}}{q^2}\frac{1}{[1-\Pi(q^2)]},$$

which has a pole at $q^2 = 0$ with residue $\dfrac{1}{1-\Pi(q^2)}$. The bare charge parameter, e_0, is then reparameterized in terms of the measured charge e, and the full photon propagator then reads

$$-\frac{ig_{\mu\nu}}{q^2}\frac{e_0^2}{[1-\Pi(q^2)]} = -\frac{ig_{\mu\nu}}{q^2}\frac{e^2}{[1-\{\Pi(q^2)-\Pi(0)\}]}. \tag{1.2}$$

[1]One particle irreducible (1PI) graphs are those which cannot be bisected by removing a single line.

The strength of the QED coupling at an energy scale $s = q^2$ is related to the long wavelength Thomson limit, where it is known rather precisely [6], $\alpha = 1/137.03599976(50)$, via the innocuous looking expression

$$\alpha(s) = \frac{\alpha}{1 - \Delta\alpha(s)}, \tag{1.3}$$

where the function $\Delta\alpha(s)$, describing the shift in the fine structure constant with energy scale, is evaluated from the real part of the vacuum polarization function, and a constant $4\pi\alpha$ is factored out by convention,

$$\Delta\alpha(s) = -4\pi\alpha \left\{\Pi(s) - \Pi(0)\right\} = -4\pi\alpha \mathrm{Re}\hat{\Pi}(s). \tag{1.4}$$

We should distinguish between the contributions of virtual lepton pair production, e^+e^-, $\mu^+\mu^-$ and $\tau^+\tau^-$, and virtual $q\bar{q}$ production whose participants carry the additional quantum number of *colour* and whose behaviour is radically modified by quantum chromodynamical (QCD) effects in comparison with the leptonic case. The shift in the fine structure constant is then naturally subdivided into contributions arising from strictly leptonic effects from the physics of QED, $\Delta\alpha_{\mathrm{lep}}(s)$, and hadronic contributions arising from the physics of QCD. The latter are further partitioned into $\Delta\alpha^{(5)}_{\mathrm{had}}(s)$, the piece from the first 5 quark flavours, and a part from the rather massive top quark ($m_t \simeq 174$ GeV), denoted $\Delta\alpha^{\mathrm{top}}_{\mathrm{had}}(s)$. These are the full set of contributions that the Standard Model allows for, and so the complete decomposition of corrections to $\Delta\alpha(s)$ reads:

$$\Delta\alpha(s) = \Delta\alpha_{\mathrm{lep}}(s) + \Delta\alpha^{(5)}_{\mathrm{had}}(s) + \Delta\alpha^{\mathrm{top}}_{\mathrm{had}}(s). \tag{1.5}$$

The scale dependence or *running* of the QED coupling is conventionally quantified by the magnitude of the shift at the Z-pole, $s = M_Z^2$, which is the most appropriate scale for precision electroweak tests. At these energies the strength of the (somewhat misnomered) fine structure constant increases by about 6% from its long wavelength Thomson limit of $\alpha(0) \simeq 1/137$ to $\alpha(M_Z^2) \simeq 1/129$. We illustrate a typical spread of evaluations of $\alpha^{-1}(M_Z^2)$ by a variety of authors below. The principle cause of the variation in central values and errors will prove to be the ill known hadronic contribution to the vacuum polarization, which we discuss later.

$\alpha^{-1}(M_Z^2)$	Group
128.99 ± 0.06	Martin, Zeppenfeld, [7].
128.896 ± 0.090	Eidelman, Jegerlehner, [8].
128.927 ± 0.023	Kühn, Steinhauser, [9].
128.923 ± 0.036	Davier, Höcker, [10].

1.2 Leptonic contribution to vacuum polarization

We use the Feynman rules of QED (for examples see [2]) to calculate the $\mathcal{O}(\alpha)$ leptonic (e, μ, and τ) contribution to the vacuum polarization function, $\hat{\Pi}_l(q^2)$. The fermion one loop insertion into the photon propagator has the following form:

$i\Pi_l^{\mu\nu}(q) =$ 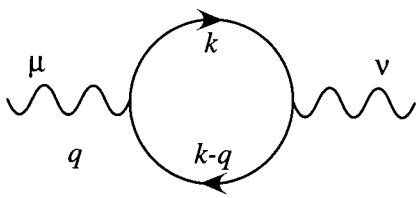

$= -(-ie)^2 \int \frac{d^4k}{(2\pi)^4} \mathrm{Tr}\left[\gamma^\mu \frac{i}{\not{k} - m_l} \gamma^\nu \frac{i}{\not{k} + \not{q} - m_l}\right],$

with m_l the lepton mass, q^μ the four-momentum of the photon propagator, k^μ the circulating loop momentum and γ^μ the Dirac-γ matrices. The diagram contains two QED vertex factors, $ie\gamma^\mu$, which connect the external photon lines to the fermion loop propagators. The presence of the loop generates an additional factor -1, and we use the standard 'slash' notation, $\not{k} = \gamma^\mu k_\mu$. The loop momentum can in principle take any value and is integrated over.

Orthodox trace machinery expands this expression,

$$i\Pi_l^{\mu\nu}(q) = -4e^2 \int \frac{d^4k}{(2\pi)^4} \frac{k^\mu(k+q)^\nu + k^\nu(k+q)^\mu - g^{\mu\nu}\left(k\cdot(k+q) - m_l^2\right)}{(k^2 - m_l^2)\left((k+q)^2 - m_l^2\right)}$$

We can tidy the denominator factors into a form amenable for further manipulation by implementing Feynman parameters, We introduce an auxiliary variable, x, such that we are able to complete the square of the denominator, which will allow us to perform the integration over k,

$$\frac{1}{(k^2 - m_l^2)\left((k+q)^2 - m_l^2\right)} = \int_0^1 dx \frac{1}{\left(k^2 - 2xk\cdot q + xq^2 - m_l^2\right)^2} = \int_0^1 dx \frac{1}{\left(l^2 + x(1-x)q^2 - m_l^2\right)^2},$$

with the loop momentum shifted by $l = k + xq$. After explicitly factoring out the tensor structure of (1.1), we Wick rotate the expression into Euclidean space, $l^0 \to il_E^0$, and then treat the resulting integral in $4 - \varepsilon = d$-dimensional space which regulates the ultraviolet divergence.

After this integration technology has been implemented, an integral expression for the vacuum polarization function is obtained, with the ultraviolet divergence rendered explicit as a pole in ε,

$$\Pi_l(q^2) = \lim_{\varepsilon\to 0} -\frac{2\alpha}{\pi}\int_0^1 dx x(1-x)\left\{\frac{2}{\varepsilon} - \log\left(m_l^2 - x(1-x)q^2\right) - \gamma_\epsilon\right\}, \tag{1.6}$$

with $\gamma_\epsilon \simeq 0.577$ the Euler-Mascheroni constant. This integral remains divergent, but if a subtraction is performed at the long wavelength limit, $\Pi(0)$, the poles in ε cancel, and we are left with a convergent quantity independent of $\varepsilon = d-4 \to 0$. The physics lies in the q^2 dependence of the effective charge, which is (happily) well defined in the limit of four spacetime dimensions,

$$\hat{\Pi}_l(q^2) = \left\{\Pi_l(q^2) - \Pi_l(0)\right\} = -\frac{2\alpha}{\pi}\int_0^1 dx x(1-x)\log\left(\frac{m_l^2}{m_l^2 - x(1-x)q^2}\right). \tag{1.7}$$

This is a standard integral [11] which provides a final solution to $\mathcal{O}(\alpha)$ with the form (setting $q^2 = s$),

$$\hat{\Pi}_l(s) = -\frac{1}{9}\frac{\alpha}{\pi}\left\{5 + 12\frac{m_l^2}{s} - 3\left(1+2\frac{m_l^2}{s}\right)\left(1-4\frac{m_l^2}{s}\right)^{1/2}\log\left[\frac{(1-4m_l^2/s)^{1/2}+1}{(1-4m_l^2/s)^{1/2}-1}\right]\right\}. \tag{1.8}$$

The solution has a branch cut which manifests itself when the denominator function in the logarithm becomes negative, that is, at $s = 4m_l^2$, the threshold for production of a real lepton anti-lepton pair.

Using Eqn. (1.4) we can now evaluate the contribution to vacuum polarization at leading order in α arising from the electron, muon and tau lepton loops. The Particle Data Group [6] give lepton masses of 0.511 MeV, 105.658 MeV and 1.777 GeV for m_e, m_μ and m_τ respectively, which upon substituting into (1.8) and implementing (1.4), we find,

$$\Delta\alpha_e^{(1)}(M_Z^2)\cdot 10^4 = 174.35,\ \ \Delta\alpha_\mu^{(1)}(M_Z^2)\cdot 10^4 = 91.78 \text{ and } \Delta\alpha_\tau^{(1)}(M_Z^2)\cdot 10^4 = 48.06.$$

The two loop $\mathcal{O}(\alpha^2)$ term for the leptonic contribution to vacuum polarization has also been calculated [12]. Although quite small, it may prove to be a significant shift for precision tests of the electroweak sector of the Standard Model, and should be included. Evaluated at $s = M_Z^2$ it reads,

$$\Delta\alpha_{\rm lep}^{(2)}(M_Z^2) = \left(\frac{\alpha}{\pi}\right)^2 \sum_{l=e,\mu,\tau}\left\{-\frac{5}{24} + \zeta(3) + \frac{1}{4}\log\frac{M_Z^2}{m_l^2} + 3\frac{m_l^2}{M_Z^2}\log\frac{M_Z^2}{m_l^2} + \mathcal{O}\left(\frac{m_l^4}{M_Z^4}\right)\right\}, \tag{1.9}$$

and numerically gives a spectrum of two loop leptonic contributions reading

$$\Delta\alpha_e^{(2)}(M_Z^2)\cdot 10^4 = 0.38,\ \ \Delta\alpha_\mu^{(2)}(M_Z^2)\cdot 10^4 = 0.24 \text{ and } \Delta\alpha_\tau^{(2)}(M_Z^2)\cdot 10^4 = 0.17,$$

for the electron, muon and tau respectively. Ultimately we find a net leptonic contribution to the shift in the fine structure constant at the Z-pole, $\Delta\alpha_{\text{lep}}(M_Z^2)\cdot 10^4$, of 314.98.

1.3 Hadronic contribution to vacuum polarization

It is not possible in an analogous way to calculate the hadronic contribution generally - at low energies and around quark-antiquark bound states strong QCD interactions render a perturbative approach inapplicable. Fortunately, appealing to analyticity within QCD enables us to circumvent these inconveniences and substitute for an explicit calculation low energy data and parameterizations where the perturbative approach becomes unreliable. We now introduce the technical apparatus necessary to investigate the hadronic contribution, namely the *optical theorem* and *dispersion relations.*

1.3.1 The optical theorem

The optical theorem relates the imaginary part of a forward (s-channel) scattering amplitude to the total cross-section. We can show this by appealing to another property of scattering theory - the unitarity of the S-matrix. The S-matrix is a limiting unitary operator that transforms a set of incoming states, $|k_1 k_2 ...\rangle$ to a set of outgoing states, $|p_1 p_2 ...\rangle$,

$$\langle p_1 p_2 ... | S | k_1 k_2 ... \rangle.$$

The T-matrix is defined as that part of the S-matrix containing information purely on the scattering interaction. We choose to decompose the S-matrix in terms of a T-matrix in the following manner, $S = \mathbf{1} + iT$, allowing for the possibility that the in and out states fail to interact with one another. The unitarity condition, $SS^\dagger = \mathbf{1}$, then implies the following relation between T and $T^\dagger$,

$$-2i\text{Im}\ T = -i(T - T^\dagger) = TT^\dagger.$$

For the purposes of investigating the vacuum polarization, it is instructive to consider the matrix element between two identical electron-positron states, $\langle k_1 k_2 | TT^\dagger | k_1 k_2 \rangle$, corresponding to the generic graph depicted in Fig. 1.1. We can expand this in terms of the invariant matrix elements[2];

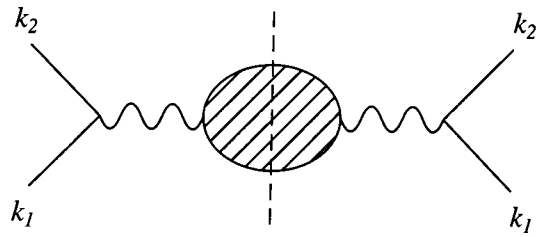

Figure 1.1: Optical theorem in e^+e^- annihilation: By cutting the central blob representing all possible intermediate states across the dashed line, we are able to relate the imaginary part of the forward scattering amplitude to the total cross-section for hadronic production.

$\mathcal{M}$, factoring out information regarding the simple kinematics of the scattering and explicitly imposing energy-momentum conservation in the δ function. Upon the insertion of a complete set of intermediate particle states we obtain,

$$2\mathrm{Im}\mathcal{M}(k_1 k_2 \to k_1 k_2) = \sum_n \left(\prod_{i=1}^{n} \int \frac{d^3 q_i}{(2\pi)^3} \frac{1}{2E_i} \right) \mathcal{M}^* \left(k_1 k_2 \to \{q_i\}\right) \mathcal{M} \left(k_1 k_2 \to \{q_i\}\right) (2\pi)^4 \delta^{(4)} \left(k_1 + k_2 - \sum_i q_i \right).$$

Now supplying the correct kinematical factors for e^+e^- scattering, we formulate the optical theorem in concise manner,

$$\mathrm{Im}\mathcal{M}(k_1 k_2 \to k_1 k_2) = 2E_{\mathrm{cm}} p_{\mathrm{cm}} \sigma_{\mathrm{tot}}(k_1 k_2 \to \mathrm{hadrons}), \tag{1.10}$$

with E_{cm} and p_{cm} are the centre-of-momentum frame energy and momentum of the system respectively. In terms of the vacuum polarization function, $\Pi(s)$, related to the invariant matrix element through

$$i\mathcal{M} = (-ie)^2 \bar{u}(k_1)\gamma_\mu v(k_2) \frac{-i}{s} \left[i\hat{\Pi}^{\mu\nu}(q^2) \right] \frac{-i}{s} \bar{v}(k_2)\gamma_\nu u(k_1),$$

we obtain a form of the optical theorem which will prove particularly useful in the forthcoming analysis,

$$12\pi \mathrm{Im}\hat{\Pi}(s) = \frac{\sigma_{\mathrm{tot}}(e^+e^- \to \mathrm{hadrons})}{\sigma_{\mathrm{tot}}(e^+e^- \to \mu^+\mu^-)} = R(s). \tag{1.11}$$

[2]Where $\mathcal{M}$ is defined by the relation $\langle p_1 p_2 | iT | k_1 k_2 \rangle = (2\pi)^4 \delta^{(4)} (k_1 + k_2 - p_1 - p_2)\, i\mathcal{M}(k_1 k_2 \to p_1 p_2)$.

It transpires that a perturbative QCD calculation of the total cross-section is asymptotic, in the high energy limit, to the cross-section for pointlike muon pair production, $e^+e^- \to \mu^+\mu^-$. In order to better resolve effects arising solely from QCD physics we factor out of the total cross-section the asymptotic limit, $\sigma_{\mu^+\mu^-} = 4\pi\alpha^2/3s$.

In synopsis of the previous section, basic precepts of scattering theory allow us to specify the absorptive part of the photon vacuum polarization by reference to the total cross-section for hadron production in e^+e^- annihilation. This is a particularly useful piece of information - there is a rich catalogue of annihilation data in existence from many experimental collaborations throughout the energy interval, $2m_\pi < \sqrt{s} \lesssim 40$ GeV, that is, from threshold for pion production to high energies where we can be assured of asymptotic freedom and the validity of perturbative QCD.

1.3.2 Dispersion relations

The vacuum polarization function, $\Pi(s)$, is a real valued function on the real axis beneath some threshold for production $s = M^2$, and possesses a branch cut along the real line above this point, $s > M^2$. It is otherwise an analytic function order-by-order in perturbation theory. If we permit complex values of the centre-of-mass energy squared, s, and analytically *continue* Π across the complex plane, we can exploit the powerful machinery of complex analysis to specify the complete polarization function from information of the behaviour of its imaginary part along the branch cut. The absorptive part of Π along the cut is specified by

$$\Pi(s + i\epsilon) = \mathrm{Re}\Pi(s) + i\mathrm{Im}\Pi(s),$$

with $\epsilon > 0$ an infinitesimal displacement away from the real s axis. Schwarz' reflection principle then allows us to write the imaginary part of the vacuum polarization as the difference between two such displacements

$$\Pi(s + i\epsilon) - \Pi(s - i\epsilon) = 2i\mathrm{Im}\Pi(s).$$

As Π is an analytic function in the complex s-plane (except for the branch cut along the real axis) we now use the Residue theorem[3], taking the contour of integration C illustrated in Fig. 1.2,

[3]Which states that the integral of a complex function, analytic other than at a finite number of poles within the contour of integration, is given by $2\pi i$ times the sum of those poles.

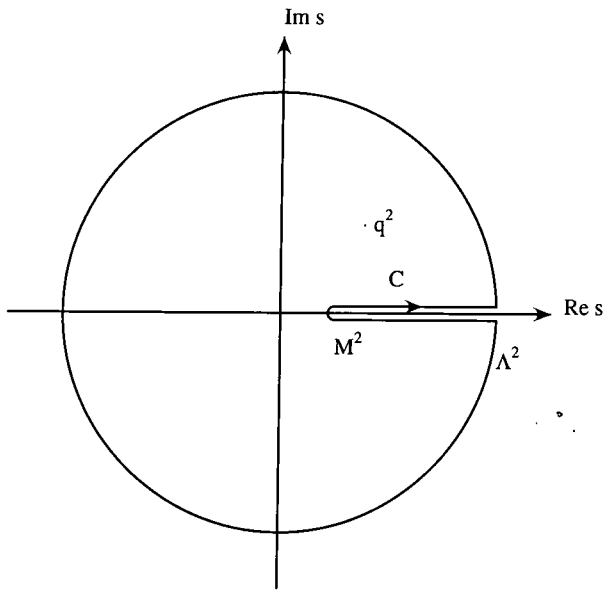

Figure 1.2: Contour of integration, C, in the complex s-plane, for use in the Residue theorem.

within the interior of which our vacuum polarization function is completely analytic for all q^2. We have deformed the contour away from the branch cut, and complete it around the large arc $|s| = \Lambda^2$, and anticipate sending $\Lambda^2 \to \infty$. Weighting Π with a simple pole $\frac{1}{s-q^2}$ creates an artificial singularity within the contour which we can exploit.

An expression for the function $\Pi(q^2)$ in terms of the weighted integral of its imaginary part along the branch cut, and a contour integral around $|s| = \Lambda^2$, is readily obtained,

$$\Pi(q^2) = \frac{1}{2\pi i}\oint_C ds \frac{\Pi(s)}{s-q^2} = \frac{1}{\pi}\int_{M^2}^{\Lambda^2} ds \frac{\mathrm{Im}\Pi(s)}{s-q^2-i\epsilon} + \frac{1}{2\pi i}\oint_{|s|=\Lambda^2} ds \frac{\Pi(s)}{s-q^2}. \qquad (1.12)$$

The goal is to make this latter piece vanish as Λ becomes large. Vacuum polarizations have the dimensions of M^2, so that the second contour integral is not assured of tending to zero in general. By performing a *second* such dispersion relation at the reference point q_0^2, we obtain the *once subtracted* dispersion relation

$$\left\{\Pi(q^2) - \Pi(q_0^2)\right\} = \frac{q^2-q_0^2}{\pi}\int_{M^2}^{\Lambda^2} \frac{ds}{s-q_0^2}\frac{\mathrm{Im}\Pi(s)}{(s-q^2-i\epsilon)} + \frac{q^2-q_0^2}{2\pi i}\oint_{|s|=\Lambda^2} \frac{ds}{s-q_0^2}\frac{\Pi(s)}{(s-q^2)}, \qquad (1.13)$$

where the integral around the large circle is suppressed by a further s factor at large $|s|$ and so *will* vanish as $\Lambda \to \infty$.

In particular for the photon vacuum polarization function, which in the conventional QED scheme is subtracted at the long wavelength reference point $\Pi(q_0^2 = 0)$, we can determine the behaviour of the dispersive part of $\hat{\Pi}$ from a weighted integral of its absorptive part.

$$\mathrm{Re}\left\{\Pi(q^2) - \Pi(0)\right\} = \mathrm{Re}\hat{\Pi}(q^2) = \frac{q^2}{\pi}\mathcal{P}\int_{M^2}^{\infty}\frac{ds}{s}\frac{\mathrm{Im}\hat{\Pi}(s)}{(s-q^2)} \tag{1.14}$$

where $\mathcal{P}$ is used to denote the Cauchy principle value given by,

$$\mathcal{P}\int_{x_a}^{x_b} dx\frac{f(x)}{x-x_0} = \lim_{\varepsilon\to 0}\left\{\int_{x_a}^{x_0-\varepsilon} dx\frac{f(x)}{x-x_0} + \int_{x_0+\varepsilon}^{x_b} dx\frac{f(x)}{x-x_0}\right\},$$

for $x_a < x_0 < x_b$.

Using the result from the optical theorem, (1.11), we obtain a dispersion relation connecting the real part of the vacuum polarization amplitude to the total cross-section for hadronic production in e^+e^- annihilation [13, 14],

$$\Delta\alpha^{(5)}_{\mathrm{had}}(q^2) = -4\pi\alpha\mathrm{Re}\ \hat{\Pi}(q^2) = -\frac{\alpha q^2}{3\pi}\mathcal{P}\int_{M^2}^{\infty}\frac{ds}{s}\frac{\mathrm{R}(s)}{(s-q^2)}. \tag{1.15}$$

The integral is weighted by a denominator of $s(s-q^2)$, such that the cross-section at low s will prove comparatively more significant than the suppressed high energy tail.

Finally, we note that the lower limit of integration, corresponding to the onset of hadron production, lies at the physical threshold for pion production in e^+e^- annihilation, that is, $M^2 = 4m_\pi^2$ where $m_\pi \simeq 0.14$ GeV.

1.4 Perturbative QCD calculation of the R-ratio

Asymptotic freedom allows the vacuum polarization function to be evaluated as a perturbative expansion in the running strong coupling, $\alpha_s(\mu^2)$, given (at three loops) by the expression

$$\frac{\alpha_s(\mu^2)}{\pi} = \frac{1}{\beta_0 L}\left\{1 - \frac{1}{\beta_0 L}\frac{\beta_1\log L}{\beta_0} + \frac{1}{\beta_0^2 L^2}\left[\frac{\beta_1^2}{\beta_0^2}\left(\log^2 L - \log L - 1 + \frac{\beta_2}{\beta_0}\right)\right]\right\}, \tag{1.16}$$

where $L = \log\left(\mu^2/\Lambda^2_{\overline{\mathrm{MS}}}\right)$ and $\Lambda_{\overline{\mathrm{MS}}}$ is the scale at which the coupling becomes 'large', determined in the $\overline{\mathrm{MS}}$ scheme, [15]. The β function coefficients are given by $\beta_0 = (11 - \frac{2}{3})/4$, $\beta_1 = (102 - \frac{38}{3}n_f)/16$ and $\beta_2 = (\frac{2857}{2} - \frac{5033}{18}n_f + \frac{325}{54}n_f^2)/64$. The running strong coupling

exhibits *asymptotic freedom*, $\alpha_s \to 0$ (though slowly) as $\mu^2 \to \infty$, that is, the coupling becomes small for *short-distance* interactions, making it an appropriate expansion parameter.

The generic form for a perturbative expansion made by each participating quark flavour q is written

$$\hat{\Pi}_q(s) = \sum_i \left(\frac{\alpha_s(\mu^2)}{\pi}\right)^i \hat{\Pi}_q^{(i)}\left(s, \mu^2, m_q^2\right),$$

where m_q is the quark mass parameter. At both one and two loop level, which have a pseudo-Abelian structure, the complete mass dependence of $\hat{\Pi}_q^{(0)}$ [12] and $\hat{\Pi}_q^{(1)}$ [16] has been explicitly calculated. The three loop function $\hat{\Pi}_q^{(2)}$ obtains contributions from graph topologies unique to non-Abelian theories, in particular, those containing triple gluon vertices and gluon loops. It has a mass dependence which is known both as a high energy expansion in m_q^2/s, and at low energies as an expansion in s/m_q^2, [17, 18], allowing a reconstruction of its behaviour through threshold. Contributions to absorptive pieces of $\hat{\Pi}_q$ in the approximation of massless quarks are known to $\mathcal{O}(\alpha_s^3)$, [19].

Using the optical theorem of (1.11) the vacuum polarization function is related to the cross-section for the production of hadrons in e^+e^- annihilation, we have a structurally similar expansion in α_s,

$$R_q(s) = \sum_i \left(\frac{\alpha_s(\mu^2)}{\pi}\right)^i R_q^{(i)}\left(s, \mu^2, m_q^2\right), \tag{1.17}$$

and the complete contribution made by the quarks is given by summing over the flavours active at a particular value of s, $R(s) = \sum_q R_q(s)$. We explicitly recover the R-ratio as a mass expansion - as we substitute the region of quark thresholds with data, we need not maintain the complete mass-dependence. As the mass dependence is known to $\mathcal{O}\left([m_q^2/s]^2\right)$, this is sufficiently convergent to allow a perturbative calculation of R to approach quite near to threshold [20].

1.4.1 One loop vacuum polarization and the R-ratio

The QCD tree-level contribution to the vacuum polarization function is well known [12]. It is simply the contribution to $\hat{\Pi}$ from a virtual $q\bar{q}$ pair, that is, the basic fermion loop we went to some pains to explicitly calculate in Section 1.2. By inserting the appropriate colour factor, $N_c = 3$, and using the charge of the participating quark flavour, $e \to |e|Q_q$, we directly obtain

the necessary expression from Eqn. (1.8). For brevity of notation writing $z = 4m_q^2/s$, we have

$$\hat{\Pi}_q^{(0)} = Q_q^2 \frac{3}{16\pi^2}\left\{\frac{20}{9} + \frac{4z}{3} - \frac{4(z-1)(z+2)}{3z}G(z)\right\}, \quad (1.18)$$
$$\text{where } G(z) = \frac{z}{2\sqrt{1-z}}\log\left\{\frac{\sqrt{1-z}-1}{\sqrt{1-z}+1}\right\}.$$

The pole mass m_q which is the parameter entering the QCD Lagrangian, is not a well defined quantity for the u, d and s light quarks within the framework of perturbation theory. We reexpress the vacuum polarization function as a series in $\bar{m}_q(\mu)$, the *running mass* evaluated at a scale μ, which is well defined. To $\mathcal{O}(\alpha_s)$ the relation between pole and running masses reads

$$\bar{m}_q(\mu^2) = m_q\left\{1 - \frac{\alpha_s(\mu)}{\pi}\left[\frac{4}{3} + \log\frac{\mu^2}{m_q^2}\right] + \mathcal{O}(\alpha_s^2)\right\}.$$

It will prove convenient for the purposes of considering light quarks to convert $\hat{\Pi}_q$ to the *minimal subtraction* ($\overline{\text{MS}}$) scheme $\bar{\Pi}_q$, wherein one subtracts only explicit poles after the renormalization of both mass (m_q) and coupling (α_s) parameters. In this case the vacuum polarization function reads as an expansion

$$\bar{\Pi}_q^{(0)} = Q_q^2\frac{3}{16\pi^2}\left\{\frac{20}{9} - \frac{4}{3}\log\frac{-s}{\mu^2} + 8\frac{\bar{m}_q^2}{s} + \left(\frac{\bar{m}_q^2}{s}\right)^2\left(4 + 8\log\frac{-s}{\bar{m}_q^2}\right) + \mathcal{O}\left(\frac{\bar{m}_q^6}{s^3}\right)\right\},$$

and has a well defined massless limit. At this order the constant subtraction term is given by $\bar{\Pi}_q^{(0)} = \hat{\Pi}_q^{(0)} - \frac{4}{3}Q_q^2\log\frac{\mu^2}{m_q^2}$. We recover the R-ratio by taking the imaginary part[4] of the vacuum polarization function. We are initially interested in the behaviour of R safely above the quark threshold regions, $4\bar{m}_q^2 \ll s$, and so expand in the quantity $z = 4\bar{m}_q^2/s$ to obtain

$$R_q^{(0)}(s) = 12\pi\text{Im}\bar{\Pi}_q^{(0)}(s) = 3Q_q^2\left\{1 - 6\frac{\bar{m}_q^4}{s^2} + \mathcal{O}\left(\frac{\bar{m}_q^6}{s^3}\right)\right\}. \quad (1.19)$$

Eqn. (1.19) immediately makes evident some attractive features of the R-ratio as an observable quantity. We expect R to possess a step structure, with increasing s, as to lowest order and in the *continuum* regions away from non-perturbative resonance effects and where perturbative mass corrections are suppressed, the passage through a flavour threshold increments R by $N_cQ_q^2$. Thus, we are able to count quarks, assess their charges and determine the number of colours in existence. Fig. 1.7 illustrates that the experimental data are entirely consistent with the model

[4]We notice that because the constant term is explicitly real, we can extract the R-ratio equivalently via $R = 12\pi\text{Im}\Pi$ or $R = 12\pi\text{Im}\bar{\Pi}$.

of coloured quarks, namely $N_c = 3$, and the charges of the u, d, s, c and b quarks reading respectively 2/3, -1/3, -1/3, 2/3 and -1/3 as a fraction of e. Deviations from the simple step structure are attributable to higher order QCD corrections.

1.4.2 Two loop vacuum polarization and the R-ratio

At two loops, $\mathcal{O}(\alpha_s)$, we must allow a gluon to traverse the basic quark loop. There are two distinct topologies of Feynman graph which we illustrate in Fig. 1.3. These graphs manifest

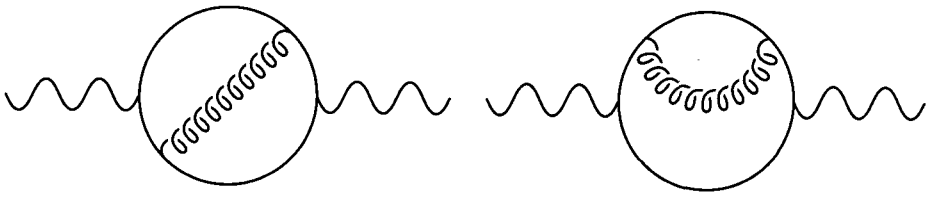

Figure 1.3: Two loop, $\mathcal{O}(\alpha_s)$, contribution to the vacuum polarization function.

Abelian-type behaviour for the gluon propagator, that is we obtain an identical functional form, modulo colour considerations, for the corrections at $\mathcal{O}(\alpha^2)$ to the leptonic contribution of QED - at this order of α_s the gluon is unable to manifest its non-Abelian character. We do need to correct for the colour statistics however, and must sum over all potential colour considerations to obtain the QCD group theoretical colour factor, $C_F = (N_c^2 - 1)/2N_c$, which for the case of QCD gives $C_F = 4/3$. We can recover the $\mathcal{O}(\alpha^2)$ QED contribution, (ie a photon propagating across the quark loop) by resetting $C_F = 1$.

The function $\hat{\Pi}_q^{(1)}(z = 4m_q^2/s)$ has been calculated analytically [16], with the explicit result,

$$\hat{\Pi}_q^{(1)}(z) = \tag{1.20}$$
$$Q_q^2 C_F \frac{3}{16\pi^2}\left\{\frac{5}{6} + \frac{13}{6}z\frac{(z-1)(3z+2)}{z}G(z)\frac{(z-1)(z-16)}{6z}G^2(z) - \frac{(z+2)}{6}\left(1+2(z-1)\frac{d}{dz}\right)zI(z)\right\}.$$

The supplementary function, $I(z)$, is given by

$$I(z) = 6\left(\zeta_3 + 4\mathrm{Li}_3(-u) + 2\mathrm{Li}_3(u)\right) 8\left(2\mathrm{Li}_2(-u) + \mathrm{Li}_2(u)\right)\log u - 2\left(2\log(1+u) + \log(1-u)\right)\log^2 u,$$

in terms of the Riemann-ζ function, $\zeta_n = \sum_{k=1}^{\infty} \frac{1}{k^n}$ and the tri- and di-logarithm functions, whose

series representations read $\mathrm{Li}_n(z) = \sum_{k=1}^{\infty} \frac{z^k}{k^n}$, for $n = 3$ and 2 respectively, and where the functions $u = \frac{\sqrt{1-z}-1}{\sqrt{1-z}+1}$, and $G(z)$ are as previously defined in the one loop case.

Again we can recast the $\hat{\Pi}_q^{(1)}$ function as a power series in $\bar{m}_q^2/s$ using the $\overline{\mathrm{MS}}$ mass in order to regulate the massless limit. The relevant subtraction at this order reads $\bar{\Pi}_q^{(1)} = \hat{\Pi}_q^{(1)} + Q_q^2\left(-\frac{15}{4} + \log\frac{\mu^2}{m_q^2}\right)$ and the resulting expansion is

$$\begin{aligned}\bar{\Pi}_q^{(1)}(s) &= Q_q^2 C_F \frac{3}{16\pi^2}\left\{\frac{55}{12} - 4\zeta_3 - \log\frac{-s}{\mu^2} + \frac{\bar{m}_q^2}{s}\left(16 - 12\log\frac{-s}{\mu^2}\right)\right. \\ &+ \left.\left(\frac{\bar{m}_q^4}{s^2}\right)\left[\frac{2}{3} + 16\zeta_3 + 22\log\frac{-s}{\bar{m}_q^2} - 24\log\frac{-s}{\bar{m}_q^2}\log\frac{-s}{\mu^2} + 12\log^2\frac{-s}{\bar{m}_q^2}\right] + \mathcal{O}\left(\frac{\bar{m}_q^6}{s^3}\right)\right\}.\end{aligned}$$

We recover the $\mathcal{O}(\alpha_s)$ contribution to the R-ratio by picking out the imaginary piece,

$$R_q^{(1)}(s) = 12\mathrm{Im}\bar{\Pi}_q^{(1)}(s) = 3Q_q^2 C_F\left\{\frac{3}{4} + 9\frac{\bar{m}_q^2}{s} + \frac{\bar{m}_q^4}{s^2}\left(-\frac{33}{2} + 18\log\frac{s}{\mu^2}\right) + \mathcal{O}\left(\frac{\bar{m}_q^6}{s^3}\right)\right\}. \tag{1.21}$$

We note that we could have equivalently obtained this final expression by making a direct calculation of the cross-section of $e^+e^- \to q\bar{q}g$, taking care to ensure the cancellation between divergences, and normalized to the pointlike $e^+e^- \to \mu^+\mu^-$ cross-section.

1.4.3 Three loop vacuum polarization and the R-ratio

At $\mathcal{O}(\alpha_s^2)$ we open up a further rich variety of Feynman graph topologies. These can be broadly categorized into two sets, graphs that are again pseudo-Abelian in nature, and those that are intrinsically non-Abelian and will explicitly illustrate that facet of QCD, both classes of diagram will admit non-trivial physics.

At this order, the gluon self-interaction manifests itself in diagrams containing a triple gluon vertex - either as a single triple gluon interaction within the quark loop, or as an internal gluon loop insertion in the $\mathcal{O}(\alpha_s)$ primary quark loops gluon propagator. We require a supplementary group theoretical colour factor at this order, $C_A = N_c$ to account for the colour counting of the non-Abelian Feynman diagrams. Representative graphs are shown in Fig. 1.4, and contribute $C_A C_F \hat{\Pi}_{NA}^{(2)}$ to the $\mathcal{O}(\alpha_s^2)$ vacuum polarization function, $\hat{\Pi}_q^{(2)}$, where $\hat{\Pi}_{NA}^{(2)}$ is written (for brevity maintaining only terms to $\mathcal{O}(m_q^2/s)$) [17, 18],

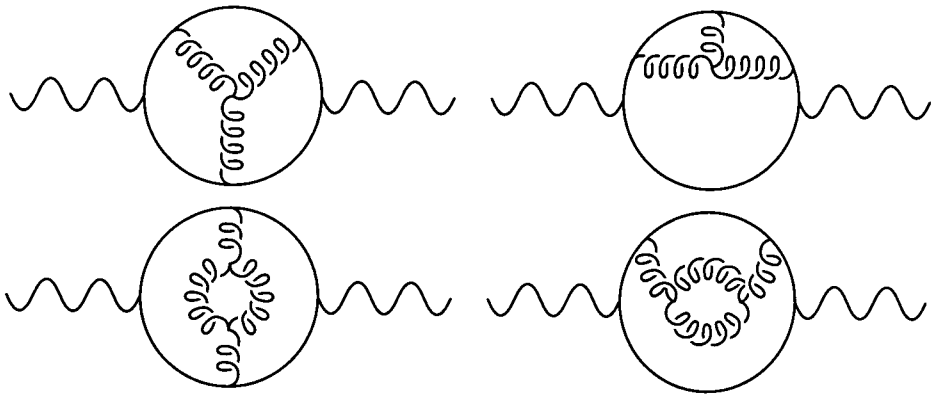

Figure 1.4: Three loop, $\mathcal{O}(\alpha_s^2)$, contributions to the vacuum polarization function arising from graphs containing the non-Abelian triple gluon vertex. Ghost particles, necessary to cancel unphysical polarizations of the gluon loop, are implicit contributions.

$$\begin{aligned}\hat{\Pi}^{(2)}_{NA}(s) &= Q_q^2 \frac{3}{16\pi^2}\left[\frac{4873}{432} + \frac{4}{3}\zeta_2 - 4\zeta_2 \log 2 - \frac{4013}{288}\zeta_3 - \frac{5}{3}\zeta_5 - \frac{157}{36}\log\frac{-s}{m_q^2} + \frac{11}{12}\log\frac{-s}{\mu^2}\log\frac{-s}{m_q^2}\right. \\ &- \frac{11}{24}\log^2\frac{-s}{m_q^2} - \frac{55}{72}\log\frac{-s}{\mu^2} + \frac{11}{3}\zeta_3\log\frac{-s}{\mu^2} + \frac{4m_q^2}{s}\left\{\frac{7}{2} + 2\zeta_2 - 6\zeta_2\log 2 + \frac{17}{6}\zeta_3\right. \\ &\left.\left. - \frac{85}{12}\zeta_5 - \frac{185}{24}\log\frac{-s}{m_q^2} + \frac{11}{4}\log\frac{-s}{\mu^2}\log\frac{-s}{m_q^2} - \frac{11}{8}\log^2\frac{-s}{m}\right\} + \mathcal{O}\left(\frac{m_q^4}{s^2}\right)\right].\end{aligned}$$

In addition to these novel contributions, we initiate a pseudo-Abelian set of graphs containing secondary quark loop insertions into the gluon propagating through the primary loop. These so-called *double bubble* diagrams, depicted in Fig. 1.5, can be further classified by the nature of the quarks in the master and slave fermion loops.

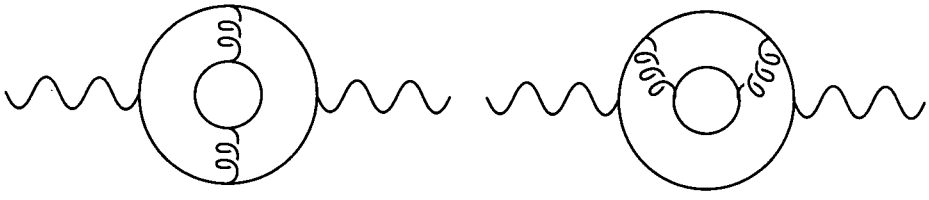

Figure 1.5: Three loop, $\mathcal{O}(\alpha_s^2)$, contributions to the vacuum polarization function arising from 'double bubble' graphs which contain an internal quark loop.

The physics of a heavy quark coupling to internal light quarks is described by a contribution

$C_F T n_l \Pi_l^{(2)}$ (where we need the group trace normalization, $T = 1/2$) and is proportional to the number of active light quark flavours, n_l, able to propagate within the loop. The case where the two loops possess the same (heavy) mass parameter is given by the contribution $C_F T \Pi_F^{(2)}$ [17, 18],

$$\begin{aligned}
\hat{\Pi}_l^{(2)} &= Q_q^2 \frac{3}{16\pi^2}\left[-\frac{116}{27}+\frac{4}{3}\zeta_2+\frac{38}{9}\zeta_3+\frac{14}{9}\log\frac{-s}{m_q^2}-\frac{1}{3}\log\frac{-s}{\mu^2}\log\frac{-s}{m_q^2}+\frac{1}{6}\log^2\frac{-s}{m_q^2}+\frac{5}{18}\log\frac{-s}{\mu^2}\right. \\
&\quad \left. -\frac{4}{3}\zeta_3\log\frac{-s}{\mu^2}+\frac{4m_q^2}{s}\left\{-1+2\zeta_2+\frac{13}{6}\log\frac{-s}{m_q^2}-\log\frac{-s}{\mu^2}\log\frac{-s}{m_q^2}+\frac{1}{2}\log^2\frac{-s}{m_q^2}\right\}+\mathcal{O}\left(\frac{m_q^4}{s^2}\right)\right] \\
\hat{\Pi}_F^{(2)} &= Q_q^2 \frac{3}{16\pi^2}\left[-\frac{307}{217}+\frac{8}{3}\zeta_2+\frac{545}{144}\zeta_3+\frac{14}{9}\log\frac{-s}{m_q^2}-\frac{1}{3}\log\frac{-s}{\mu^2}\log\frac{-s}{m_q^2}+\frac{1}{6}\log^2\frac{-s}{m_q^2}+\frac{5}{18}\log\frac{-s}{\mu^2}\right. \\
&\quad \left. -\frac{4}{3}\zeta_3\log\frac{-s}{\mu^2}+\frac{4m_q^2}{s}\left\{-\frac{10}{3}-4\zeta_2+4\zeta_3+\frac{13}{6}\log\frac{-s}{m_q^2}-\log\frac{-s}{\mu^2}\log\frac{-s}{m_q^2}+\frac{1}{2}\log^2\frac{-s}{m_q^2}\right\}+\mathcal{O}\left(\frac{m_q^4}{s^2}\right)\right].
\end{aligned}$$

$C_F^2 \Pi_A^{(2)}$ represents the remaining contribution common to Abelian theories, those Feynman graphs containing gluons with neither self-interaction vertices nor internal loops, and there are a further eight representative topologies yielding [17, 18],

$$\begin{aligned}
\hat{\Pi}_A^{(2)} &= Q_q^2 \frac{3}{16\pi^2}\left[-\frac{121}{48}-5\zeta_2+8\zeta_2\log 2-\frac{99}{16}\zeta_3+10\zeta_5+\frac{1}{8}\log\frac{-s}{m_q^2}\right. \\
&\quad \left. +\frac{4m_q^2}{s}\left\{\frac{139}{12}-\frac{15}{2}\zeta_2+12\zeta_2\log 2-\frac{41}{12}\zeta_3-\frac{35}{6}\zeta_5-\frac{3}{8}\log\frac{-s}{m_q^2}+\frac{9}{4}\log^2\frac{-s}{m_q^2}\right)+\mathcal{O}\left(\frac{m_q^4}{s^2}\right\}\right].
\end{aligned}$$

Again we can make the relevant conversion to the $\overline{\text{MS}}$ scheme and take the absorptive part to obtain the corresponding R-ratio contributions, which read

$$\begin{aligned}
R_A^{(2)} &= 3Q_q^2\left\{-\frac{3}{32}+\frac{\bar{m}_q^2}{s}\left\{\frac{153}{8}-\frac{27}{4}\log\frac{s}{\mu^2}\right\}+\mathcal{O}\left(\frac{\bar{m}_q^4}{s^2}\right)\right\}, \\
R_{NA}^{(2)} &= 3Q_q^2\left\{-\frac{123}{32}-\frac{11}{12}\log\frac{s}{\mu^2}-11\zeta_3+\frac{\bar{m}_q^2}{s}\left\{\frac{185}{8}-\frac{33}{4}\log\frac{s}{\mu^2}\right\}+\mathcal{O}\left(\frac{\bar{m}_q^4}{s^2}\right)\right\}, \\
R_l^{(2)} &= 3Q_q^2\left\{-\frac{11}{8}-\frac{1}{4}\log\frac{s}{\mu^2}+\zeta_3+\frac{\bar{m}_q^2}{s}\left\{-\frac{13}{2}-3\log\frac{s}{\mu^2}\right\}+\mathcal{O}\left(\frac{\bar{m}_q^4}{s^2}\right)\right\} \quad \text{and} \\
R_F^{(2)} &= 3Q_q^2\left\{-\frac{11}{8}-\frac{1}{4}\log\frac{s}{\mu^2}+\zeta_3+\frac{\bar{m}_q^2}{s}\left\{-\frac{13}{2}-3\log\frac{s}{\mu^2}\right\}+\mathcal{O}\left(\frac{\bar{m}_q^4}{s^2}\right)\right\}.
\end{aligned}$$

Note that $R_l^{(2)}$ and $R_F^{(2)}$ are identical at $\mathcal{O}(\bar{m}_q^2/s)$.

We have thus far neglected the possibility of the radiation of massive quarks, c, b, from the light u, d, s. Unfortunately the full contribution to the vacuum polarization at three loops is not known, however the contribution to the absorptive part (equivalently the R-ratio) was

calculated in [21]. This represents corrections to the hadronic cross-section for production of a light quark made by virtual heavy loops, the contribution is proportional to $C_F T$ and reads

$$R_Q^{(2)} = 3Q_Q^2 \frac{s}{\bar{m}_Q^2}\left\{\frac{22}{225} + \frac{1}{45}\log\frac{\bar{m}_Q^2}{s}\right\},$$

where $\bar{m}_Q$ is the running mass of the heavy quark.

The complete $\mathcal{O}(\alpha_s^2)$ R-ratio is constructed by summing the individual increments made by active quark flavours at a particular energy, and virtual heavy quarks contribute beneath and close to their threshold through additions R_Q.

Energy domain	active flavours(q)	virtual participants (Q)
$2m_\pi\sqrt{s} < 3.74$ GeV	u, d, s	c, b
$5 < \sqrt{s} < 10.56$ GeV	u, d, s, c	b

The total set of contributions at $\mathcal{O}(\alpha_s^2)$ to R is then written as the sums

$$R^{(2)} = \sum_q Q_q^2\left\{C_F^2 R_A^{(2)} + C_A C_F R_{NA}^{(2)} + C_F T n_l R_l^{(2)} + C_F T R_F^{(2)}\right\} + \sum_Q Q_Q^2 C_F T R_Q^{(2)}.$$

1.4.4 Four loop vacuum polarization and the R-ratio

The massless vacuum polarization function has not been determined in its entirety, but for our purposes it is enough to know the absorptive part, which was calculated in [19], and generates a flavour dependent supplement to R which reads numerically, [20],

$$\begin{aligned} R_q^{(3)}(s) &= Q_q^2\left\{-6.6369 - 1.2001 n_f - 0.0052 n_f^2 + \left(-17.2964 + 2.0877 n_f - 0.0384 n_f^2\right)\log\frac{s}{\mu^2}\right. \\ &+ \left.\left(7.5625 - 0.9167 n_f + 0.0278 n_f^2\right)\log^2\frac{s}{\mu^2}\right\}. \end{aligned} \tag{1.22}$$

Also at $\mathcal{O}(\alpha_s^3)$ we open up the *singlet* contribution[5], originating in a graph with three gluonic propagators connecting potentially distinct flavour quark loops, Fig. 1.6, whose absorptive part, relevant to $R^{(3)}$ has been calculated as, [20],

$$R_S^{(3)} = -1.2395\left(\sum_q Q_q\right)^2$$

[5] An analogous non-singlet diagram at $\mathcal{O}(\alpha_s^2)$ with two gluon intermediaries does not contribute, as demanded by *Furry's theorem*, which insists that the Green function contribution associated with a fermion loop possessing an odd number of vertices vanishes identically.

Unlike the previous terms, the singlet contribution is proportional to the sum of the charges squared, $(\sum_q Q_q)^2$. The contributions of the three light u, d and s quarks cancel as $\sum_{u,d,s} Q_q =$

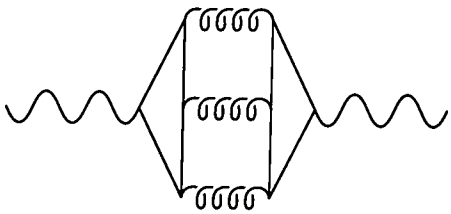

Figure 1.6: The singlet contribution to vacuum polarization function at $\mathcal{O}(\alpha_s^3)$.

0, and this flavour cancellation is compounded by the fact that the singlet contribution is numerically rather small, its net effect is not significant.

1.4.5 Gathering R together

The R-ratio has been calculated to $\mathcal{O}(\alpha_s^3)$, an enviable level of theoretical precision, and one certainly not yet matched by the endevours of experimentalists. As an input into the dispersion relation, (1.15), we should specify a set of parameters used to enumerate the expressions of the previous section. We select $\mu^2 = s$, a choice which represents the typical interaction energy and nullifies the logarithms in $\log s/\mu^2$. Additionally we quantify the sensitivity to choice of scale by varying μ^2 within the bounds $s/2 \leq \mu^2 \leq 2s$. We use $\Lambda^{(5)}_{\overline{\text{MS}}} = 220$ MeV, which corresponds to the world average $\alpha_s\left(M_Z^2\right) = 0.119$.

For numerical calculations, full mass expansions to $\mathcal{O}(\bar{m}^4/s^2)$ are used [20] with a running coupling and quark masses. The prescription for matching these masses and couplings across the flavour thresholds is carried out, again in accordance with [20]. The light u, d and s quarks are taken to be massless, and pole masses of the heavy c, b and t quarks are taken to be $M_c = 1.46$ GeV, $M_b = 4.7$ GeV and $M_t = 174$ GeV. This prescription yields a total R-ratio expansion which we illustrate with continuum data in Fig. 1.7, we obtain a clearer description of continuum regions using perturbative methods than the data.

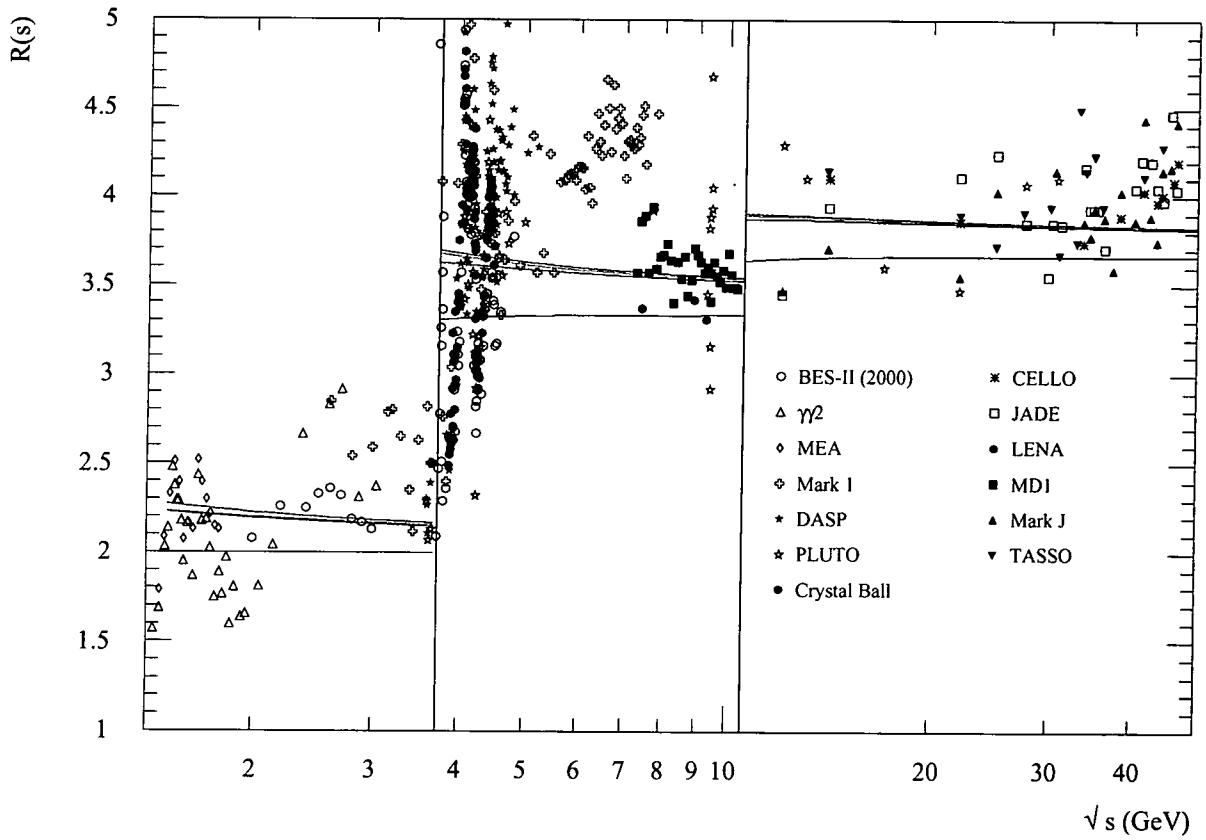

Figure 1.7: The R-ratio of Section 1.4, order by order up to the massless $\mathcal{O}(\alpha_s^3)$ contribution. The tree level contribution is the curve in black, to $\mathcal{O}(\alpha_s)$ in blue, $\mathcal{O}(\alpha_s^2)$ in magenta and $\mathcal{O}(\alpha_s^3)$ in red. The distinction between the $\mathcal{O}(\alpha_s^2)$ and $\mathcal{O}(\alpha_s^3)$ is rather small, even at low energies. The physical flavour thresholds are taken to be demarcated by the threshold for $D^{\pm}$ charm meson, and $B^{\pm}$ bottom meson production. A broad compilation of inclusive measurements have been superimposed, with their errors suppressed for clarity [22, 23, 24, 25, 26, 27]. Note that it is widely agreed that the normalizations of the MARK 1 [24], DASP [25]and PLUTO [26] data through the charm threshold ($\sqrt{s} \simeq 4m_c^2$) are suspect. In Section 1.5.3 we see how they can be fixed by the perturbative prediction in the continua straddling threshold. Note that perturbative QCD fails to describe the data adequately towards low energies and through the charm threshold itself.

1.5 Empirical input in non-perturbative regions

We have seen that at low energies, $\sqrt{s} \lesssim 2$ GeV, and through the $q\bar{q}$ resonance regions pertubative methods of the determining the total hadronic cross-section become inapplicable and we must substitute the available e^+e^-annihilation data in lieu of analytical methods. This entails a raft of practical issues on the most objective way to combine the information assimilated from a wide variety of sources. In the low energy region $\sqrt{s} \lesssim 1.5$ GeV inclusive measurements of the total hadronic cross-section are not available, and we have to exhaustively sum the individual annihilation channels to construct the total hadronic cross-section. In this section we shall collate the available data, demonstrate the prescription by which it can be most effectively combined and investigate the inherent uncertainties that arise.

1.5.1 Data processing

A diverse range of collaborations throughout the experimental high energy physics community have made piecewise contributions to the library of e^+e^- annihilation data. The measurements are typically made over different intervals of $\sqrt{s}$, and the data are of a broad spectrum of quality. Extracting the maximal amount of objective information from this glut of data is a non-trivial task. We can take into account correlations between data points, arising from the common systematical errors inherent in a data set by using a correlated χ^2 minimization procedure [28].

For $N_{\rm exp}$ distinct but overlapping data sets, where x_i^n is the ith cross-section measurement for the nth data set, with corresponding statistical and systematic errors $\Delta^n_{i,\rm stat}$ and $\Delta^n_{i,\rm sys}$ respectively, the χ^2 function is defined as

$$\chi^2 = \sum_{n=1}^{N_{\rm exp}} \sum_{i,j=1}^{N_n} \left(x_i^n - k_i\right) \left(C_{ij}^n\right)^{-1} \left(x_j^n - k_j\right), \tag{1.23}$$

where the $\{k_i\}$ correspond to the unknown distribution to be interpolated. The covariance matrices, C^n, are defined in the following manner,

$$C_{ij}^n = \begin{cases} \left(\Delta^n_{i,\rm stat}\right)^2 + \left(\Delta^n_{i,\rm sys}\right)^2 \text{ for } i = j \\ \Delta^n_{i,\rm stat} \cdot \Delta^n_{i,\rm sys} \text{ for } i \neq j \end{cases} \quad i,j = 1,...,N_n.$$

We finally insist on the usual minimization condition, $\frac{\partial \chi^2}{\partial k_i} = 0$ for each i which lead to a set of linear equations which can be solved numerically,

$$\sum_{n=1}^{N_{\rm exp}} \sum_{j=1}^{N_n} \left(x_j^n - k_j\right) \left(C_{ij}^n\right)^{-1} = 0, \quad i = 1, ..., N_n. \tag{1.24}$$

This procedure also defines a combined covariance matrix, $\tilde{C}_{ij}$, from which we are able to extract the covariances between individual members of the interpolated distribution k_i and k_j. Its inverse is determined by the sum over each of the individual inverse covariance matrices in the following manner

$$\tilde{C}_{ij}^{-1} = \sum_{n=1}^{N_{\rm exp}} \left(C_{ij}^n\right)^{-1}.$$

In this manner we treat the error propagation in a consistent way, and obtain a distribution of data points $\{k_i\}$ which objectively reflect the amalgamation of measurements from a variety of independent sources.

1.5.2 Low energy region, $2m_\pi < \sqrt{s} < 2.8$ GeV

The low energy interval, $2m_\pi < \sqrt{s} \lesssim 2.8$ GeV is the most poorly defined part of the integration area, and unfortunately is the region that the hadronic contribution shows most sensitivity to. The integral of Eqn. (1.15) is weighted such that a significant portion of the hadronic contribution, and a correspondingly significant piece of the overall error, will originate from this energy interval.

For the region from the threshold of pion production to the ω-resonance, $2m_\pi - 0.81$ GeV, we use $e^+e^- \to \pi^+\pi^-$ data to reconstruct the broad peak corresponding to the ρ-resonance. This data is traditionally given in terms of the pion form factor, which is simply related to the cross-section, $\sigma_{\pi\pi}$, through the relation,

$$\sigma_{\pi\pi}(s) = \frac{\pi}{3} \frac{\alpha^2 \beta_\pi^3}{s} \left|F_\pi(s)\right|^2, \quad \text{where } \beta_\pi = (1 - 4m_\pi^2/s)^{1/2}.$$

Many experiments, [29, 30], have made measurements of the ρ-region, and the resonance shape is well determined. Recent experiments by the CMD-2 collaboration [30] at the VEPP-2M facility in Novosibirsk have resolved the ρ very well, to such and extent that we are able to see clearly

structure due to $\rho - \omega$ interference. The data amalgamation prescription of (1.24) is adhered to. We illustrate the resulting error band and spread of the source data in Fig. 1.8.

At energies very close to threshold, the relative sparseness of the data represents a problem. It is possible to implement an expansion from *chiral perturbation theory* [31] which describes the cross-section near these low energies,

$$F_\pi^{\mathrm{ChPT}}(s) = 1 + \frac{1}{6}\langle r^2\rangle_\pi + c_\pi s^2 + \mathcal{O}(s^3). \tag{1.25}$$

The coefficients were obtained in [32, 33] respectively, the pion charge radius squared, $\langle r^2\rangle_\pi = (0.431 \pm 0.026)$ fm^2 and $c_\pi = (3.2 \pm 1.0)$ GeV^{-4}.

This interval also contains the narrow ω-resonance in the 3π channel which we explicitly superimpose in the form of a relativistic Breit-Wigner resonance separately. We discuss its precise parameterization later in Section 1.5.5.

As the centre of mass energy increases, the collider energies become able to stimulate a larger variety of e^+e^- annihilation channels [34, 35, 36, 37, 38]. There exists an energy window where we have no full inclusive measurement of the total hadronic cross-section, and must reconstruct the total cross-section as the sum of an exhaustive census of individual annihilation channel contributions to $e^+e^- \to$ hadrons. The term *exclusive* cross-section has been coined. We treat each channel independently by the prescription of (1.24), and then sum linearly each of these amalgamated data sets in order to make most use of the available information. The results are detailed in Table 1.1.

We should be aware that the decomposition of annihilation modes of Table 1.1 contains channels, denoted with the superscripts $^{(1)}$ and $^{(2)}$, that exhibit subsequent decays into the many pion final states listed separately. We must avoid the double counting of contributions implicitly included in these multiple pion modes, and achieve this by subtracting the portions of cross-section already accounted for.

The ω annihilation channels (marked by $^{(1)}$ in Table 1.1) decays dominantly into three pions, which means the $e^+e^- \to \omega\pi^0$ and $e^+e^- \to \omega\pi^+\pi^-\pi^0$ channels are mostly contained within the four and six pion final states. The appropriate branching ratios, $Br(\omega \to \pi^+\pi^-\pi^0) = 88.8 \pm 0.7\%$ and $Br(\omega \to \pi^+\pi^-) = 2.2 \pm 0.3\%$, [6], specify how much of this contribution is unaccounted

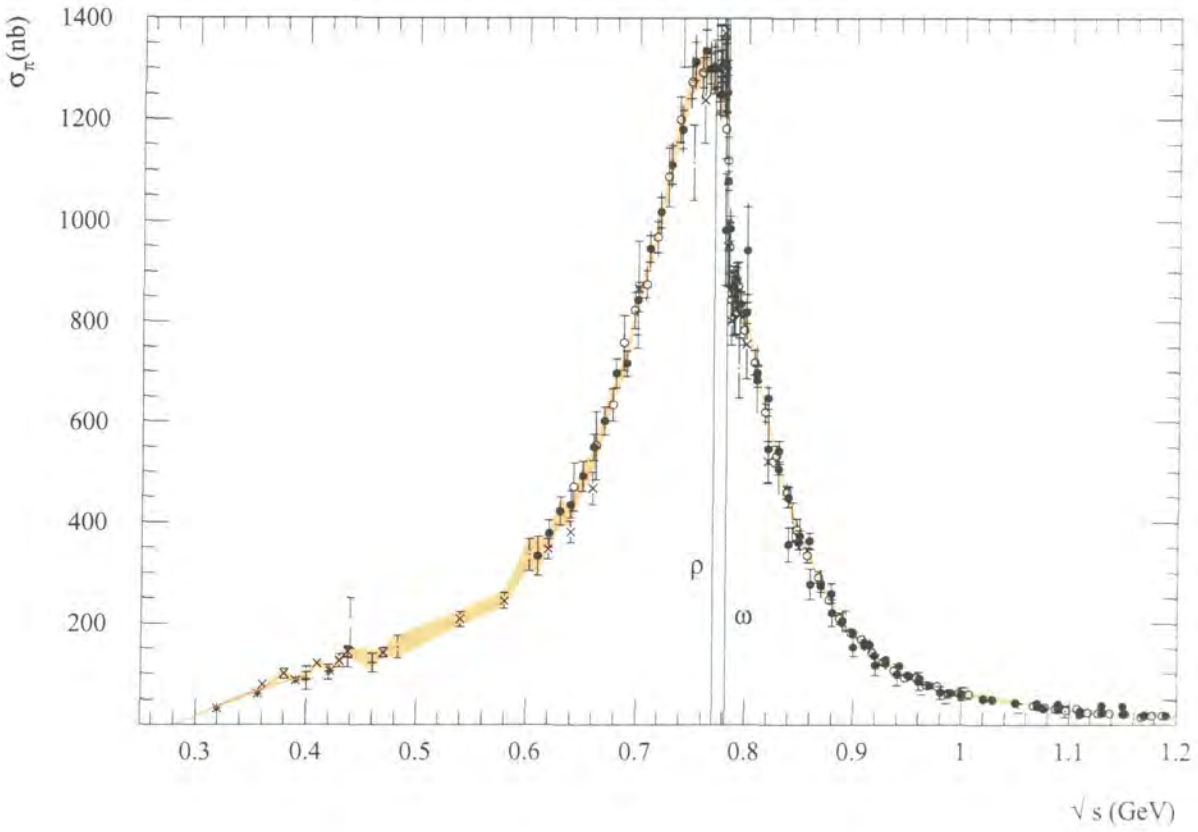

Figure 1.8: The cross-section for pion pair production, $\sigma_{\pi\pi}(s)$, versus $\sqrt{s}$ around the ρ-resonance region, $2m_\pi < \sqrt{s} \lesssim 1$ GeV. We show a comprehensive collection of data [29], including rather recent and accurate results from Novosibirsk, [30], which have helped considerably to better resolve the cross-section in this interval. The orange band illustrates the spread of uncertainty about a central value interpolated from the data compilation, in accordance with the prescription of Eqn. (1.24). The red line at low energies shows the chiral expansion of the two pion cross-section of Eqn. (1.25). The vertical lines demarcate the central peaks of the ρ and ω resonances, in fact the data amalgamation is able to resolve interference between the two.

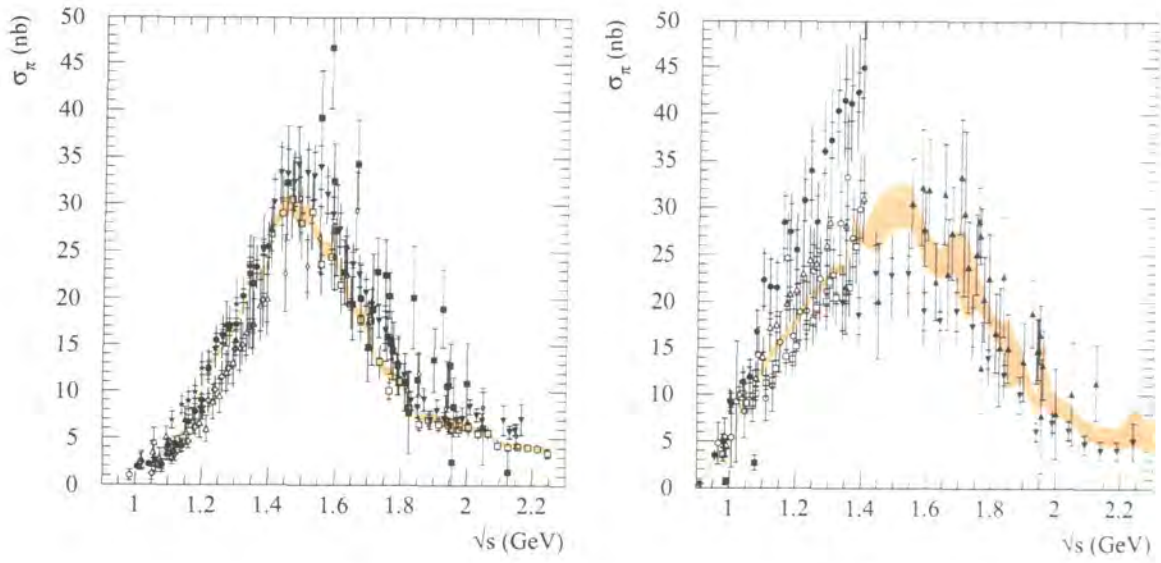

$e^+e^- \to \pi^+\pi^-\pi^+\pi^-$ $e^+e^- \to \pi^+\pi^-\pi^0\pi^0$

Figure 1.9: The cross-section (in nb) of the four pion channels in e^+e^- annihilation, which comprise the chief contribution to the total cross-section after $e^+e^- \to \pi^+\pi^-$. The data are compiled from a variety of experimental collaborations, [38]. The orange band again shows the interpolation from the data of Eqn. (1.24), it is clear that the cross-section of $e^+e^- \to \pi^+\pi^-\pi^+\pi^-$ is rather better determined than the cross-section of $e^+e^- \to \pi^+\pi^-\pi^0\pi^0$.

for in residual channels that we ought to include, and $\sigma_{\omega\pi^0}$ and $\sigma_{\omega\pi^+\pi^-\pi^0}$ are corrected by a factor (1-0.91=0.09). Similarly the η annihilation channel (marked by $^{(2)}$ in Table 1.1) exhibits subsequent three pion decay modes, and we should exclude from the total $e^+e^- \to \eta\pi^+\pi^-$ cross-section these subsequent decays which are implicitly include in the five pion channels. The branching ratios $Br(\eta \to \pi^0\pi^0\pi^0) = 23.2 \pm 0.4\%$ and $Br(\eta \to \pi^+\pi^-\pi^0) = 32.1 \pm 0.4\%$, [6], determine the proportion of uncounted residual contributions from other decays of the η, and so $\sigma_{\eta\pi^+\pi^-}$ is corrected by a factor (1-0.553 = 0.447).

There exist some *unmeasured* channels, denoted by $^{(3)}$ in Table 1.1, which should be included for the sum to properly reflect the total cross-section $e^+e^- \to$ hadrons. These have been reconstructed via isospin relations which relate the unmeasured modes to linear combinations of the measured annihilation channels.

The five pion final state cross-sections are rather simply related in the following manner, [28].

$\sigma_{\pi^+\pi^-3\pi^0} = \frac{1}{2}\sigma_{2\pi^+2\pi^-\pi^0}$. An upper bound on the undetermined six pion channel was derived in [39], following [28] an estimate of its cross-section is obtained by taking half of this upper bound conservatively saturated with a 100% error, $\sigma_{\pi^+\pi^-4\pi^0} \leq \frac{3}{2}\sigma_{2\pi^+2\pi^-2\pi^0} - \frac{9}{24}\sigma_{3\pi^+3\pi^-}$. One further isospin relation is used to equate the unknown $e^+e^- \to K^+K^-\pi^0$ cross-section to that of the $e^+e^- \to K^0_S K^0_L \pi^0$, [28], $\sigma_{K^0_S K^0_L \pi^0} = \sigma_{K^+K^-\pi^0}$. In this way we exhaust the possible set of available hadronic final states for e^+e^- annihilation in the energy interval.

We use the 'partially' inclusive DM2 measurements of the $e^+e^- \to K^0_S + X$ reaction to estimate the contribution to the total hadronic cross-section made by the $K\bar{K}\pi\pi$ channel, denoted with a $^{(4)}$ in Table 1.1, following [28]. The following modes are already explicitly included, $K^0_S K^0_L$, $K^0_S K^+\pi^-$ and $K^0_S K^0_L \pi^0$, assuming that $K^0\bar{K}^0(\pi\pi)^0$ and $K^+K^-(\pi\pi)^0$ make equal contributions, the total $K\bar{K}\pi\pi$ cross-section is twice the $K^0_S + X$ cross-section corrected for the measured channels.

The individual components summing to the exclusive cross-section in the regions $2m_\pi - 1.46$ GeV and $1.46 - 1.9$ GeV are given in Table 1.1. We check the contributions to the cross-section from each annhihilation channel with the detailed decomposition given in [28], and find excellent consistency between the two evaluations. The dominant portions of the hadronic cross-section arise from the two and four pion final states.

As we scan beyond $\sqrt{s} \gtrsim m_\tau \simeq 1.8$ GeV, simultaneously the compilation of exclusive channels becomes unreliable and measurements that do not discriminate between hadronic final states become available. The latter in the form of older data [23, 24, 25, 26, 27], and more recent precise measurements from the BES-II collaboration at Beijing [22]. We can construct an interpolated total hadronic cross-section purely from these non-exclusive measurements using Eqn. (1.24), and term it the *inclusive* cross-section, which is then used as the parameterization input to the dispersion integral (1.15).

The early measurements of this region seemed to indicate the existence of a broad structure throughout $2 \lesssim \sqrt{s} \lesssim 3$ GeV, and they produced a curve that exceeded the perturbative prediction by as much as 20%. It was thought that this might be evidence for some gluonic bound state, although subsequent release of inclusive measurements [22] of the R-ratio from BES-II showed consistency with QCD to within a standard deviation - these new data have pinched the

Final state	$\Delta\alpha^{(5)}_{\rm had}(M_Z^2)\cdot 10^4$ $2m_\pi - 1.46$ GeV	$\Delta\alpha^{(5)}_{\rm had}(M_Z^2)\cdot 10^4$ $1.46 - 1.9$ GeV
$\pi^+\pi^-$	33.93 ± 0.52	0.17 ± 0.06
$\pi^+\pi^-\pi^0$	0.30 ± 0.04	0.17 ± 0.05
$\pi^+\pi^-\pi^0\pi^0$	2.00 ± 0.08	2.99 ± 0.31
$\omega\ \pi^0$ (1)	0.12 ± 0.02	0.04 ± 0.01
$\pi^+\pi^-\pi^+\pi^-$	1.45 ± 0.05	2.29 ± 0.09
$\pi^+\pi^-\pi^+\pi^-\pi^0$	0.09 ± 0.04	0.70 ± 0.25
$\pi^+\pi^-\pi^0\pi^0\pi^0$ (3)	0.04 ± 0.05	0.33 ± 0.22
$\omega\ \pi^+\pi^-$ (1)		0.02 ± 0.00
$\pi^+\pi^-\pi^+\pi^-\pi^+\pi^-$		0.05 ± 0.02
$\pi^+\pi^-\pi^+\pi^-\pi^0\pi^0$	0.02 ± 0.01	0.82 ± 0.09
$\pi^+\pi^-\pi^0\pi^0\pi^0\pi^0$ (3)	0.01 ± 0.01	0.61 ± 0.61
$\eta\ \pi^+\pi^-$ (2)	0.02 ± 0.02	0.12 ± 0.04
K^+K^-	0.53 ± 0.05	0.16 ± 0.02
$K^0_SK^0_L$	0.15 ± 0.11	0.04 ± 0.02
$K^0_SK^+\pi^-(K^0_LK^-\pi^+)$ (3)	0.03 ± 0.01	0.28 ± 0.05
$K^+K^-\pi^0$		0.10 ± 0.07
$K^0_SK^0_L\pi^0$ (3)		0.10 ± 0.07
$K\bar{K}\pi\pi$ (4)	0.01 ± 0.25	1.04 ± 0.67
Sum of contributions	38.76 ± 0.79	10.32 ± 1.06

Table 1.1: A detailed breakdown of the individual exclusive channel contributions to $\Delta\alpha^{(5)}_{\rm had}(M_Z^2)$. The dominant contribution arises from the $e^+e^- \to \pi^+\pi^-$, and the next most significant contributions are obtained from $e^+e^- \to \pi^+\pi^-\pi^+\pi^-$ and $e^+e^- \to \pi^+\pi^-\pi^0\pi^0$, depicted in Fig. 1.9. The channels marked with (1) have to be corrected for missing modes. The channel highlighted by (2) has had $\eta \to 3\pi$ contributions subtracted. Those modes marked by (3) have their contributions deduced from isospin relations, as described in the main body of the text. The modes described in (4) are deduced from the 'partially' inclusive measurements of $e^+e^- \to K^0_S + X$ with modes explicitly included elsewhere subtracted.

interpolation firmly back in place with the theoretical expectations.

The amalgamated inclusive and exclusive cross-sections are nominally complementary measurements, and we check their mutual consistency by a comparison in their region of overlap $1.5 \lesssim \sqrt{s} \lesssim 1.9$ GeV[6]. Each of the descriptions of the R-ratio is illustrated in Fig. 1.10, and it is readily apparent that there exists an incompatibility in normalization between the two, with the central interpolation of the inclusive data typically lying some 10% beneath that of the exclusive, although the shape manifests the same features. We might ascribe this inconsistency to either a systematic overcounting of annihilation channels or a normalization error within the inclusive data, but the resolution is not immediately clear. We shall investigate this further later, and for now resolve to perform parallel calculations using first inclusive and then exclusive data in the overlapping region, and defer the subjective choice between the two.

For the overlapping energy interval, corresponding to the onset of the inclusive data to the limit of the exclusive summation, we obtain contributions to $\Delta\alpha^{(5)}_{\text{had}}(M_Z^2) \cdot 10^4$ of 8.62 ± 0.60 and 10.32 ± 1.06 respectively for the inclusive and exclusive data as the R input to (1.15).

At $\sqrt{s} = 1.9$ GeV, we use the inclusive data until the point where we consider that perturbative calculations offer the best description of the R-ratio. This onset is taken at $\sqrt{s} = 2.8$ GeV, where the BES-II data point matches precisely the theoretical expectation. The contribution from the inclusive data in this interval is 13.26 ± 0.83. However, the exclusive data below $\sqrt{s} = 1.9$ GeV lie some way above the inclusive, and in order to circumvent the unappealing prospect of a discontinuous R-ratio at this point, we insert the perturbative evaluation up to $\sqrt{s} = 2.2$ GeV where it matches smoothly to the inclusive data. This procedure gives a parallel low energy contribution to $\Delta\alpha^{(5)}_{\text{had}}(M_Z^2) \cdot 10^4$ of 13.79 ± 0.83, where we allocate a generous error estimate from the inclusive data.

The QCD prediction for the remainder of the low energy interval until we reach the physical charm threshold at $\sqrt{s} = 2m_{D^\pm} = 3.74$ GeV, is given by the light u, d and s contributions, with small corrections due to heavy virtual c quark loops and is obtained from Eqn. 1.17. This contributes a further 9.73 ± 0.05.

[6]In fact the overlapping region extends up to $\sqrt{s} \lesssim 2.1$ GeV, but here the accuracy of individual channel measurements degrades to such an extent that the summation is not assured of reflecting the true cross-section.

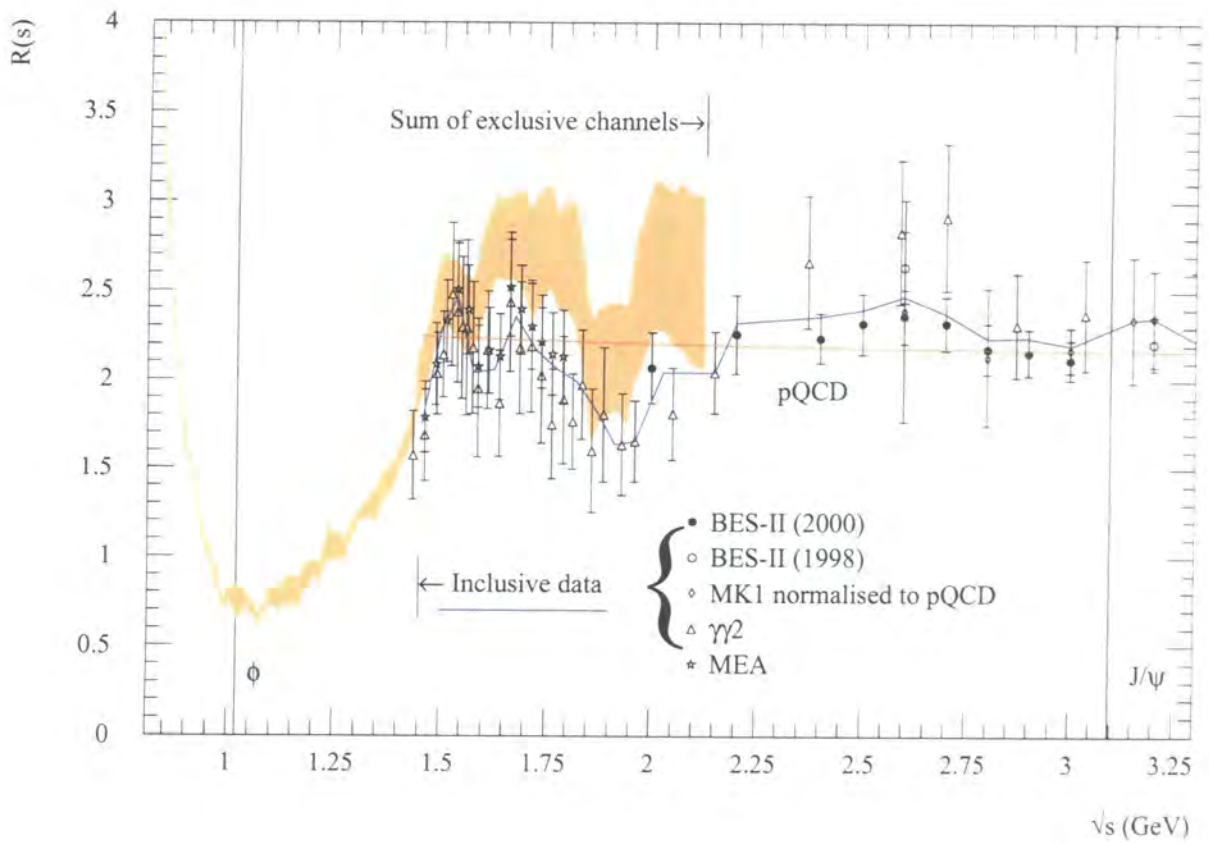

Figure 1.10: The quantity $R(s)$ versus $\sqrt{s}$ in the critical low energy interval, $\sqrt{s} \lesssim 3$ GeV. The orange band below $\sqrt{s} = 2.125$ GeV now illustrates the bounds of the summed exclusive channels, which have each individually been compiled using Eqn. (1.24). The inclusive data are explicitly plotted, and above $\sqrt{s} = 1.46$ GeV the blue curve shows the central value of their interpolation. In the overlapping interval there is a distinct discrepancy between the two (in principle) complementary measurements. The central perturbative QCD prediction at $\mathcal{O}(\alpha_s^3)$ is plotted in red through the inclusive region for comparison. There are hints of non-trivial structure below $\sqrt{s} \lesssim 2.5$ GeV. Finally, the vertical lines denoting the central positions of the ϕ and J/ψ resonances are depicted.

A further set of contributions from this interval is obtained by superimposing the narrow resonance of the ϕ, and the lower narrow ψ's using a relativistic Breit-Wigner parameterization (1.26), and these are written out in Section 1.5.5.

1.5.3 Charm threshold, $3.74 < \sqrt{s} < 5.0$ GeV

Severe fluctations of the cross-section are apparent in the data through the charm threshold interval, $3.74 \lesssim \sqrt{s} \lesssim 5$ GeV, illustrated in Fig. 1.11. This is due to the non-perturbative resonance structure of the higher members of the ψ family, $\psi(4040)$, $\psi(4160)$ and $\psi(4415)$, whose collective structure is too deeply intertwined to permit an accurate determination of their contribution to $\Delta\alpha^{(5)}_{\rm had}(M_Z^2)$ using Breit-Wigner parameterizations.

In lieu of a satisfactory theoretical parameterization, we resort to the measured cross-section in this interval to use as input into the dispersion integral (1.15). The region has been measured comprehensively by five separate collaborations, and so in principle the charm threshold ought to be very well resolved. However the older data sets, Crystal Ball [23], MARK I [24], DASP [25] and PLUTO [26], all suffer individually from uncertain overall normalizations. Moreover, in the continuum regions well above and below the threshold, where we believe perturbative QCD to give a good description of the cross-section, the data are slightly incongruous with the theory prediction. Fortunately, there exist means by which we are able to determine the appropriate normalization for the data.

Following the examples of [7, 40], in an effort to suppress the error arising from the charm threshold, we use the perturbative QCD calculation of the R-ratio in the continuum regions straddling the threshold in order to rescale the data in line with the theoretical prediction. In this manner we fix the normalization of the data *globally* and in particular obtain a cleaner mutual description throughout the resonance interval.

We define a χ^2 in the following way, and obtain a set of rescaling factors, $\{\lambda_j\}$ by which we normalize the data to the perturbative expectation of the R-ratio at $\mathcal{O}(\alpha_s^3)$ as described in Section 1.4,

$$\chi^2 = \sum_{i \notin \text{charm}} \left\{ \frac{\lambda R_i^{\rm exp}(x_i) - R^{\rm pQCD}(x_i)}{\Delta_i^{\rm exp}} \right\}^2 .$$

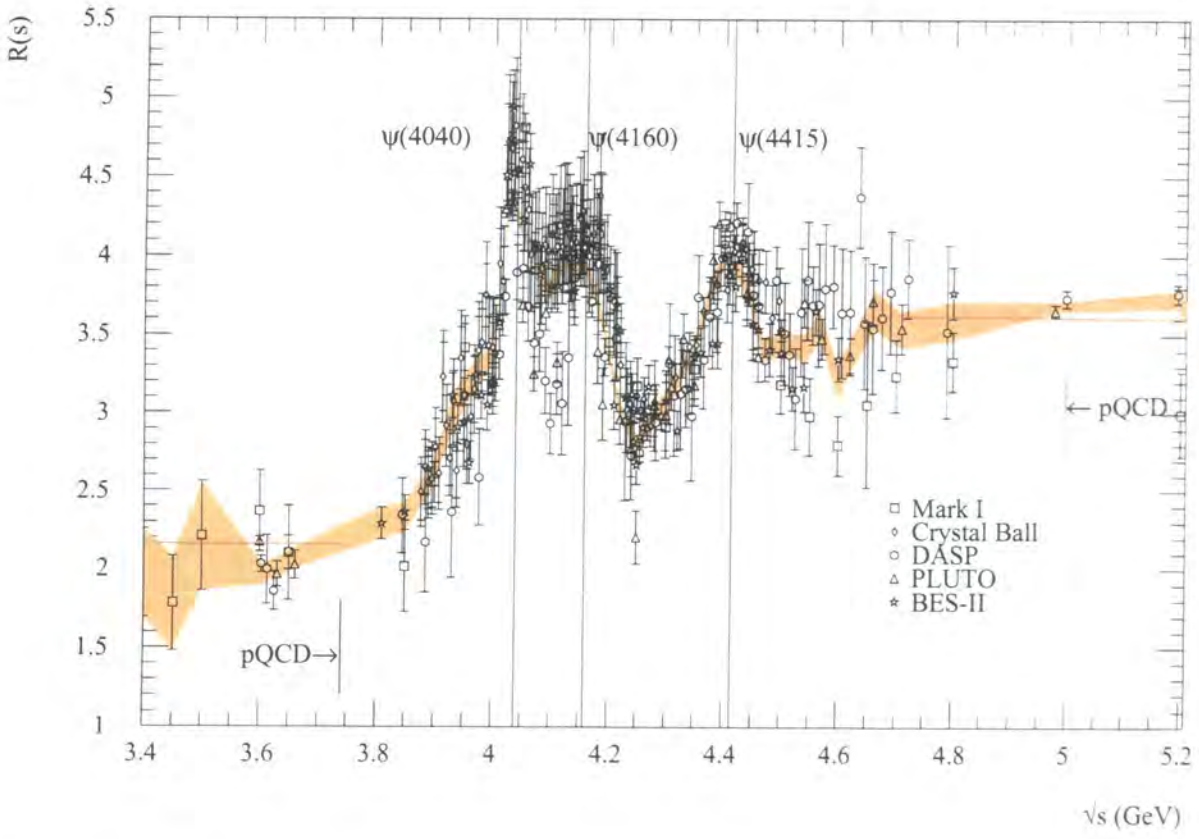

Figure 1.11: The quantity $R(s)$ in the vicinity of the physical charm threshold $3.74 \lesssim \sqrt{s} \lesssim 5$ GeV. Data from this region suffered from large overall normalization errors, this has been addressed by rescaling the data to the perturbative QCD prediction in the continuum regions safely above and beneath threshold. The plotted data have been rescaled by the factors given in Table 1.2, and the broad resonance structure of the higher members of the ψ family are quite distinct. To guide the eye, vertical lines denoting the position of the $\psi(4040)$, $\psi(4160)$ and $\psi(4415)$ resonance centres have been superimposed. The orange band illustrates the interpolation deriving from the compilation of rescaled data, and the perturbative prediction for R to $\mathcal{O}(\alpha_s^3)$ is depicted in the continuum in red.

We check that the scaling parameters λ^+ and λ^- corresponding to data above and below

Measurement	λ^-	λ^+	N^-	N^+
MARK I	0.84	0.84	11	51
DASP	0.94	0.85	4	21
PLUTO	0.96	0.94	3	24

Table 1.2: Rescaling parameters for the data sets describing the charm threshold. $\lambda^{\pm}$ describe the appropriate scaling factor above and below threshold, whilst $N^{\pm}$ gives the number of data points in the straddling continuum regions to fit to perturbative QCD.

threshold respectively are mutually consistent, as is apparent from Table 1.2. Taking an average in each of the continuum regions we obtain global scaling factors for the MARK I data of 0.84, the DASP data of 0.88 and the PLUTO data of 0.95. The Crystal Ball data are encompassed completely by the charm threshold and so afford no opportunity to extract a rescaling variable by reference to the continuum. These are left unmodified. The Beijing data are in good agreement with the perturbative prediction and require no manipulation. The data sets are then scaled according to the scheme outlined above. We presume to have nullified the systematic error of the normalized data in the region, and combine the five sets using the covariance matrix technique of (1.24), to obtain an interpolation throughout the threshold.

The results are illustrated in Fig. 1.11, which shows clearly the resolved structure in the region. The broad higher resonances of the $\psi(4040)$, $\psi(4160)$ and $\psi(4415)$ are apparent, and the combined fit joins smoothly (by construction) onto the perturbative predictions for R in the continuum regions, at $\sqrt{s} = 3.74$ GeV and $\sqrt{s} = 5$ GeV. Integrating the interpolated result through charm threshold we obtain a contribution to the hadronic part of the running of the fine structure constant of 15.13 ± 0.36.

1.5.4 Bottom threshold, $\sqrt{s} \simeq 10.56$ GeV

Ideally we would be able to extract the bottom threshold in exactly the same way as for the charm threshold. Unfortunately, this region has been measured only coarsely by a handful of experiments, rendering meaningless an analogous interpolation. In fact, it is not apparent that

the data resolve any genuine structure at all beyond statistical fluctuation.

We treat this interval using the perturbative prediction for the R-ratio as the interpolation through the region, and a physical bottom threshold delineating the four to five flavour transition at $\sqrt{s} = 2m_{B^{\pm}} = 10.56$ GeV. Whilst formally perhaps not ideal, the paucity of the data do not allow a more aesthetic treatment. We further justify this particular ansatz by noting that the resonances of the Υ family are *extremely* narrow, and that a similar disruption to the smooth cross-section as that witnessed in the charm threshold region is unlikely. The perturbative prediction should give an adequate description, and is certainly consistent with the sparse data. Moreover, as we are now at comparatively high energies, the suppression of the R-ratio by the weight function under the dispersion integral is significant - deviation from the central value obtained will be rather minimal.

The contribution to the hadronic part of the running coupling arising from the bottom threshold is then taken as the linear superposition of the narrow Breit-Wigner resonance states of the Υ family with the theoretical QCD prediction. These are again included in Section 1.5.5.

1.5.5 Breit-Wigner resonance parameterizations, ω, ϕ, ψ's, Υ's

We have seen how the smooth R continuum is disrupted by non-perturbative resonance states whose contribution cannot be deduced by the fixed order perturbative expansion. The broad overlapping resonances have been included by means of a data interpolation, and following the prescription of [8], we are able to safely parameterize the distinct narrow resonances of the ω and ϕ in the low energy region, and the higher ψ and Υ families around the $c\bar{c}$ and $b\bar{b}$ thresholds respectively by means of a Breit-Wigner model with parameters from global fits to data [6].

For the 'larger' narrow resonance states we implement the relativistic Breit-Wigner resonance model for the hadronic cross-section contribution with an s-dependent width,

$$\sigma_{\mathrm{BW}}(s) = \frac{12\pi}{M_R^2}\frac{\Gamma_{ee}}{\Gamma_R}\frac{M_R^2\Gamma_R\Gamma(s)}{(s-M_R^2)^2 + M_R^2\Gamma^2(s)}, \tag{1.26}$$

where $\Gamma(s) \simeq s\,\Gamma_R/M_R^2$ above the thresholds, the Γ_R are the resonance widths and Γ_{ee} represents the partial electronic width.

For sufficiently narrow resonances we can safely make a further approximation, that of zero width resonances, approximating the resonance contribution as a simple pole where the cross-section contribution is given by

$$\sigma_{\rm NW}(s) = \frac{12\pi^2}{M_R}\Gamma_{ee}\delta(s - M_R^2). \tag{1.27}$$

The ω and ϕ resonances are sufficiently large to demand the use of the relativistic Breit-Wigner (1.26) with an s-dependent width given by the form [41],

$$\Gamma_R(s) = \sum_i \Gamma(R \to X_i, s) = \frac{s}{M_R^2}\Gamma_R \sum_i Br(R \to X_i)\frac{F_{X_i}(s)}{F_{X_i}(M_R^2)}$$

where $R = \omega, \phi$ and the $\{X_i\} = \{3\pi, \pi^0\gamma, 2\pi\}$ and $\{K^+K^-, K_SK_L, 3\pi, \pi^0\gamma, \eta\gamma\}$ decay modes respectively. $Br(R \to X_i)$ denotes the branching ratio for the channel X_i, taken from [6], and $F_{X_i}(s)$ is the phase space function for the channel X_i, approximated by the two-body[7] decay, $F_{p_1p_2} = \left[1 - (m_1 + m_2)^2/s\right]^{3/2}$. We show the resonance contributions to $\Delta\alpha^{(5)}_{\rm had}(M_Z^2) \cdot 10^4$ in Table 1.5.5. The ψ-family are evaluated using (1.26), whilst the Υ-family are sufficiently fine to

Resonance	Contribution to $\Delta\alpha^{(5)}_{\rm had}(M_Z^2) \cdot 10^4$
ω	3.07 ± 0.10
ϕ	5.08 ± 0.19
Narrow ψ-family	9.41 ± 0.53
Narrow Υ-family	1.22 ± 0.04

Table 1.3: Contributions arising from the Breit-Wigner resonance parameterizations. The ω and ϕ are evaluated using a relativistic s-dependent width Breit-Wigner, the narrow higher resonances with a narrow width approximation. The broad $\psi(4040)$, $\psi(4160)$ and $\psi(4415)$ are explicitly resolved in the charm threshold region, and not included here.

justify the use of the narrow width approximation, (1.27).

[7]The three pion decay channel is dominated by the mode $R \to \rho\pi \to 3\pi$ which can be used to approximate exact form.

1.6 Direct evaluation of $\alpha(M_Z^2)$ in the timelike region

We collate the complete list of hadronic contributions to $\Delta\alpha^{(5)}_{\rm had}(M_Z^2)\cdot 10^4$ discussed above, and their origins in Table 1.4. The bracketed entries are the complementary results of parallel eval-

$\sqrt{s}$ interval (GeV)	$\Delta\alpha^{(5)}_{\rm had}(M_Z^2)\cdot 10^4$ contribution	Origin of contribution
$2m_\pi - 1.46^a$	$38.76 \pm \left\{ \begin{array}{l} 0.52 \\ 0.60^b \end{array} \right\}$	Pion form factor data
1.46 - 1.90	$\left\{ \begin{array}{l} 8.62 \pm 0.60^c \\ 10.32 \pm 1.06^b \end{array} \right.$	$\left\{ \begin{array}{l} \text{Inclusive data} \\ \text{Exclusive summation} \end{array} \right.$
1.90 - 2.80	$\left\{ \begin{array}{l} 13.26 \pm 0.83^c \\ 13.79 \pm 0.83 \end{array} \right.$	$\left\{ \begin{array}{l} \text{Inclusive data} \\ \text{Exclusive summation} \end{array} \right.$
2.80 - 3.74	9.73 ± 0.05^d	Perturbative QCD
3.74 - 5.00	15.13 ± 0.36	Charm data*
5.00 - ∞	169.97 ± 0.64^d	Perturbative QCD
ω, ϕ, ψ's, Υ's	18.79 ± 0.58	Breit-Wigner resonances
$\Delta\alpha^{(5)}_{\rm had}(M_Z^2)\cdot 10^4$	$\left\{ \begin{array}{l} 274.26 \pm 1.90 \\ 276.49 \pm 2.14 \end{array} \right.$	$\left\{ \begin{array}{l} \text{Inclusive data} \\ \text{Exclusive summation} \end{array} \right.$
$\alpha^{-1}(M_Z^2)$	$\left\{ \begin{array}{l} 128.972 \pm 0.026 \\ 128.941 \pm 0.029 \end{array} \right.$	$\left\{ \begin{array}{l} \text{Inclusive data} \\ \text{Exclusive summation} \end{array} \right.$

Table 1.4: Full series of results contributing to the hadronic component of the shift in fine structure constant, $\Delta\alpha^{(5)}_{\rm had}(M_Z^2)\cdot 10^4$. The upper (lower) error in the result labelled ^{a} corresponds to the 2π (remaining) exclusive channels. Contributions labelled with superscripts ^{b}, ^{c} and ^{d} have common error sources which are added linearly. Remaining errors are added in quadrature. The perturbative contribution is determined using the prescription of Section 1.4. The data sets through the charm threshold interval marked * have had their normalizations fixed in accordance with Section 1.5.3.

uations using the prescription of either inclusive data or a summation of exclusive annihilation channels in the low energy region. It is apparent that the chief components of the errors arise in the low energy regions $2m_\pi$ – 2.8 GeV. In order for any further significant reduction in the uncertainty on central values, it will be necessary for clearer experimental determination of the low energy cross-sections, particularly in the ambiguous regions of overlapping inclusive and exclusive measurements. We find a non-negligible difference between the two evaluations,

approximately 2.2 units of $\Delta\alpha^{(5)}_{\rm had}(M_Z^2)\cdot 10^4$, which will lead to a distinct difference in predictions for $\alpha^{-1}(M_Z^2)$.

The hadronic contributions are now combined with the the leptonic $\Delta\alpha_{\rm lep}(M_Z^2)\cdot 10^4 = 314.98$ and top $\Delta\alpha^{\rm top}(M_Z^2)\cdot 10^4 = -0.76$ contributions in Eqn. (1.5) to evaluate the running of the fine structure constant to the Z-pole. The two parallel inclusive and exclusive calculations yield respectively

$$\alpha^{-1}(M_Z^2) = 128.972 \pm 0.026 \text{ and } \alpha^{-1}(M_Z^2) = 128.941 \pm 0.029. \tag{1.28}$$

We see that the introduction of new data has considerably improved the error of $\Delta\alpha^{(5)}_{\rm had}(M_Z^2)$, although there remains some unresolved discrepancy between the parallel evaluations. It might be argued that the precise BES-II data (which agree well with QCD in the safe continuum regions) favour the inclusive data on the grounds of smoothness and continuity in the region of $\sqrt{s} \sim 2$ GeV, but this is by no means a conclusive argument.

1.6.1 Comparison with the literature

It will be instructive to present a discussion of how this evaluation differs to that of the 'industry standard' obtained by Eidelman and Jegerlehner in [8]. This analysis is constructed so as to be the most immune to model dependencies, and used strictly the available data to parameterize the R-ratio through to $s = 40$ GeV, and beyond this point perturbative QCD to evalulate R for the tail of the integrand. This carefully empirical evaluation details a total hadronic contribution to the vacuum polarization function of $\Delta\alpha^{(5)}_{\rm had}(M_Z^2)\cdot 10^4 = 280.37 \pm 6.54$, where the large error is endemic of the varying quality of the data available. It may be argued that this reliance on data in regions where perturbative QCD is believed to be much more reliable (for instance $\sqrt{s} \gtrsim 15$ GeV) is a deficiency in this analysis, indeed, in later work the same authors place more reliance on the theoretical determination of R [42]. Since this evaluation was carried out, many supplemental experiments have been performed [30, 34, 35, 36, 37], refining considerably the data interpolations of the R-ratio, particularly the exclusive two and four pion channels in the low energy regions, and the inclusive Beijing data, whose influence was discussed in Sections 1.5.2.

It will be a worthwhile exercise decomposing the contributions by energy interval origin in order to clarify exactly where the shift in central value, and tightening of the error bands arise.

The two contrasting spectra of contributions are listed below, decomposed according to the energy intervals of [8].

Final state	$\sqrt{s}$ interval (GeV)	Contribution from [8]	Current evaluation
ρ	$2m_\pi$ - 0.81	26.08 ± 0.68	25.32 ± 0.52
ω	0.42 - 0.81	2.93 ± 0.09	3.07 ± 0.10
ϕ	1.00 - 1.04	5.08 ± 0.14	5.08 ± 0.19
J/ψ		11.34 ± 0.82	9.41 ± 0.53 (+1.93=11.35)
Υ		1.18 ± 0.08	1.22 ± 0.04
hadrons	0.81 - 1.40	13.83 ± 0.80	12.24 ± 0.54
hadrons	1.40 - 3.10	27.62 ± 4.02	$1.40-1.46$ 1.21 ± 0.07 Exc. $1.46-2.8$ 21.88 ± 1.43 Inc. $2.8-3.10$ 3.43 ± 0.02 pQCD.
hadrons	3.10 - 3.60	5.82 ± 1.16	5.02 ± 0.03
hadrons	3.60 - 9.46	50.60 ± 3.33	$3.60-3.74$ 1.28 ± 0.01 pQCD. $3.74-5.0$ 15.13 ± 0.36 Inc. $5.0-9.46$ 35.51 ± 0.21 pQCD.
hadrons	9.46 - 40.0	93.07 ± 3.50	91.77 ± 0.19
perturbative QCD	40.0 - ∞	42.82 ± 0.10	42.70 ± 0.24
Total	$2m_\pi$ - ∞	280.37 ± 6.54	274.26 ± 1.90

From threshold for hadronic production through the ρ resonance interval there is a net deficit of some 0.7 units in the central value of this analysis of $\Delta\alpha^{(5)}_{\rm had}(M_Z^2)\cdot 10^4$, and a considerable reduction in its error estimate, between the two evaluations. This can be ascribed to the inclusion of valuable new data obtained from the VEPP-2M Novosibirsk experiments in this later analysis [30, 34, 35, 36, 37]. The interval $0.81 \leq \sqrt{s} \leq 1.4$ GeV contains the largest single discrepancy, around 1.6 units, between the two evaluations. Both analyses sum exclusive channels to determine the R-ratio in this interval, and again the discrepancy can be allocated to the extension of the data compilation by later experiments.

The contributions generated from the $1.4 \leq \sqrt{s} \leq 3.1$ GeV show a mismatch of some 1.2 units. Both evaluations nominally use the inclusive data through this region, however since the earlier analysis, the Beijing data have become available. These lie systematically beneath (and in agreement with the perturbative QCD prediction) in the subinterval of $2 \lesssim \sqrt{s} \lesssim 2.8$ GeV, and by dint of their better resolution, now dominate the interpolation through the updated

data compilation. The broad structure denoted by the older data has been almost completely suppressed, and accounts for the large shift in central value, whilst the greater accuracy of the Bes-II measurements has really defined the data parameterization much more clearly, explaining the dramatic decrease in the error of the contribution.

In contrast with the earlier determinations insistence on data, given the degree of sophistication to which the perturbative contribution is determined, we feel safe in implementing a theoretical description through $3.1 \leq \sqrt{s} \leq 3.6$ GeV. The older data compilation here consists solely of the MARK 1 and PLUTO data, whose normalization uncertainties were discussed in Section 1.5.3. These data overrepresent the perturbative QCD prediction in the continuum regions above and below the charm threshold, Table 1.2, and so we nominally anticipate a 15% excess in a contribution determined from these raw inclusive measurements compared with that of a theoretical determination, which is evident from the table.

The interval $3.6 \leq \sqrt{s} \leq 9.46$ generates another sizeable net contribution, some 1.3 units, to the shift in the respective central values. This is not the complete story however - there are competing systematic differences between the two evaluations in this broad interval which to a greater extent cancel. As above we might expect a decrement in contribution of about 15% purely from the evaluation of the charm threshold, from the rescaling of the charm data to the perturbative expectation in the continua. This would generate a gross difference of almost 3.5 units were it not for the fact that the data describing the continuum above threshold, $\sqrt{s} \lesssim 7$, (where we have substituted perturbative QCD) lie systematically *beneath* the theoretical expectation.

There has been another significant reduction in error arising from the interval. This has been achieved by two mechanisms, firstly the normalization of the old data describing the charm threshold has been determined by reference to QCD in the continuum - the systematic errors are nullified, and secondly, in the continuum regions away from threshold we make use of the theoretical description of R which is more reliable than the data interpolation.

Beyond this region and up to the onset of the high energy tail, $9.46 \leq \sqrt{s} \leq 40$ GeV, the earlier analysis again uses an R interpolation generated from the data compilation. The sparseness and crudity of the data makes this inappropriate. A comparison with the QCD prediction,

Fig. 1.7, shows that the interpolation will inherit sizeable spurious fluctuations and shape artifacts from the experimental measurements. At these energies we can believe perturbative QCD and again use the theoretical evaluation of R. Deviation from the theory prediction by the measurements, despite the weight suppression associated with the integration kernel at high energies, account for the the significant difference in central values. The theoretical prediction has a naturally lower error associated with it, the prediction is not so sensitive to the mass parameters away from the thresholds, and at $\mathcal{O}(\alpha_s^3)$ it exhibits only slender susceptibility to changes in the scale.

We see that the resonances are generally in good agreement, which is to be anticipated - their contribution being well defined by a family of Breit-Wigner resonance shapes subject to parameters obtained globally by the Particle Data Group.

Final the high energy tails beyond 40 GeV are both described using theoretical predictions of the imaginary part of the vacuum polarisation function. We find marginal deviation in the two results, consistent with slight differences in the input parameters.

1.7 The Standard Model Higgs mechanism

The $W^{\pm}$ and Z gauge bosons, which ensure local gauge invariance in the Standard Electroweak Model [3] are required to possess no explicit mass terms in the Lagrangian density if the theory is to remain renormalizable. The reconciliation of the apparent masslessness of these particles with the empirical fact that they possess large masses, $M_W \simeq 80.3$ and $M_Z \simeq 91.2$ GeV , is resolved by the *Higgs mechanism* [43].

A complex doublet of scalar (Higgs) fields is added to the existing particle spectrum,

$$\phi = \begin{pmatrix} \phi^+ \\ \phi^0 \end{pmatrix},$$

with a contribution to the electroweak Lagrangian density of the form

$$\mathcal{L} = \frac{1}{2} D_\mu \phi \cdot D^\mu \phi - V(\phi), \tag{1.29}$$

where the *covariant derivative* is given by $D_\mu\phi = (\partial_\mu - \frac{i}{2}g\vec{W}_\mu \cdot \vec{T} - \frac{i}{2}g'B_\mu)\phi$, and the *Higgs potential* is given by $V(\phi) = \lambda(\phi^\dagger\phi)^2 - \mu^2\phi^\dagger\phi$. The crucial choice of the parameters λ, $\mu^2 > 0$ generates minima *away* from the origin, Fig. 1.12. The minima of this potential are degenerate

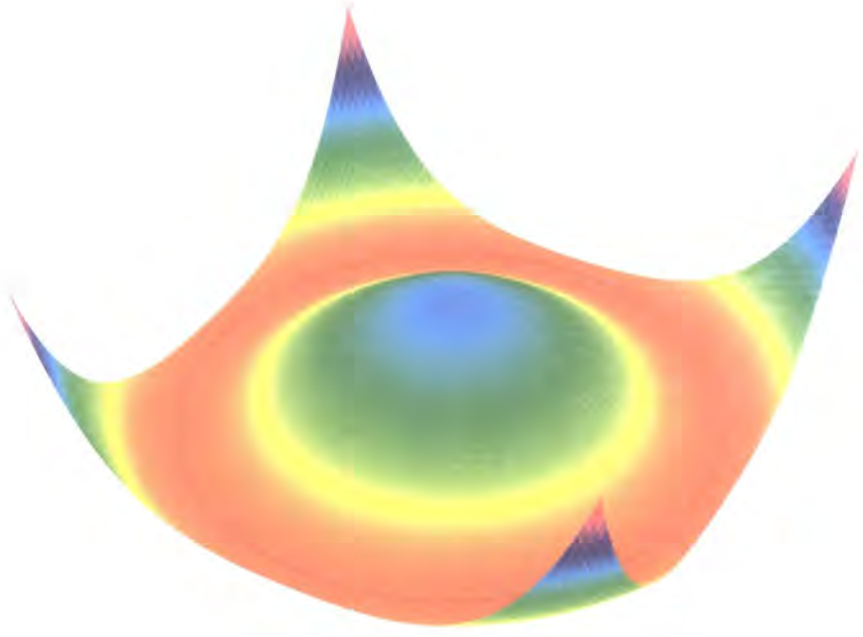

Figure 1.12: The scalar Higgs potential, $V(\phi)$, with complex degrees of freedom suppressed. The characteristic 'wine-bottle' shape of the potential is evident, and the degenerate continuous minima satisfying Eqn. (1.30) are shown as the red curve.

and continuous and lie on the contour

$$|\phi| = \sqrt{\frac{\mu^2}{2\lambda}} \equiv \frac{v}{\sqrt{2}}. \tag{1.30}$$

The symmetry is broken by making a particular selection of minimum for ϕ, local gauge invariance ensures that three of the four degrees of freedom can be phased away[8], and considering only perturbations about the (arbitrary) choice of minimum, the ϕ field has the reparameterization

$$\phi(x) = \frac{1}{\sqrt{2}}\begin{pmatrix} 0 \\ v + h(x) \end{pmatrix}.$$

[8]To reappear as the extra longitudinal modes necessary for massive $W^\pm$ and Z gauge bosons.

Substituting this back into Eqn. (1.29), a Lagrangian density is obtained with the appropriate Standard Model electroweak particle content corresponding to three massive particles, the $W^{\pm}$ and Z^0, and one massless field, the photon γ. The eigenstates of the charge operator and their respective masses are written

$$\begin{aligned} W_\mu^{\pm} &= \frac{1}{\sqrt{2}}(W_\mu^1 \pm iW_\mu^2) && \text{with mass } M_W^2 = \frac{g^2v^2}{4}, \\ Z_\mu = \frac{gW_\mu^3 - g'B_\mu}{\sqrt{g^2+g'^2}} &= \cos\theta_W W_\mu^3 - \sin\theta_W B_\mu && \text{with mass } M_Z^2 = \frac{g^2v^2}{4\cos^2\theta_W} = \frac{M_W^2}{\cos^2\theta_W}, \\ A_\mu = \frac{g'W_\mu^3 + gB_\mu 2}{\sqrt{g^2+g'^2}} &= \sin\theta_W W_\mu^2 + \cos\theta_W B_\mu && \text{with mass } M_\gamma^2 = 0. \end{aligned}$$

The remaining degree of freedom, h, corresponds to a neutral scalar particle, the Higgs, whose mass is determined by the parameters of the Higgs potential, $M_H = \sqrt{2}\mu = \sqrt{2\lambda}v$. One of these parameters is left undetermined by the defining electroweak parameters, and so the Higgs mass must be extracted empirically, ideally through direct observation of a signal. In lieu of a direct measurement, we also have the capacity to constrain the Higgs mass by performing global fits of the world electroweak data to higher order Higgs corrections.

1.7.1 χ^2 fit for the SM Higgs mass

The electroweak observables are sensitive to the Higgs mass through a variety of radiative corrections. As an example, the one-loop correction to the relation between the mass of the W and the electroweak parameters reads [44]

$$1 - \frac{M_W^2}{M_Z^2} = \frac{1}{2}\left\{1 - \left[1 - \frac{4\pi\alpha}{\sqrt{2}G_F M_Z^2(1-\Delta r)}\right]^{1/2}\right\}$$

where the function Δr, containing the dependence on the mass of the top and Higgs, is written

$$\Delta r \simeq \Delta\alpha + \frac{G_F}{8\sqrt{s}\pi^2}\left\{-3\cot^2\theta_W m_t^2 + \frac{11}{3}M_W^2 \log\frac{M_H^2}{M_W^2}\right\} + ...$$

Given the determinations of the electroweak parameters $\alpha(M_Z^2)$, G_F and M_Z and the measurements of M_W and m_t [6] it is possible to bound the Higgs mass.

The correction to the W mass is logarithmically dependent on M_H, and quadratically dependent on m_t, this latter not being sufficiently well determined to usefully limit the former.

Fortunately, there exist a variety of expressions relating experimentally observable quantities to the defining parameters of the electroweak sector - the best estimate of the Higgs mass is then most effectively made by performing a global fit in *all* the relevant expressions to *all* the available electroweak data, a task performed by the LEP and SLD Electroweak Working Group [45].

Using the favoured inclusive value $\alpha^{-1}(M_Z^2) = 128.972 \pm 0.026$ of the current analysis, the Electroweak Working Group performed global χ^2 minimizations to the Standard Model Higgs boson mass, M_H, using the sum of presently available electroweak data [46]. A striking minimum was found in χ^2 at $M_H = 110$ GeV, which lies close to, but fractionally above, the direct LEP2 exclusion bound[9] which is to be contrasted with the minimum generated by the larger value of $\Delta\alpha^{(5)}_{\rm had}(M_Z^2) \cdot 10^4$ of previous determinations which lie significantly within the exclusion zone, Fig. 1.13. We conclude that the present experimental status of direct Higgs searches and global electroweak data more comfortably accomadates the consistency of the Standard Model Higgs with a smaller value of $\Delta\alpha^{(5)}_{\rm had}(M_Z^2) \cdot 10^4$ than is presently widespread.

[9]We note that there are a few events seen at the highest LEP2 energy which are consistent with a Higgs of mass about 115 GeV, but that such a signal needs confirmation [47]

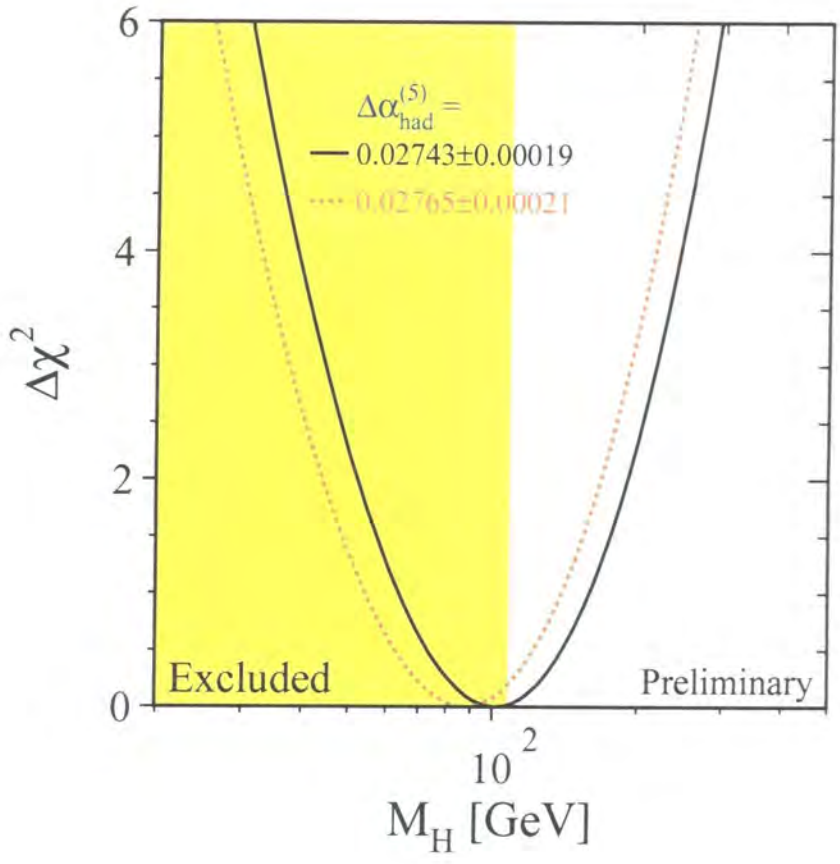

Figure 1.13: χ^2 fit as a function of the standard model Higgs mass, M_H, using the latest compilation of electroweak data. The black solid line and the red dashed line correspond to the use of the determinations of $\Delta\alpha^{(5)}_{\rm had}(M_Z^2)\cdot 10^4$ of 274.3 ± 1.9 for the inclusive data and 276.5 ± 2.1 for the exclusive data respectively in the low energy region of the dispersion integral. The yellow zone to the left illustrates the energy interval where the Higgs has been excluded due to direct searches at LEP2. Note that these χ^2 profiles do not illustrate the inherent experimental uncertainties in $\Delta\alpha^{(5)}_{\rm had}(M_Z^2)$.

Chapter 2

Analytic continuation and the charm pole mass

In this second chapter we investigate the potential for further reducing the error on $\alpha(M_Z^2)$ by using analytic continuations of the hadronic contribution to the vacuum polarization amplitude between the regions of *timelike*, $s > 0$, and *spacelike*, $s < 0$, energy domains. We illustrate how the inherent sensitivity of the perturbative QCD description at threshold to the charm pole mass parameter, m_c, is sufficient to negate hope of bettering the 'direct' evaluation of Chapter 1 in the timelike zone. However, by demanding consistency between the $\Delta\alpha^{(5)}_{\rm had}(M_Z^2)$ obtained via the two complementary methods, we are able to (i) obtain an estimate of the magnitude of m_c and quantify an associated error, and (ii) shed light on the ambiguity between the distinct determinations of R evaluated from the inclusive interpolation and summed exclusive channels in the low energy domain $1.5 \lesssim \sqrt{s} \lesssim 2$ GeV.

2.1 Constraining $\Delta\alpha^{(5)}_{\rm had}(M_Z^2)$ through analytic continuation?

Recalling that the chief impediment to greater stringency in constraining the predictions of the mass of the Standard Model Higgs is the hadronic contribution to vacuum polarization whose dominant source of error arises from data interpolation at low energies, it is not surprising that

substantial effort has been made in attempting to better negotiate the inherent uncertainty. In lieu of a systematic and comprehensive series of experimental reevaluations of the low energy region to better resolve the current error, focus has shifted to ways in which the experimental uncertainty might be circumnavigated by more theoretical sleights of hand.

Recent developments involve exploiting the analytic behaviour of $\Delta\alpha^{(5)}_{\rm had}(s)$ and performing a continuation throughout the plane of complex s. The suggestion of [48, 10] is to suppress the data contribution within the dispersion integral with specially selected polynomial functions, subtracted from the weight function, in the regions where the data is problematic. The suppressed contribution is compensated by adding the same polynomial weight integral, but now continued along circular contours from the spacelike domain and using perturbative QCD, condensate contributions and global duality arguments. The authors obtain a hadronic contribution to vacuum polarization of

$$\Delta\alpha^{(5)}_{\rm had}(M_Z^2)\cdot 10^4 = 277.6 \pm 4.1.$$

However we see from Fig. 1.10 that QCD fails to reproduce the the structure of the data for R in the region. The error inherent in this interval is sufficent to negate the gain in accuracy from the contour trick, and we conclude that studies of this type cannot circumvent the low energy measurements of R and their uncertainties.

An alternative proposal using the complex structure of $\hat{\Pi}(s)$ was proposed by Jegerlehner in [42]. Again a spacelike evaluation of the hadronic contribution to vacuum polarization is used. The dispersion integral (1.15) now reads

$$\Delta\alpha^{(5)}_{\rm had}(-s) = \frac{\alpha s}{3\pi}\int_{4m_\pi^2}^{\infty}\frac{ds'}{s'}\frac{R(s')}{(s'+s)}, \tag{2.1}$$

and moreover, the hadronic contribution to the vacuum polarization function from perturbative QCD can be evaluated directly as $\hat{\Pi}$ is expressly real in the spacelike domain,

$$\Delta\alpha^{(5)}_{\rm had}(-s) = -4\pi\alpha{\rm Re}\hat{\Pi}(-s) = -4\pi\alpha\hat{\Pi}(-s). \tag{2.2}$$

We can calculate the quantity $\Delta\alpha_{\rm had}(-s_0)$ at large *negative* values of $s=-s_0$, and then use perturbative QCD to analytically continue along the negative real axis to $s=-M_Z^2$, and then subsequently continue around the large semicircle to the timelike mass of the Z-boson, where it

is useful for precision electroweak phenomenology. The procedure is algebraically formulated as

$$\Delta\alpha^{(5)}_{\rm had}(-M_Z^2) = \left[\Delta\alpha^{(5)}_{\rm had}(-M_Z^2) - \Delta\alpha^{(5)}_{\rm had}(-s_0)\right]^{\rm QCD} + \Delta\alpha^{\rm data}_{\rm had}(-s_0). \tag{2.3}$$

We make substantial use of QCD in the spacelike domain, safely far away from threshold and bound state effects which lie in the timelike region and where, in principle, it is an accurate description of QCD physics. We should choose s_0 such that a perturbative treatment is valid - we need it sufficiently large to justify the neglect of contributions from parton condensates, and it transpires that the choice $|s_0| \gtrsim 6$ GeV^2 is sufficient to suppress these non-perturbative effects [42].

The final continuation around the large semicircle from spacelike $s = -M_Z^2$ to timelike $s = M_Z^2$ was investigated in [42], and the associated error proved to be negligible,

$$\Delta\alpha^{(5)}_{\rm had}(M_Z^2) = \Delta\alpha^{(5)}_{\rm had}(-M_Z^2) + (0.45 \pm 0.02)\cdot 10^{-4}.$$

It can be seen that analytic continuation of Eqn. (2.3) is implicitly a weighted substitution of the R-ratio obtained from interpolated data with that of a purely perturbative QCD prediction. The most interesting experimental pieces of the R interpolation all occur at comparatively low $s \ll M_Z^2$. If we then compare the direct evaluation of $\Delta\alpha_{\rm had}(-M_Z^2)$ with the analytic continuation in the form of a purely QCD dispersion integral (2.1) the net effect is to make the replacement

$$R^{\rm data}(s') \to \frac{s_0 R^{\rm data}(s') + s' R^{\rm QCD}(s')}{s_0 + s'}.$$

For $s' \ll s_0$ we retain the full data interpolation intact, for $s' \gg s_0$ we discard all the data in favour of the perturbative prediction, whilst in the interim, for $s' \sim s_0$, a mixture of the data and QCD is utilized. The lower we are able to reliably force s_0, the smaller will be the net data contribution to the evaluation of $\Delta\alpha^{(5)}_{\rm had}(\pm M_Z^2)$, and correspondingly the uncertainty on the total hadronic contribution to vacuum polarization from measurements is diminished.

Before lauding this ingenious formalism, we must investigate the error associated with the perturbative QCD continuation from $s = -s_0$ to $s = -M_Z^2$, that is, the error on the quantity $\delta^{\rm QCD}(s_0)$, defined by

$$\delta^{\rm QCD}(s_0) = \left[\Delta\alpha^{(5)}_{\rm had}(-M_Z^2) - \Delta\alpha^{(5)}_{\rm had}(-s_0)\right]^{\rm QCD} = -4\pi\alpha \int_{-s_0}^{-M_Z^2} ds' \frac{d\Pi(s')}{ds'}.$$

Unfortunately, it transpires that the parameters defining the QCD description of the vacuum polarization function (specifically the pole masses corresponding to the QCD heavy quark thresholds) are not sufficiently well determined to allow this technique to supplant the error on $\Delta\alpha^{(5)}_{\rm had}(M_Z^2)$ from the direct evaluation. The dominant source of error arises from uncertainty in the value of the pole mass of the charm quark.

We can generate an estimate of the sensitivity of the continuation technique to m_c by considering the dominant $\mathcal{O}(1)$ contribution to $\delta^{\rm QCD}(s_0)$. This can be determined by the expression

$$\left[\Delta\alpha^{(5)}_{\rm had}(-M_Z^2) - \Delta\alpha^{(5)}_{\rm had}(-s_0)\right]^{\rm QCD,(0)} = \frac{\alpha Q_c^2}{3\pi}(M_Z^2 - s_0)\int_{4m_c^2}^{\infty} ds' \frac{R_c^{(0)}}{(s+M_Z^2)(s+s_0)} \qquad (2.4)$$

where $R_c^{(0)}$ is given by Eqns. (1.11) and (1.19), and obviously retains the complete mass dependence. For the spectrum of charm masses, $m_c = 1.6,\ 1.4,\ 1.2$ GeV, and $s_0 = 6$ GeV^2, with associated QCD thresholds depicted in Fig.2.1, we obtain contributions to the QCD continuation of $\delta(6)^{\rm QCD} \cdot 10^4$ of 62.36, 64.17 and 66.05 respectively - as the charm mass spans $1.2 \lesssim m_c \lesssim 1.6$ GeV, $\delta^{\rm QCD,(0)}(s_0) \cdot 10^4$ varies by 4 units!

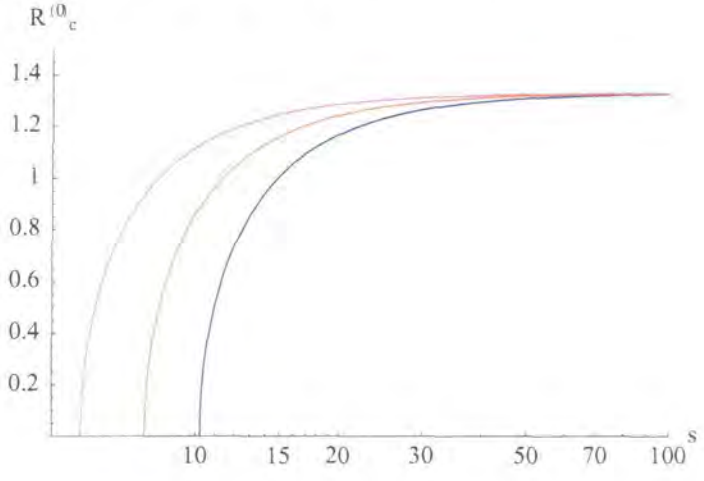

Figure 2.1: The $\mathcal{O}(1)$ charm contribution to the R ratio with exact mass dependence of the real part of (1.19), for a spanning sample of charm pole masses, $m_c = 1.6$ GeV in blue, $m_c = 1.4$ GeV in red and $m_c = 1.2$ GeV in magenta. Note the sizeable shift in QCD threshold position with relatively slight variation in mass parameter.

It is apparent that the uncertainty from the QCD continuation from $-s_0$ to $-M_Z^2$ threatens to

overwhelm the error arising from the direct evaluation, and that this error is chiefly attributable to the error on the charm pole mass. We are forced to conclude that there is no advantage to be gained by evaluating $\Delta\alpha^{(5)}_{\rm had}(M_Z^2)$ via this circuitous route in the complex plane until the charm pole mass m_c can be (independently) better constrained.

Approaching the problem from an alternative perspective, believing perturbative QCD in the spacelike region away from threshold and low energy effects as an accurate description of the physics to hand, by demanding internal consistency between the direct and continued evaluation allows us to estimate the charm pole mass.

2.2 Analytic continuation of $\hat{\Pi}(s)$ into the spacelike domain

For a physically appropriate set of parameters, we should in principle obtain the same result for $\Delta\alpha^{(5)}_{\rm had}(M_Z^2)$, irrespective of the method of evaluation, either direct or analytically continued from *any* perturbative $-s_0$ in the spacelike region. That this is not the case is indicative of some deficiency in the description - either an inappropriate parameter set in the theoretical determination, or some wayward input in the data interpolation, or some combination of the two. We define a new function $d(s_0)$ to study the difference between the direct and analytically continued evaluations of $\Delta\alpha^{(5)}_{\rm had}(M_Z^2)$ in the following way,

$$\begin{aligned} d(s_0) &= \Delta\alpha^{(5)}_{\rm had}(M_Z^2)\,|_{\rm direct} - \Delta\alpha^{(5)}_{\rm had}(M_Z^2)\,|_{\rm continuation} \\ &= \left[\Delta\alpha^{(5)}_{\rm had}(-M_Z^2) - \Delta\alpha^{(5)}_{\rm had}(-s_0)\right]^{\rm data} - \left[\Delta\alpha^{(5)}_{\rm had}(-M_Z^2) - \Delta\alpha^{(5)}_{\rm had}(-s_0)\right]^{\rm QCD}, \quad (2.5) \end{aligned}$$

where the dependence on the parameters m_c (and m_b to a lesser extent) and renormalization scale μ is implicit. If we are able to find a meaningful and stable set of parameters such that $d(s_0) \equiv 0$, then this will be a powerful constraining argument in favour of that particular value of m_c.

The contributions $\delta^{\rm data}(s_0) \equiv \left[\Delta\alpha^{(5)}_{\rm had}(-M_Z^2) - \Delta\alpha^{(5)}_{\rm had}(-s_0)\right]^{\rm data}$, of Table 2.1 have significant components arising from threshold regions, which are interpolated from data using the procedure of section 1.5.3. As the data are independent of the QCD mass and scale parameters, $\delta^{\rm data}(s_0)$ shows minimal susceptibilty to their variation, the slight residual dependence arising

from intervals away from threshold, where stable perturbative calculations of R are used. When we compare $\delta^{\rm data}(s_0)$ and $\delta^{\rm QCD}(s_0)$, with a consistent QCD prescription, the dispersion relation and R predictions from timelike regions in the continua will *by definition* compensate the corresponding contribution from the vacuum polarization function $\hat{\Pi}$ in the spacelike domain. In essence, we are fitting the QCD form in the region to the data for R which embody the resolved broad resonance structures lying in the physical threshold, $3.74 \leq \sqrt{s} \leq 5$ GeV, and the fitted Breit-Wigner parameterizations of the lower ψ family.

The scale choice ought to characterize the interval of continuation $s_0 \leq \mu^2 \leq M_Z^2$ under consideration. We select a value $\mu = 20$ GeV as being appropriately representative of the region, and illustrate the sensitivity to scale by showing the variation associated with a shift to $\mu = 50$ GeV.

The b flavour threshold will exhibit a similar phenomenon, although lessened in magnitude due to its higher energy weighting in the dispersion integral, and smaller charge squared. However the only data input used to enumerate the b threshold arises in our prescription from the Breit-Wigner parameterization of the family of Υ resonances. The minimal amount of empirical input precludes a reliable estimation of the pole mass of the b-quark in an analagous way. In order to prevent effects from $s \simeq 4m_b^2$ tainting the charm mass investigation we subtract off all b-quark contributions in both time and spacelike domains, and restrict the number of flavours to $n_f = 4$. This permits us to cleanly isolate the systematic effects of varying the c mass.

2.2.1 Data evaluation from dispersion integral

We first perform a series of dispersion relation calculations for a variety of $s = -s_0 < 0$ in (2.1). The identical techniques for data interpolation are used, and the same prescription for evaluating the low energy regions is implemented as for the direct timelike evaluation of $\Delta\alpha^{(5)}_{\rm had}(M_Z^2)$ in Chapter 1.

For the perturbative evaluation of R, for consistency we now choose a fixed scale, $\mu = 20$ GeV, rather than $\mu^2 = s$ to avoid ambiguities inherent in allowing the argument of $\alpha_{\rm s}(\mu^2)$ to become

negative[1]. As the threshold mass effects might prove crucial, we now calculate R to $\mathcal{O}([m_q^2/s]^6)$ as described in [18] for use in the continua. The full ($n_f = 5$) set of results for $s_0 = 6$, 15, 25, 50, 100, 50^2 and M_Z^2 and the lower scale are shown in Table 2.1.

Before calculating the contribution to $\delta^{\rm data}(s_0)$ we must subtract the contibutions from the b-quark. We evaluate the perturbative contribution of R from $\sqrt{s} > 5$ GeV with $n_f = 4$ flavours, and subtract the Υ resonance family. We also need to reevalute the QCD contribution for the same spectrum of charm masses and scales that we intend to use for $\delta^{\rm QCD}(s_0)$ for the continuation to be consistent across the complex s plane.

The table illustrates the 'pinching' of the data with variation of s_0. As we move to systematically smaller s_0, these contributions to $\Delta\alpha_{\rm had}^{\rm data}(-s_0)$ from the energy intervals at higher s' become comparatively less important and the error bars from these regions are more tightly constrained by the weighting function of the dispersion integral. For $s_0 \gg s'$ the weight function behaves as $\sim 1/s'$, independent of s_0, which is reflected in the fact that the contributions from the ρ region obtained from varying s_0 above 6 GeV are almost static, whilst in the opposing limit, $s_0 \ll s'$, the weight function behaves as $\sim s_0/(s')^2$ - thus the significant contributions from the high energy parts of the integral diminish quickly with decreasing s_0, as does their uncertainty.

2.2.2 The $\mathcal{O}(1)$ and $\mathcal{O}(\alpha_s)$ QCD contributions to $d(s_0)$

We are now left with the task of evaluating the perturbative QCD contribution to $d(s_0)$, the function $\delta^{\rm QCD}(s_0) \equiv [\Delta\alpha_{\rm had}(-M_Z^2) - \Delta\alpha_{\rm had}(-s_0)]^{\rm QCD}$. In the spacelike domain, the relationship between vacuum polarization function, Π and the hadronic contribution to the running of α is direct, Eqn. (2.2), and so the $\mathcal{O}(1)$ and $\mathcal{O}(\alpha_s)$ contributions can be obtained in a straightforward manner from the machinery of section 1.4. Clearly, the threshold treatment of vacuum polarization[2] for the heavy quarks now becomes extremely important, the full mass dependent

[1] For example, it is not apparent with a scale running in the spacelike domain how one determines the number of active quark flavours.

[2] Since we care only about the difference in the vacuum polarization function at two scales, the constant subtraction term cancels and $\hat{\Pi}(-M_Z^2) - \hat{\Pi}(-s_0) = \bar{\Pi}(-M_Z^2) - \bar{\Pi}(-s_0)$.

$\sqrt{s}$ interval (GeV)	$s_0 = 6$	$s_0 = 15$	$s_0 = 25$	$s_0 = 50$	$s_0 = 100$	$s_0 = 50^2$	$s_0 = M_Z^2$
$2m_\pi - 0.81$	23.40 ± 0.48	24.51 ± 0.50	24.82 ± 0.94	25.07 ± 0.51	25.19 ± 0.52	25.31 ± 0.52	25.31 ± 0.52
$0.81 - 1.46$	11.31 ± 0.50	12.49 ± 0.56	12.86 ± 0.14	13.14 ± 0.59	12.29 ± 0.60	13.44 ± 0.60	13.45 ± 0.60
$1.46 - 1.9$	5.90 ± 0.40 7.05 ± 0.72	7.27 ± 0.50 8.70 ± 0.89	7.76 ± 0.53 9.28 ± 0.95	8.17 ± 0.56 9.77 ± 1.00	8.39 ± 0.58 10.04 ± 1.03	8.61 ± 0.60 10.31 ± 1.06	8.62 ± 0.60 10.31 ± 1.06
$1.9 - 2.8$	6.95 ± 0.44 7.28 ± 0.44	9.70 ± 0.61 6.67 ± 0.16	10.85 ± 0.68 8.57 ± 0.21	11.93 ± 0.75 12.42 ± 0.75	12.55 ± 0.79 13.06 ± 0.79	13.22 ± 0.83 13.75 ± 0.83	13.24 ± 0.83 13.77 ± 0.83
$2.8 - 3.74$	3.53 ± 0.01	5.68 ± 0.02	6.80 ± 0.02	7.98 ± 0.03	8.74 ± 0.03	9.62 ± 0.03	9.65 ± 0.03
$3.74 - 5$	3.65 ± 0.09	6.67 ± 0.16	8.57 ± 0.21	10.92 ± 0.26	12.67 ± 0.30	14.98 ± 0.36	15.06 ± 0.36
$5 - \infty$	6.11 ± 0.02	13.36 ± 0.09	19.74 ± 0.12	31.38 ± 0.18	46.15 ± 0.25	134.69 ± 0.48	169.99 ± 0.52
ω, ϕ, ψ's, Υ's	10.60 ± 0.27	13.37 ± 0.38	14.72 ± 0.43	16.17 ± 0.49	17.18 ± 0.53	18.67 ± 0.57	18.73 ± 0.58
$\Delta\alpha_{\rm had}^{\rm data}(-s_0) \cdot 10^4$	71.45 ± 1.13 72.93 ± 1.41	93.05 ± 1.41 94.91 ± 1.70	106.12 ± 1.51 108.10 ± 1.81	124.76 ± 1.64 126.85 ± 1.92	144.16 ± 1.72 146.32 ± 2.00	238.54 ± 1.84 240.77 ± 2.10	274.05 ± 1.86 276.27 ± 2.12

Table 2.1: Explicit breakdown of contributions to $\Delta\alpha_{\rm had}^{(5)}(s = -s_0)$ in the spacelike region for $6 \leq s_0 \leq M_Z^2$ GeV^2. The same prescription for generating the data interpolation is used as was presented in Chapter 1 for the timelike evaluation of $\Delta\alpha_{\rm had}^{(5)}(M_Z^2)$, and again we show complimentary results through the energy intervals $1.46 \leq \sqrt{s} \leq 2.8$ and final sum, where the upper (lower) braced entry corresponding to the use of inclusive (exclusive) data. The perturbative contributions here were evaluated with all u, d, s, c and b flavours in their active domains, and five light quarks contributing internal loops at $\mathcal{O}(\alpha_s^2)$ and $\mathcal{O}(\alpha_s^3)$. The scale is taken as $\mu = 20$ GeV, the c pole mass as 1.4 GeV and the b pole mass as 4.7 GeV.

one and two loop functions in the case of heavy quarks were given explicitly in Eqn. (1.19) and Eqn. (1.21), and can be readily evaluated. For the case of the light quarks, their contribution to $\delta^{\rm QCD}(s_0)$ turns out to be simply proportional to the logarithmic ratio of the two spacelike scales:

$$\begin{aligned}\left[\Delta\alpha_{\rm had}(-M_Z^2) - \Delta\alpha_{\rm had}(-s_0)\right]^{\rm QCD,(0)} &= \frac{\alpha}{\pi}\log\frac{M_Z^2}{s_0},\\ \left[\Delta\alpha_{\rm had}(-M_Z^2) - \Delta\alpha_{\rm had}(-s_0)\right]^{\rm QCD,(1)} &= C_A\frac{3\alpha}{4\pi}\frac{\alpha_{\rm s}}{\pi}\log\frac{M_Z^2}{s_0}.\end{aligned}$$

For sample pole mass $m_c = 1.4$ GeV and scale $\mu = 20$ GeV, we obtain contributions to $\delta^{\rm QCD(0)}(s_0)\cdot 10^4$ and $\delta^{\rm QCD(1)}(s_0)\cdot 10^4$ set out in Table 2.2. Higher order terms will prove to be numerically significant. We detail their treatment, available to $\mathcal{O}(\alpha_{\rm s}^3)$, in the following sections.

2.2.3 Reconstruction of the $\mathcal{O}(\alpha_{\rm s}^2)$ threshold behaviour

Section 1.4 illustrated the treatment of the perturbative vacuum polarization function above threshold as a series in m_q^2/s. For the direct evaluation of $\Delta\alpha_{\rm had}(M_Z^2)$ this was sufficient to determine the R-ratio to the point where the broad higher ψ resonances faded into agreement with the continuum limit. However, since we are probing the charm mass, we categorically must have the appropriate behaviour of the QCD polarization function through the threshold $s \simeq 4m_c^2$, exactly at the point where the mass expansion outlined previously breaks down. Fortunately, there exist techniques that allow a complete reconstruction of the functional form of $\Pi^{(2)}$ through threshold to be made. As this behaviour is of paramount importance, we numerically reconstruct its precise form, maximally leveraging our knowledge of low and high energy expansions in the safe regions away from threshold by using *Padé approximants* [49, 50] through the dangerous interval $s \simeq 4m_q^2$. Both sets of expansions are mapped in such a way that their complete behaviour can be utilized where they are valid, away from threshold, for interpolation purposes. Of course, the light quark contribution requires no such sophisticated treatment, and can be obtained directly from the massless limits of the three loop polarization functions of Section 1.4.

In [17], low energy expansions, in terms of $1/z = s/4m_q^2$, were obtained for the chief contri-

butions to the $\mathcal{O}(\alpha_s^2)$ vacuum polarization functions, $\hat{\Pi}_A$, corresponding to the pseudo-Abelian pieces whose Feynman graphs contain no internal loops, $\hat{\Pi}_{NA}$, pertaining to strictly non-Abelian Feynman graphs, $\hat{\Pi}_l$, corresponding to graphs containing light quark loops radiated from an external massive quark, and $\hat{\Pi}_F$ describing the radiation of heavy quark loops from an external heavy quark loop. The expansions are valid sufficiently beneath threshold energies, and are determined to $\mathcal{O}([s/4m_q^2]^7)$, the full low energy vacuum polarization function can be approximated,

$$\hat{\Pi}^{(2)} = \sum_{n>0} \left[C_F^2 A_A^n + C_A C_F A_{NA}^n + C_F T n_l A_l^n + C_F T A_F^n \right] \left(\frac{1}{z}\right)^n,$$

where the $A_{A,NA,l,F}^n$ coefficients are pure numbers. Note these dominant contributions to the low energy expansion possess the same colour decomposition as the high energy case.

We choose to perform the interpolation in terms of components of the Adler D-function, which is closely related to the derivative of the vacuum polarization function, and is defined by

$$D(-s) = -12\pi^2 s \frac{d\Pi(s)}{ds}, \tag{2.6}$$

and so we recover the $\mathcal{O}(\alpha_s^2)$ contribution to $\delta^{\rm QCD}(s_0)$ by evaluating the integral

$$\left[\Delta\alpha_{\rm had}(-M_Z^2) - \Delta\alpha_{\rm had}(-s_0)\right]^{\rm QCD,(2)} = \left(\frac{\alpha_s}{\pi}\right)^2 \frac{\alpha}{3\pi} \int_{-s_0}^{-M_Z^2} ds' \frac{D^{(2)}(s')}{s'}. \tag{2.7}$$

After reexpressing the high and low energy series expansions for $\Pi^{(2)}$ as series for the $\mathcal{O}(\alpha_s^2)$ Adler D-function in terms of the variable z, we perform the mapping to the ω-plane [49],

$$\omega = \frac{1 - \sqrt{1-z}}{1 + \sqrt{1-z}}$$

which transforms the infinite half plane $-\infty < z \leq 0$ to the interior of $-1 < \omega \leq 0$. In this way we can utilize the *entire* global behaviour in the regions where we trust both series expansions to extract the Padé fit.

The Padé approximant itself is a rational function, the ratio of two polynomials,

$$\mathrm{P}_{[a/b]}(\omega) \equiv \frac{\sum_{i=0}^{a} \alpha_i \omega^i}{\sum_{i=0}^{b} \beta_i \omega^i}.$$

By fitting the approximant in the ω plane, where the convergent parts of the high and low energy expansions lie in the dominant portions of $-1 < \omega < 0$, and the divergent region is rather localized, we ensure that the functional form through threshold is an accurate reconstruction of

the underlying 'true' function. Typically an approximant of the form $P_{[4/4]}(\omega)$ or $P_{[3/3]}(\omega)$ is sufficient to interpolate the complete function in the ω-plane. The Padé approximant is then transformed back to the z-plane using the inverse mapping defined by

$$z = \frac{4\omega}{(1+\omega)^2}$$

and now describes the full behaviour of the $\mathcal{O}(\alpha_s^2)$ Adler-D function throughout the infinite half-plane $s < 0$. Sample results of the procedure are illustrated in Fig. 2.2, for the case of

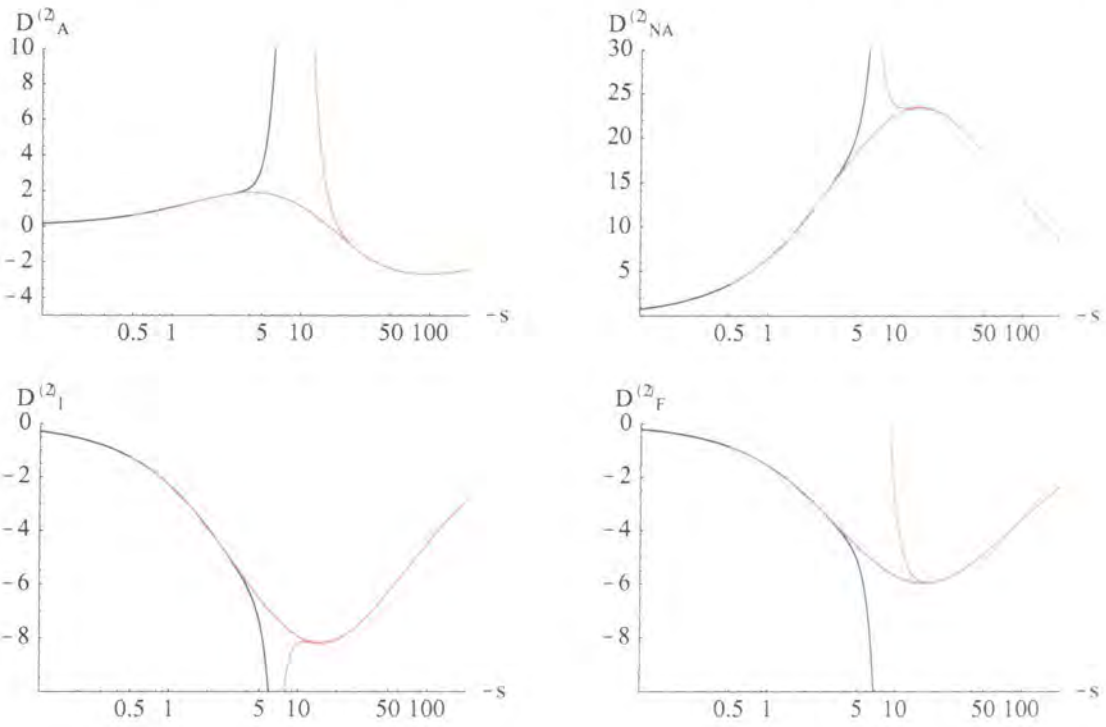

Figure 2.2: Figure illustrating the efficacy of the Padé interpolation technique through threshold for $\mu = 20$ GeV and a charm mass of 1.4 as a generic example. The $\mathcal{O}(\alpha_s^2)$ contribution to the Adler D-function is shown as high (red curve) and low (blue curve) energy expansions, for each of the colour factor components. The magenta line shows the Padé threshold interpolation, it becomes indistinguishable from the mass expansions away from threshold.

$m_c = 1.4$ GeV and the scale $\mu = 20$ GeV. It is apparent (at least visually) that the technique performs an excellent job of interpolating through threshold.

We can finally generate the $\mathcal{O}(\alpha_s^2)$ contribution to (2.7) by numerically integrating the Padé

approximant in the s-plane according to Eqn. (2.7). We present the results of this technique for the sample parameter set, $m_c = 1.4$ GeV, $\mu = 20$ GeV in Table 2.2. Comparing the light and charm contributions, we see that the mass effects are rather significant, and that the complete $\mathcal{O}(\alpha_s^2)$ mass dependence is important.

2.2.4 Determination of the $\mathcal{O}(\alpha_s^3)$ massless contribution

Only the massless absorptive piece of the $\mathcal{O}(\alpha_s^3)$ vacuum polarization function has been calculated, and the results were presented for $R^{(3)}$ in Section 1.4. Nevertheless this is sufficient information to reconstruct the massless approximation to the $\mathcal{O}(\alpha_s^3)$ contribution to $\delta^{\rm QCD}(s_0)$ through the use of the stalwart dispersion integral (2.1), and the absorptive piece of the $\mathcal{O}(\alpha_s^3)$ vacuum polarization. Since $R^{(3)} = \sum_{i=0}^{2} A^{(i)}(n_f) \log^i(s/\mu^2)$, from Eqn. (1.22), this is a well defined quantity,

$$\left[\Delta\alpha_{\rm had}(M_Z^2) - \Delta\alpha_{\rm had}(-s_0)\right]^{\rm QCD,(3)} = \frac{\alpha}{3\pi}\left(\frac{\alpha_s}{\pi}\right)^3 (M_Z^2 - s_0) \int_0^\infty ds' \frac{R^{(3)}(s')}{(s+M_Z^2)(s+s_0)}$$

$$= \left(\frac{\alpha_s}{\pi}\right)^3 \frac{\alpha}{3\pi}(M_Z^2 - s_0)\left\{A^{(0)} \log\frac{M_Z^2}{s_0} + \frac{A^{(1)}}{2}\left(\log^2\frac{M_Z^2 2}{\mu^2} - \log^2\frac{s_0}{\mu^2}\right) + \frac{A^{(2)}}{3}\left(\pi^2 \log\frac{M_Z^2}{s_0} + \log^3\frac{M_Z^2}{\mu^2} - \log^3\frac{s_0}{\mu^2}\right)\right\}.$$

Substituting the appropriate flavour dependent coefficients, we generate massless contributions at four loop level to $\delta^{\rm QCD,(3)}(s_0) \cdot 10^4$ written in Table 2.2. Clearly this treatment of the four loop vacuum polarization function with a massless charm is not entirely satisfactory, we saw for the three loop contribution that the mass effects can be rather significant at low s_0. However, the mass expansions are not in place to allow an analagous Padé treatment at this order - the most we can do is to estimate the uncertainty arising from an imperfect description of the charm in $\delta^{\rm QCD,(3)}(s_0)$.

2.3 Evaluation of the pole mass of the charm quark

The complete set of QCD contributions to $\mathcal{O}(\alpha_s^3)$ to $d(s_0)$ is set out in Table 2.2. With the four loop contribution to vaccum polarization calculated, we now have sufficient information to

Contribution	Flavour	$s_0 = 6$ GeV^2	15	25	50	100	50^2
$\mathcal{O}(1)$	u, d, s	112.02	97.83	89.92	79.19	68.46	18.61
$\mathcal{O}(\alpha_s)$		5.53	4.83	4.44	3.91	3.38	0.92
$\mathcal{O}(\alpha_s^2)$		0.69	0.39	0.25	0.10	-0.03	-0.15
$\mathcal{O}(\alpha_s^3)$		0.38	0.22	0.15	0.08	0.04	0.01
$\mathcal{O}(1)$	c	64.17	59.62	56.20	50.72	44.54	12.37
$\mathcal{O}(\alpha_s)$		5.20	4.41	3.92	3.27	2.67	0.64
$\mathcal{O}(\alpha_s^2)$		1.62	1.08	0.78	0.44	0.18	-0.10
$\mathcal{O}(\alpha_s^3)$		0.26	0.14	0.10	0.06	0.03	0.01
$\delta^{\rm QCD}(s_0) \cdot 10^4$	u, d, s, c	189.87	168.53	155.76	137.76	119.28	32.31

Table 2.2: Perturbative contributions to $\delta^{\rm QCD}(s_0) \equiv [\Delta\alpha_{\rm had}(-M_Z^2) - \Delta\alpha_{\rm had}(s_0)]^{\rm QCD}$ to $\mathcal{O}(\alpha_s^3)$ from the u, d, s and c flavours, determined using the prescription of the earlier sections. Note that the QCD contributions in the earlier Table 2.1 also includes the b quark.

evaluate $d(s_0)$, for a spectrum of charm mass parameters. By studying how $d(s_0)$ varies as a function of both the charm mass and s_0 we will be able to extract information regarding the most appropriate (consistent) value of m_c to take. The values of the residual function $d(s_0)$ that we obtain for $\mu = 20$ GeV and for the charm mass parameter varied between $1.26 \leq m_c \leq 1.46$ GeV in increments of 0.02 GeV are written in Table 2.3, using the inclusive (exclusive) data. It transpires that our sample parameter ($m_c = 1.40$ GeV) set is rather good - there is a fairly minimal deviation from zero for all values of s_0, although this residual grows quite quickly with comparatively small changes in the charm mass from its preferred value.

If we assume that the residual is the product of a deficiency in either the formalism or the data interpolation, we can gain further insight by assuming the discrepancy $d(s_0)$ arises from some localized region, $s \simeq s_p$, and then approximate its supplemental contribution to the R-ratio input to the dispersion integral (2.1) by a simple pole,

$$R^{\rm pole}(s) \equiv \delta(s - s_p) R_p.$$

The set of remainders may then be modelled by the function

$$d(s_0) \equiv \Delta\alpha_{\rm pole}(-M_Z^2) - \Delta\alpha_{\rm pole}(-s_0) = \frac{\alpha R_p}{3\pi} \frac{(M_Z^2 - s_0)}{(s_p + M_Z^2)(s_p + s_0)} \simeq \frac{\alpha R_p}{3\pi} \frac{1}{s_p + s_0} \qquad (2.8)$$

and by fitting the model parameters to the evaluations of $d(s_0)$ we garner some idea of the location in s of the model deficiency. Given the uncertainty engendered from the QCD charm

m_c(GeV)	$d(s_0 = 6\ \text{GeV}^2) \cdot 10^4$	$d(15) \cdot 10^4$	$d(25) \cdot 10^4$	$d(50) \cdot 10^4$	$d(100) \cdot 10^4$	$d(50^2) \cdot 10^4$
1.46	0.57 (1.31)	0.36 (0.72)	0.23 (0.47)	0.10 (0.23)	0.04 (0.10)	−0.02 (−0.03)
1.44	0.39 (1.13)	0.24 (0.60)	0.16 (0.40)	0.06 (0.19)	0.03 (0.09)	−0.02 (−0.03)
1.42	0.20 (0.93)	0.12 (0.48)	0.07 (0.31)	0.02 (0.15)	0.00 (0.06)	−0.02 (−0.03)
1.40	0.00 (0.75)	0.01 (0.37)	0.00 (0.24)	−0.03 (0.10)	−0.03 (0.03)	−0.02 (−0.02)
1.38	−0.17 (0.57)	−0.09 (0.27)	−0.08 (0.16)	−0.07 (0.06)	−0.04 (0.02)	−0.02 (−0.03)
1.36	−0.37 (0.37)	−0.21 (0.15)	−0.16 (0.08)	−0.11 (0.02)	−0.06 (−0.01)	−0.02 (−0.03)
1.34	−0.57 (0.17)	−0.33 (0.03)	−0.24 (−0.00)	−0.16 (−0.03)	−0.09 (−0.03)	−0.03 (−0.04)
1.32	−0.74 (−0.01)	−0.43 (−0.07)	−0.31 (−0.07)	−0.19 (−0.06)	−0.11 (−0.05)	−0.02 (−0.03)
1.30	−0.94 (−0.20)	−0.54 (−0.18)	−0.39 (−0.15)	−0.25 (−0.12)	−0.14 (−0.08)	−0.03 (−0.04)
1.28	−1.11 (−0.38)	−0.64 (−0.28)	−0.45 (−0.21)	−0.28 (−0.15)	−0.15 (−0.09)	−0.02 (−0.03)
1.26	−1.32 (−0.58)	−0.76 (−0.40)	−0.53 (−0.29)	−0.32 (−0.19)	−0.18 (−0.12)	−0.03 (−0.04)

Table 2.3: Table containing the residual $d(s_0) \equiv \delta^{\text{data}}(s_0) - \delta^{\text{QCD}}(s_0)$ for a spectrum of charm pole masses and the lower QCD scale $\mu = 20$ GeV. The entries (bracketed) correspond to the use of the inclusive (exclusive) data interpolations in the dispersion integral.

threshold, we hope to see some stable value of $s_p \simeq 4m_c^2$, and that the most appropriate charm mass will have $R_p \simeq 0$. We show the residual points, and the results of their fit to the simple pole model Eqn. (2.8) in Fig. 2.3. The parameters describing the complete set of fits to the model for inclusive and exclusive data at both scales of $\mu = 20$ and $\mu = 50$ and the full spectrum of charm masses are given in Table 2.4.

The fitting procedure proves to be instructive - for the favoured scale and inclusive data, we obtain a persistent residual pole in our model at $s \sim 7$ GeV, which corresponds neatly with the interval within which we anticipate deficiencies in the charm description will lie. The residual is nullified by taking a charm pole mass of between 1.40 and 1.42 GeV, the individual pole fits here correspond to a sign switch in the monotonic (for timelike s_p) modelling function, see Fig. 2.3. Moreover, if we now look at the exclusive data for these values of m_c, having nullified the dominant contribution to the residual structure from the charm region, we see a surplus in the low energy ambiguous interval where the inclusive and exclusive data appear to possess distinct normalizations. In fact, the pole model acts to correct the exclusive data here towards the inclusive interpolation, we take this as further circumstantial evidence favouring the inclusive data interpolation over the exclusive channel summation. The instability of the exclusive values of s_p might be ascribed to the fitting of a simple single pole model to a quantity that in fact

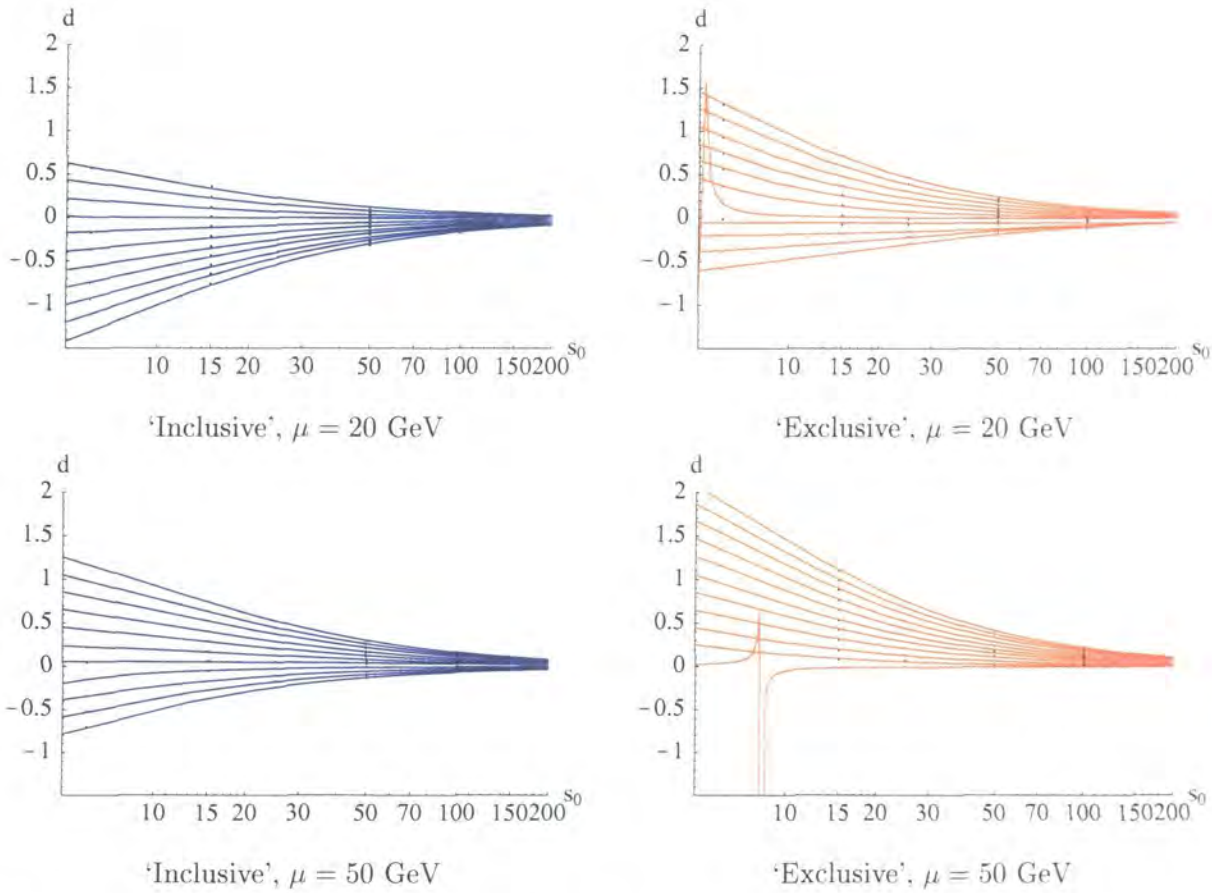

'Inclusive', $\mu = 20$ GeV

'Exclusive', $\mu = 20$ GeV

'Inclusive', $\mu = 50$ GeV

'Exclusive', $\mu = 50$ GeV

Figure 2.3: Spectra of charm mass plots, solid lines from top to bottom, $m_c = 1.46$ to 1.26 GeV, in decrements of 0.02 GeV, illustrating the residual function $d(s_0)$ at scales $\mu = 20$ GeV and $\mu = 50$ GeV.

requires two poles, one to account for the charm variation, and a second to compensate for potential overcounting implicit in the exclusive channels.

Interpretation of the fits to the higher scale residuals is not entirely as clear cut. Taking the sign switch as indicative of the position of the best charm pole mass we find values of m_c of between 1.32 and 1.34 GeV and 1.26 and 1.28 GeV for the inclusive and exclusive low energy data parameterizations respectively. This quantifies the extent to which our value of the charm mass is dependent on the QCD scale used. We list in Table 2.5 three values of charm pole mass, the Particle Data Group [6] world value as 'control' and those values obtained from the current analysis, using the $\mu = 20$ GeV determination as central value and its variation with scale to

m_c(GeV)	'Inclusive' $\mu = 20$ GeV	'Exclusive' $\mu = 20$ GeV	'Inclusive' $\mu = 50$ GeV	'Exclusive' $\mu = 50$ GeV
1.46	(0.9, 6.4)	(1.8, 4.4)	(2.3, 9.4)	(3.1, 6.6)
1.44	(0.6, 5.8)	(1.5, 3.9)	(2.0, 10.0)	(2.8, 6.6)
1.42	(0.3, 4.5)	(1.1, 3.3)	(1.7, 10.7)	(2.5, 6.5)
1.40	(0.0, −4.6)	(0.8, 2.4)	(1.3, 10.8)	(2.1, 6.1)
1.38	(−0.4, 14.4)	(0.5, 1.3)	(1.0, 12.3)	(1.8, 5.8)
1.36	(−0.7, 9.8)	(0.3, −0.8)	(0.7, 17.8)	(1.4, 5.6)
1.34	(−1.1, 8.9)	(−0.0, −5.1)	(0.85, 117.3)	(1.1, 5.3)
1.32	(−1.3, 7.7)	(**, **)	(−0.1, −1.8)	(0.8, 4.6)
1.30	(−1.7, 8.0)	(−1.6, 57.5)	(−0.4, 2.9)	(0.5, 2.9)
1.28	(−1.9, 7.2)	(−1.3, 21.0)	(−0.7, 3.8)	(0.2, 0.8)
1.26	(−2.2, 7.1)	(−1.5, 14.7)	(−0.9, 4.0)	(−0.0, −8.3)

Table 2.4: Table of parameters as (R_p, s_p) pairs describing the simple pole fits, Eqn. (2.8) to the residual function $d(s_0)$ for the spectrum of charm masses, and scale variations described in Section 2.2, and illustrated in Fig. 2.3. The entry denoted by $(**, **)$ corresponds to a residual sufficiently close to 0 for all s_0 to render the fitting procedure inappropriate.

$\mu = 50$ GeV to generate a (conservative) estimate of the intrinsic error. It is clear that the

Source	m_c
'Inclusive'	1.40(1.34) GeV
'Exclusive'	1.34(1.26) GeV
PDG	1.46 ± 0.11 GeV

Table 2.5: The pole mass of the charm quark determined from requiring consistency of the space-like evaluation of the dispersion relation using first inclusive, then exclusive data for R in the region $1.46 \leq \sqrt{s} \leq 1.9$ GeV. The first value corresponds to the choice of QCD scale $\mu = 20$ GeV, and the number in brackets corresponds to scale choice $\mu = 50$ GeV. For comparison we show the values of the pole mass corresponding to the Particle Data group range of 1.15 to 1.35 GeV for the running mass in the $\overline{\text{MS}}$ scheme.

exclusive data systematically favour a charm pole mass that is rather too low when compared with the accepted range extracted from the global data.

Chapter 3

Summary and conclusions for $\alpha(M_Z^2)$

The first half of this thesis addressed the vacuum polarization phenomenon in quantum electrodynamics. We began with a review of the concepts and the formalism involved, illustrating why quantum field theory requires the electromagnetic coupling, α, to run with the energy of interaction, from the familiar long wavelength Thomson limit of 1/137.036 to $\sim$ 1/129 at the Z-boson mass.

The electroweak sector of the standard model can be fully defined by the choice of three empirically extracted parameters, conventially chosen as G_F, M_Z and our $\alpha(M_Z^2)$, where the latter of the trio is the least well determined. Obviously as exact an estimate as possible for the running of the QED coupling proves a crucial quantity, necessary as input thoughout precision phenomenological tests of the Glashow-Weinberg-Salam model. The running of the coupling is parameterized by the quantity $\Delta\alpha(s)$, which naturally decomposes into contributions arising from leptonic and hadronic physics, where the latter is further subdivided into contributions from the five lightest quark flavours, and the top quark.

We then sketched the derivation of the well known one loop, $\mathcal{O}(\alpha)$, leptonic contribution to vacuum polarization and presented the potentially significant two loop leptonic supplement.

After the 'clean' perturbative calculation of the leptonic piece, we examined the hadronic component of the vacuum polarization, in principle described by QCD. Strong low energy effects

do not permit a direct theoretical evaluation of the complete hadronic contribution, and as a means to circumvent this obstacle, we introduced two deep rooted corollaries to scattering theory, the optical theorem and dispersion relations, which together allow us to substitute for theory empirical measurements of the total hadronic cross-section in e^+e^- annihilation.

A reappraisal of the hadronic contribution to $\Delta\alpha(s)$ is motivated by substantial progress in two parallel fields. The first of these are theoretical advances in perturbative calculations of the total hadronic cross-section in e^+e^- annihilation, where complete mass dependent expressions are now available to $\mathcal{O}(\alpha_s)$, the $\mathcal{O}(\alpha_s^2)$ series is known as a mass expansion sufficiently well to ensure its applicability close to the quark flavour thresholds, and the massless contributions at $\mathcal{O}(\alpha_s^3)$ are also determined. The stability of the perturbative prediction allows us to supplant comparatively poor data in the continuum regions between flavour thresholds, and obtain a set of more realistic contributions from these intervals with far smaller associated errors.

The second motivation for the update is the availability of a range of substantially improved measurements of hadronic cross-sections in the low energy domain, $\sqrt{s} \lesssim 5$ GeV.

From threshold for pion production to $\sqrt{s} \simeq 1.5$ GeV the cross-section can be constructed by a summation of all the accessible e^+e^- annihilation channels. A series of experiments by the CND and SND collaborations at the VEPP-2M facility in Novosibirsk have refined the measurements of the dominant contributing cross-sections $\sigma_{\pi^+\pi^-}$, $\sigma_{2\pi^0\pi^+\pi^-}$ and $\sigma_{2\pi^+2\pi^-}$ to dramatic effect - the errors arising from these contributions can be said to be well under control.

Above $\sqrt{s} \simeq 1.5$ GeV, fully inclusive measurements of the cross-section are available, indiscriminately collecting all hadronic final states. We are able to construct an interpolation of the cross-section by using purely inclusive data, and significant new information has recently arrived in the form of a comprehensive scan of the total hadronic cross-section for $2 \lesssim \sqrt{s} \lesssim 5$ GeV by the BES-II collaboration in Beijing. These new data *considerably* better resolve the interpolation in the region, the previously existing data being comparatively sparse and plagued by large uncertainties.

In the overlapping region we found that the complimentary determinations of R through the energy interval $1.4 \lesssim \sqrt{s} \lesssim 2$ GeV exhibit incongruous normalizations, although similar

structure, which lead us to distinct predictions of $\Delta\alpha^{(5)}_{\rm had}(s)$. We were unable to categorically determine which of the two evaluations more accurately reflects the true cross-section in the region, although implicitly favour the inclusive parameterization on continuity grounds compared with the precise Beijing data which show excellent agreement with perturbative QCD in the light quark continuum. The subjective choice of data in this region corresponds to a shift in the final value of $\Delta\alpha^{(5)}_{\rm had}(M_Z^2)$ of some 2.2 units, a figure comparable with the full error from all other sources. A resolution of this ambiguity is clearly of some importance.

The final energy interval requiring significant data input is the physical charm threshold, $3.74 \leq \sqrt{s} \leq 5$ GeV. Here broad members of the ψ resonance family overlap to the extent that they preclude parameterization with a Breit-Wigner model. Moreover, the data, with the exception of the BES-II measurements exhibit substantial systematic normalization uncertainties. We implement a rescaling procedure for these data by fixing their normalizations to the perturbative continua straddling the charm threshold. This allows the structure in the region to be well resolved, and again significantly reduces the error contribution.

By summing the full set of contributions, we obtain values of $\Delta\alpha^{(5)}_{\rm had}(M_Z^2)$ which we compare with the benchmark value of Eidelman and Jegerlehner in an explicit decomposition of the various contributions.

Origin	$\Delta\alpha^{(5)}_{\rm had}(M_Z^2)\cdot 10^4$	$\alpha^{-1}(M_Z^2)$
'Inclusive'	274.26 ± 1.90	128.972 ± 0.026
'Exclusive'	276.49 ± 2.14	128.941 ± 0.029
Eidelman, Jegerlehner	280.37 ± 6.54	128.896 ± 0.090

We briefly review the Standard Model Higgs mechanism, and present the results of a global fit of electroweak data to radiative corrections, performed by the Electroweak Working Group. A preferred value of the Higgs mass is found at 110 GeV, marginally above the energies currently excluded by direct searches at LEP2.

In the second part of this investigation into the physics of vacuum polarization, motivated by the potential to further constrain the error on $\Delta\alpha^{(5)}_{\rm had}(M_Z^2)$, we perform an analytic continuation of the polarization function, $\hat{\Pi}$ into the spacelike region, $s < 0$, around the large semicircle

$|s| = M_Z^2$, and then along the real axis to $-s_0 > -M_Z^2$ through Eqn. 2.3,

$$\Delta\alpha_{\rm had}(-M_Z^2) = \left[\Delta\alpha_{\rm had}(-M_Z^2) - \Delta\alpha_{\rm had}(-s_0)\right]^{\rm QCD} + \Delta\alpha_{\rm had}^{\rm data}(-s_0).$$

We show that the continuations effectively replace the data contributions by perturbative QCD calculations, evaluated in the spacelike domain well away from bound state and low energy effects. We illustrate, by reference to the susceptibility of the $\mathcal{O}(1)$ charm contribution to the precise value of the charm pole mass parameter, that this continuation technique cannot supplant the error from the direct evaluation. It transpires that the charm threshold interval is better constrained by the data than the QCD contribution with the current uncertainties associated with the charm mass.

We therefore shift the direction of our approach from that of refining the resolution of the hadronic contribution to vacuum polarization to performing a redetermination of the charm pole mass, using complementary data evaluations from dispersion integrals analagous to Chapter 1 to fix the QCD charm threshold.

A function $d(s_0) \equiv \delta^{\rm data}(s_0) - \delta^{\rm QCD}(s_0)$ was defined which quantifies the discrepancy between direct and continued evaluations of the $\Delta\alpha_{\rm had}^{(5)}(M_Z^2)$. A consistent description would require $d(s_0) = 0$ for all s_0. The variation of d with charm mass and QCD scale then yields information about the consistent choices of defining parameters. By modelling the residue $d(s_0)$ with a simple pole we have been able to extract the magnitude of the charm pole mass, and performing parallel calculations again for the inclusive and exclusive measurements in the overlapping energy regions at low $\sqrt{s}$ we have justifed a preference for the inclusive data in the energy interval $1.5 \lesssim \sqrt{s} \lesssim 2$ GeV We show again values of m_c determined in this way with the Particle Data Group world average below.

Source	m_c
'Inclusive'	1.40(1.34) GeV
'Exclusive'	1.34(1.26) GeV
PDG	1.46 ± 0.11 GeV

The stability of the fits using inclusive data at the preferred scale would seem to favour the use of the inclusive data in the ambiguous energy interval.

Future advance in the physics of vacuum polarization might be obtained in one of variety of ways. Firstly, a clearer experimental determination of the low energy regions would seem to be a prerequisite. The Beijing data have elucidated the use of the inclusive data, but do not probe to sufficiently low enough energies to test the domain of overlapping inclusive and exclusive measurements, and the exclusive channels need better defining in order to resolve their apparent overestimation. For the evaluation of the charm mass, the $\mathcal{O}(\alpha_s^3)$ mass dependence would be useful to quantify. By reference to the $\mathcal{O}(\alpha_s^2)$ contribution, we see that mass effects can be significant, and speculate that they may be of the order of the size of increment used in the evaluations of d to specify m_c.

Finally, better (independent) evaluation of the charm pole mass would permit the analytic continuation techniques to reduce the error in $\Delta\alpha_{\rm had}^{(5)}(M_Z^2)$, or alternatively, a direct and accurate measurement of the Higgs mass would allow the analysis to operate in reverse - more rigidly constraining the $\Delta\alpha_{\rm had}^{(5)}(M_Z^2)$ and the physics therein.

References

[1] F. Halzen and A. D. Martin, Quarks And Leptons, *New York, USA: Wiley (1984) 396p.*

[2] M. E. Peskin and D. V. Schroeder, An Introduction to quantum field theory, *Reading, USA: Addison-Wesley (1995) 842 p*

[3] S. L. Glashow, Nucl. Phys. **B22** (1961) 579;
A. Salam, Elementary Particle Theory ed. N. Svartholm, Almquist and Forlag, Stockholm (1968);
S. Weinberg, Phys. Rev. Lett. **19** (1967) 1264.

[4] W. J. Marciano and A. Sirlin, Phys. Rev. Lett. **61** (1988) 1815;
T. van Ritbergen and R. G. Stuart, Nucl. Phys. **B564** (2000) 343.

[5] R. Assmann *et al.*, Eur. Phys. J. **C6** (1999) 187.

[6] D. E. Groom *et al.*, Eur. Phys. J. **C15** (2000) 1.

[7] A. D. Martin and D. Zeppenfeld, Phys. Lett. **B345** (1995) 558.

[8] S. Eidelman and F. Jegerlehner, Z. Phys. **C67**, 585 (1995).

[9] J. H. Kuhn and M. Steinhauser, Phys. Lett. **B437**, 425 (1998).

[10] M. Davier and A. Hocker, Phys. Lett. **B435**, 427 (1998).

[11] I. S. Gradshteyn and I. M. Ryzhik, Tables of Integrals, Series and Products, 5th edition. *London, UK: Academic Press (1981) 1160p.*

[12] G. Källén and A. Sabry, *K. Dan. Vidensk. Selsk. Mat.-Fys. Medd* **29** (1955) No. 17.

[13] N. Cabibbo and R. Gatto, Phys. Rev. **124**, 1577 (1961).

[14] F. A. Berends and G. J. Komen, Phys. Lett. **B63**, 432 (1976);
E. A. Paschos, Nucl. Phys. **B159**, 285 (1979);
J. Ellis, M. K. Gaillard, D. V. Nanopoulos and S. Rudaz, Nucl. Phys. **B176**, 61 (1980);
W. Wetzel, Z. Phys. **C11**, 117 (1981).

[15] W. A. Bardeen, A. J. Buras, D. W. Duke and T. Muta, Phys. Rev. **D18** (1978) 3998.

[16] B. A. Kniehl, Nucl. Phys. **B347** (1990) 86;
D. J. Broadhurst, J. Fleischer and O. V. Tarasov, Z. Phys. **C60** (1993) 287.

[17] K. G. Chetyrkin, J. H. Kuhn and M. Steinhauser, Nucl. Phys. **B482** (1996) 213.

[18] K. G. Chetyrkin, R. Harlander, J. H. Kuhn and M. Steinhauser, Nucl. Phys. **B503** (1997) 339.

[19] S. G. Gorishnii, A. L. Kataev and S. A. Larin, Phys. Lett. **B259**, 144 (1991);
L. R. Surguladze and M. A. Samuel, Phys. Rev. Lett. **66**, 560 (1991).

[20] K. G. Chetyrkin, J. H. Kuhn and A. Kwiatkowski, Phys. Rept. **277** (1996) 189.

[21] K. G. Chetyrkin, Phys. Lett. **B307** (1993) 169.

[22] H. Guangshun, Private communication;
J. Z. Bai *et al.* [BES Collaboration], Phys. Rev. Lett. **84**, 594 (2000).

[23] Z. Jakubowski *et al.* [Crystal Ball Collaboration], Z. Phys. **C40**, 49 (1988).

[24] J. Siegrist *et al.* [MARK I Collaboration], Phys. Rev. **D26**, 969 (1982).

[25] R. Brandelik *et al.* [DASP Collaboration], Phys. Lett. **B76**, 361 (1978);
H. Albrecht *et al.* [DASP Collaboration], Phys. Lett. **B116**, 383 (1982).

[26] J. Burmester *et al.* [PLUTO Collaboration], Phys. Lett. **B66**, 395 (1977);
C. Berger *et al.* [PLUTO Collaboration], Phys. Lett. **B81**, 410 (1979);
L. Criegee and G. Knies [PLUTO Collaboration], Phys. Rept. **C83** (1982) 151.

[27] C. Bacci *et al.* [$\gamma\gamma 2$ Collaboration], Phys. Lett. **B86**, 234 (1979);
B. Esposito *et al.* [MEA Collaboration], Lett. Nuovo Cim. **28**, 337 (1980);
H. J. Behrend *et al.* [CELLO Collaboration], Phys. Lett. **B183**, 400 (1987);
W. Bartel *et al.* [JADE Collaboration], Phys. Lett. **B129**, 145 (1983);
B. Niczyporuk *et al.* [LENA Collaboration], Z. Phys. **C15**, 299 (1982);
A. E. Blinov *et al.* [MD1 Collaboration], Z. Phys. **C49**, 239 (1991);
A. E. Blinov *et al.* [MD1 Collaboration], Z. Phys. **C70**, 31 (1996);
B. Adeva *et al.* [Mark-J Collaboration], Phys. Rev. Lett. **50**, 799 (1983);
B. Adeva *et al.* [Mark-J Collaboration], Phys. Rev. Lett. **50**, 2051 (1983);
B. Adeva *et al.* [Mark-J Collaboration], Phys. Rept. **109**, 131 (1984);
B. Adeva *et al.* [Mark-J Collaboration], Phys. Rev. **D34**, 681 (1986);
R. Brandelik *et al.* [TASSO Collaboration], Phys. Lett. **B113**, 499 (1982);
M. Althoff *et al.* [TASSO Collaboration], Phys. Lett. **B138**, 441 (1984).

[28] R. Alemany, M. Davier and A. Hocker, Eur. Phys. J. **C2**, 123 (1998).

[29] D. Buskulic *et al.* [ALEPH Collaboration], Z. Phys. **C70**, 579 (1996);
L. M. Barkov *et al.* [OLYA, CMD Collaboration], Nucl. Phys. **B256**, 365 (1985);
I. B. Vasserman, *et al.* [OLYA Collaboration], Yad. Fiz. **30** (1979) 999;
I. B. Vasserman *et al.* [TOF Collaboration], Yad. Fiz. **33** (1981) 709;
S. R. Amendolia *et al.* [NA7 Collaboration], Phys. Lett. **B138**, 454 (1984);
A. Quenzer *et al.* [DM1 Collaboration], Phys. Lett. **B76**, 512 (1978);
D. Bisello *et al.* [DM2 Collaboration], Phys. Lett. **B220**, 321 (1989).

[30] R. R. Akhmetshin *et al.* [CMD-2 Collaboration], `hep-ex/9904027`.

[31] J. Gasser and U. G. Meissner, Nucl. Phys. **B357**, 90 (1991).

[32] S. R. Amendolia *et al.* [NA7 Collaboration], Nucl. Phys. **B277**, 168 (1986).

[33] G. Colangelo, M. Finkemeier and R. Urech, Phys. Rev. **D54** (1996) 4403.

[34] R. R. Akhmetshin *et al.* [CMD2 Collaboration], Phys. Lett. **B466** (1999) 392.

[35] M. N. Achasov *et al.* [SND Collaboration], `hep-ex/9809013`.

[36] M. N. Achasov *et al.* [SND Collaboration], Nucl. Phys. **A675**, 391 (2000).

[37] M. N. Achasov *et al.* [SND Collaboration], Phys. Lett. **B462**, 365 (1999).

[38] S. I. Dolinsky *et al.* [ND Collaboration], Phys. Rept. **202**, 99 (1991);
G. Cosme *et al.* [M2N Collaboration], Phys. Lett. **B63**, 349 (1976);
G. Parrour *et al.* [M2N Collaboration], Phys. Lett. **B63**, 357 (1976);
G. Cosme *et al.* [M3N Collaboration], Nucl. Phys. **B152**, 215 (1979);
A. Cordier *et al.* [DM1 Collaboration], Nucl. Phys. **B172**, 13 (1980);
A. Antonelli *et al.* [DM2 Collaboration], Z. Phys. **C56**, 15 (1992);
L. M. Kurdadze *et al.* [OLYA Collaboration], JETP Lett. **43**, 643 (1986);
D. Bisello *et al.* [DM2 Collaboration], Nucl. Phys. Proc. Suppl. **21**, 111 (1991);
B. Esposito *et al.* [MEA Collaboration], Lett. Nuovo Cim. **28**, 195 (1980);
L. M. Barkov *et al.* [CMD Collaboration], Sov. J. Nucl. Phys. **47**, 248 (1988);
A. Cordier *et al.* [DM1 Collaboration], Phys. Lett. **B81**, 389 (1979);
A. Antonelli *et al.* [DM2 Collaboration], Phys. Lett. **B212**, 133 (1988);
D. Bisello, *et al.* [DM1 Collaboration], Phys. Lett. **B107**, 145 (1981);
P. M. Ivanov *et al.* [OLYA Collaboration], Phys. Lett. **B107**, 297 (1981);
P. m. Ivanov *et al.* [OLYA Collaboration], JETP Lett. **36**, 112 (1982);
D. Bisello *et al.* [DM2 Collaboration], Z. Phys. **C39**, 13 (1988);
A. Cordier, *et al.* [DM1 Collaboration], Phys. Lett. **B110**, 335 (1982);
F. Mané, *et al.* [DM1 Collaboration], Phys. Lett. **B112**, 178 (1982).

[39] D. Buskulic *et al.* [ALEPH Collaboration], CERN PPE/97-013 (1997).

[40] R. Marshall, Z. Phys. **C43** (1989) 595.

[41] V. M. Aulchenko *et al.*, Phys. Lett. **B186** (1987) 432;
F. M. Renard, Nucl. Phys. **B82**, 1 (1974);
N. N. Achasov, *et al.* Sov. J. Nucl. Phys. **23**, 320 (1976);
N. N. Achasov, *et al.* Sov. J. Nucl. Phys. **54**, 664 (1991).

[42] F. Jegerlehner, Proc. IV Int. Symp. on Rad. Corr., Barcelona 1998, `hep-ph/9901386`.

[43] P. W. Higgs, Phys. Lett. **12** (1964) 132; *ibid.* Phys. Rev. Lett. **13** (1964) 508; *ibid.* Phys. Rev. **145** (1966) 1156;

[44] M. Veltman, Acta Phys. Polon. **B8** (1977) 475.

[45] LEP and SLD Electroweak Working Group, CERN EP/2000-16.

[46] M. Grünewald, Private communication;
LEP and SLD Electroweak Working Group, presented in the plenary talk by A. Gurtu at ICHEP 2000, Osaka, 27 July-2 Aug., 2000.

[47] R. Barate *et al.* [ALEPH Collaboration], `hep-ex/0011045`.

[48] S. Groote, J. G. Korner, K. Schilcher and N. F. Nasrallah, Phys. Lett. **B440** (1998) 375.

[49] J. Fleischer and O. V. Tarasov, Z. Phys. **C64** (1994) 413.

[50] S. Eidelman, F. Jegerlehner, A. L. Kataev and O. Veretin, Phys. Lett. **B454** (1999) 369.

Chapter 4

Precepts of deep inelastic scattering

In this chapter we present a principle test of perturbative QCD, that of the deeply inelastic scattering of a lepton from a proton target. We formulate the standard theoretical description of the basic DIS process, and illustrate how a comparison of measurements of cross-sections with theoretical treatments of varying degrees of sophistication can tell us about the composition of the hadronic target. This will lead us naturally to the concept of parton distributions and the dynamics of their evolution in distinct kinematic domains. We introduce the DGLAP evolution equations and illustrate how these can be viewed as a formalism for resumming large logarithms of the kinematic variables which arise in a perturbative computation.

4.1 The fundamental DIS process

Deep inelastic scattering was one of the first and classic experimental validations of perturbative QCD, and one that still provides a powerful microscopic window in examining the levels of sub-structure within a hadronic target[1]. The fundamental process can be symbolically represented by the expression

$$l + P \to l' + X,$$

[1]Further reviews of deep inelastic lepton-proton scattering can be found in refs. [1, 2, 3, 4]

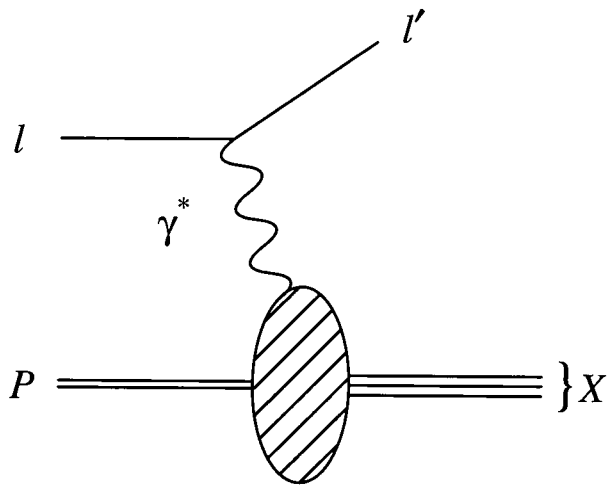

Figure 4.1: Schematic of a neutral current deep inelastic scattering of a lepton on a proton target, mediated via a highly virtual photon, γ^*. The incoming and scattered leptonic four-momenta are denoted by k and k' respectively, the incoming proton four-momentum by p, and X represents the hadronic final state after the inelastic collision.

wherein one collides a high energy lepton(l) with four-momentum k, inelastically from a proton(P) target carrying a four-momentum p. The incoming lepton emits a highly virtual gauge boson, either a photon or a Z^0 in the instance of a *neutral current* interaction, or an electrically charged $W^{\pm}$ for a *charged current* interaction[2]. In the reactions considered within the remit of this thesis, we restrict ourselves to neutral current interactions by requiring a charged lepton in the initial and final state. The electromagnetic current, mediated by the probing gauge boson, then interacts destructively with the proton, leaving the scattered lepton(l') and a complex hadronic final state(X), typically consisting of one or more hadronic jets, along with the fragmented proton remnants which continue to travel down the collider beam-pipe, close to the axis defined by the intitial direction of motion of the proton.

[2]Whether a particular process is a neutral or charged current event is determined by whether or not the lepton maintains its charge at the upper vertex.

4.1.1 Kinematic nomenclature of DIS

We define the following Lorentz invariant kinematic variables to describe the DIS process,

$$s = (p+k)^2, \;\; W^2 = (p+q)^2, \;\; Q^2 = -q^2 = -(k-k')^2, \tag{4.1}$$

where s is the centre-of-mass energy squared, W^2 is the square of the invariant mass of the hadronic final state X, and Q^2 is the invariant mass squared of the exchanged virtual boson.

In order that the DIS process probes the proton with a high resolution, and thus resolves substructure within the proton rather than its gross properties, we require a *high virtuality* for the mediating photon, that is $M_p^2 \ll Q^2$. In this situation the probing photon has a wavelength $\lambda \sim 1/Q$ sufficiently small to resolve the internal structure of the hadron. Moreover, in order to preclude (for simplicity of analysis) neutral current DIS events involving the exchange of a Z^0 boson, we require that that same virtuality is constrained from above by the mass of the Z-boson, such that $Q^2 \ll M_Z^2$. As the contribution from DIS processes involving the Z^0 gauge boson is suppressed by a factor $\frac{Q^2}{Q^2+M_Z^2}$, relative to the contribution from those events mediated by photons, we can then with justification neglect these effects.

In the framework of DIS, it is convenient to define two dimensionless variables, x and y, using the standard kinematic quantities already defined in (4.1). It is instructive to show these quantities evaluated in the proton rest frame, or so-called laboratory frame, wherein the rest mass energy of the proton is given by M_P, and in which the energies of the incident and scattered lepton are given by E and E' respectively. We define $\nu = p.q = M_P(E'-E)$, and then write

$$\begin{aligned} x = \frac{Q^2}{2\nu} &= \frac{Q^2}{2M_P(E'-E)} \text{ and} \\ y = \frac{p.q}{p.k} &= 1 - E'/E, \end{aligned} \tag{4.2}$$

where M_P is the proton rest mass. Each of these variables carries an aesthetically physical interpretation. The fraction of energy carried by the virtual photon in the proton rest frame is given by y, whilst x is the celebrated Bjorken-x variable, which we shall interpret within the context of the naive parton model as the fraction of the proton's momentum carried by the struck parton. With these interpretations, x and y ought to be strictly bound between 0 and 1, and it is clear by reference to the kinematics in the rest frame of the proton, (4.2), that this is true.

Two independent variables are required to describe the kinematics of $\gamma^* P \to X$ inclusive DIS subprocess, and traditionally Q^2 and x are the preferred choice. We discuss the behaviour of DIS observables in a two dimensional plane, (x, Q^2).

In the high energy limit where particle masses can safely be neglected by comparison with the interaction energy, the invariant masses of the virtual photon and hadronic final state can be respectively written, using these variables, in the concise forms

$$Q^2 = s\, y\, x \text{ and } W^2 = Q^2 \frac{1-x}{x}.$$

4.1.2 Covariant formulation of deep inelastic scattering

We can formulate a description of the DIS process covariantly - the scattering amplitude for the generic process illustrated in Fig. 4.1 can be written

$$\mathcal{M} = e\bar{u}(k')\gamma^\mu u(k)\frac{1}{q^2}\langle X|j_\mu(0)|P\rangle, \tag{4.3}$$

with $\mathcal{M}$ the scattering amplitude, j_μ the electromagnetic current and $|X\rangle$ and $|P\rangle$ representing the final and initial hadronic states respectively. Crucially, we can factor the differential cross-section, proportional to the scattering amplitude squared, into a leptonic, $L_{\mu\nu}$, and a hadronic, $W^{\mu\nu}$, tensor

$$\frac{d^2\sigma}{dxdQ^2} \sim L_{\mu\nu}W^{\mu\nu}. \tag{4.4}$$

The leptonic piece is completely determined by quantum electrodynamics and is readily calculated by implementing the relevant Feynman rules,

$$L_{\mu\nu} = e^2 \sum_{\text{spins}} \left[\bar{u}(k')\gamma_\mu u(k)\right]\left[\bar{u}(k')\gamma_\nu u(k)\right]^*.$$

Using the machinery and trace technologies found in standard texts, this can be simplified to obtain

$$L_{\mu\nu} = 4e^2(k_\mu k'_\nu + k_\nu k'_\mu - g_{\mu\nu}\, k\cdot k'). \tag{4.5}$$

The hadronic piece, corresponding to the hatched blob in Fig. 4.1, and which contains all the information concerning how the electromagnetic current, j_μ, interacts with the proton target, is

given by [4] (summing implicitly over spin states)

$$\begin{aligned} W_{\mu\nu}(p,q) &= \frac{1}{4\pi}\sum_X \langle P|j_\nu^\dagger(0)|X\rangle\langle X|j_\mu(0)|P\rangle(2\pi)^4\delta^4(q+p-p_X) \\ &= \frac{1}{4\pi}\int d^4z\, e^{iq.z}\langle P|[j_\nu^\dagger(z), j_\mu(0)]|P\rangle. \end{aligned}$$

The intermediate steps are implemented through use of the completeness of the final states X, rewriting the delta function in its integral form, and noting that the second term of the current commutator is identically zero due to energy-momentum conservation.

Gauge invariance implies the Ward identities which in turn ensure that the electromagnetic current is conserved, $q \cdot W = 0$, and so we can construct the most general tensor structure from those quantities available, the momenta p, q and the spacetime metric g [4]. We obtain

$$W^{\mu\nu}(p,q) = \left(g^{\mu\nu} - \frac{q^\mu q^\nu}{q^2}\right) W_1(x,Q^2) + \left(p^\mu + \frac{1}{2x}q^\mu\right)\left(p^\nu + \frac{1}{2x}q^\nu\right) W_2(x,Q^2). \tag{4.6}$$

This leads, on contraction with (4.5), to the general scattering cross-section for the generic DIS process [4].

$$\frac{d^2\sigma}{dxdQ^2} = \frac{4\pi\alpha^2}{xQ^4}\left[y^2x\, F_1(x,Q^2) + (1-y)F_2(x,Q^2)\right] \tag{4.7}$$

Where we have defined the dimensionless functions $F_1 = W_1$ and $F_2 = \nu W_2$, which parameterize our ignorance of the intimate structure of the proton, and can depend solely on the independent scalar variables x and Q^2.

4.2 The (naive) quark parton model

The (naive) quark parton framework describing deep inelastic scattering predates the development of QCD, having been formulated in the 1960's [5], but remains a steadfastly useful intuitive apparatus for considering the internal structure of the proton, and indeed will prove to be a first step towards a more profound understanding.

The model is constructed around two basic assumptions:

- The initial proton system is considered to be a kinematically uniform collection of point-like constituents, *partons*, travelling with the bulk velocity of the fast moving proton. The individual partons then have the proton momentum distributed amongst them.

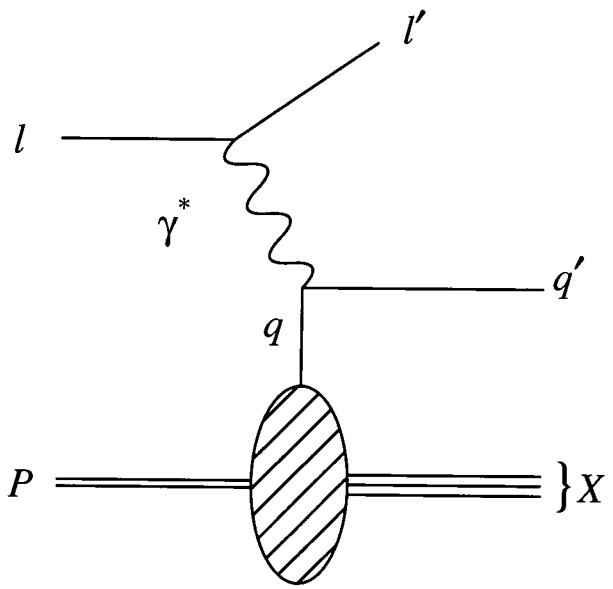

Figure 4.2: The quark-parton description of deep inelastic scattering. A photon probe scatters on a partonic constituent of the proton.

- At high Q^2 the probed parton is taken to be *unconstrained* within the hadron. Given that free partons had (and have since) not been witnessed, this might seem like a relatively ad hoc ansatz, but it transpires has a natural justification within the context of perturbative QCD, namely *asymptotic freedom.*

Within the laboratory frame, we understand that the interaction of the parton with the virtual photon happens over a far shorter timescale than any potential interactions with passive constituents, because of relativistic time dilation. Armed with these precepts, one can express the interaction of the probing gauge boson with the proton as the sum over all incoherent scatterings of the photon with the constituent charged partons, which gives rise to an expression for the differential total cross-section for production in DIS,

$$\frac{d^2\sigma}{dxdQ^2} = \sum_q \int_0^1 d\xi f_q(\xi) \frac{d^2\hat{\sigma}_q}{dxdQ^2}, \tag{4.8}$$

where $\hat{\sigma}$ is the *partonic cross-section*, describing a point-like interaction between the probe and constituent parton from the proton. The functions, $f_q(\xi)$, are termed *parton distribution functions*, and are interpreted as the probability of finding a parton, q, carrying a fraction, ξ, of the parent proton's longitudinal momentum.

As an aside, we explicitly identify the longitudinal momentum fraction of the struck parton with the Bjorken variable x. In the 'Breit' or infinite momentum frame, in which the four momentum of the proton is decomposed as $p^\mu \simeq (p, 0, 0, p)$, the partons should possess negligible transverse momentum for the proton to remain coherent and intact. The struck parton remains almost on mass shell, $m_q \simeq 0$, throughout the elastic interaction and so we find, by decomposing the four momentum of the struck parton, $p'_q = q + p_q$,

$$0 \simeq m_q^2 = (p'_q)^2 = (q + \xi p)^2 = -Q^2 + 2\xi(p \cdot q)$$
$$\xi = Q^2/p \cdot q = x.$$

We can also determine the partonic cross-section using QED, anticipating the fermionic nature of the proton constituents. The spin averaged matrix element for massless $e^- q \to e^- q$ scattering can be obtained from the matrix element for $e^+e^- \to q\bar{q}$ scattering through the use of a crossing symmetry, although in this case it as simple to determine the partonic cross-section from first principles. Using the Feynman rules for electron-quark scattering we obtain the relevant matrix element averaged over initial state spins and colours, and summed over those of the final state [1, 4],

$$\overline{\sum}|\mathcal{M}|^2 = 2Q_q^2 e^4 \frac{\hat{s}^2 + \hat{u}^2}{\hat{t}^2},$$

where Q_q is the partonic charge in units of electronic charge, and the $\hat{s} = \xi Q^2/xy$, $\hat{t} = -Q^2$ and $\hat{u} = \xi Q^2(y-1)/xy$ are the subprocess Mandelstam variables reexpressed in DIS nomenclature.

The partonic cross-section can be rearranged in a similar form to (4.7) to give

$$\frac{d\hat{\sigma}_q}{dQ^2} = \frac{2\pi\alpha^2 Q_q^2}{Q^4}[1 + (1-y)^2],$$

which on inserting into (4.8) gives a total cross-section

$$\frac{d^2\sigma}{dxdQ^2} = \frac{4\pi\alpha^2}{xQ^4} \sum_q f_q(x) Q_q^2 \frac{x}{2}[1 + (1-y)^2], \tag{4.9}$$

where the sum extends over all possible parton species coupling to the probing boson, and we have used the identity $\int_0^1 dx \delta(x - \xi) = 1$ to extract the double differential cross-section.

Comparing the coefficients of y^2 and $(1-y)$ of this latter expression with those of (4.7) we extract the following form for the structure functions [1, 4]

$$F_2(x) = 2xF_1(x) = \sum_q Q_q^2 x f_q(x), \tag{4.10}$$

The fact that F_1 and F_2 are not independent quantities is a property of DIS interactions involving spin-$\frac{1}{2}$ partons, and is known as the *Callan-Gross* relation. The combinations F_1 and $F_L = (F_2 - 2xF_1)$ correspond to the absorption by the struck parton of transverse and longitudinally polarized photons. [3] The Callan-Gross relation is then to be physically understood in that a spin-$\frac{1}{2}$ particle is unable to absorb a photon in a longitudinally polarized state. Conversely, if the partons within the proton had been spin-0 particles, they would have been unable to absorb transversely polarized photons, and we would anticipate that $F_1 = 0$ and $F_L = F_2$.[4] That this is experimentally well discounted cements the identification of the partons with particles of spin-$\frac{1}{2}$ fermionic character.

Note that, within this approximation, the structure functions depend *solely* upon the dimensionless variable x, and are independent of Q^2. This is the famous *Bjorken scaling* phenomenon [5, 6], and experimentally is obeyed, to a good approximation, for moderate $x \sim 0.1 - 0.2$, over a wide range $1 \lesssim Q^2 \lesssim 10^3$ GeV^2. We might have anticipated this scaling behaviour a priori, as by construction within the naive parton model, we are scattering a photon from point-like free objects. If this were not the case, and the photon interacted with partons possessing further substructure, the dimensionless structure functions would require some additional scale characterising their size and carrying the dimensions of Q^2.

4.2.1 Collective behaviour of the proton's partons

Our investigations into baryon structure so far have led us to a picture of the proton as consisting of pointlike spin-$\frac{1}{2}$ particles, which we have tentatively identified with the quarks of quantum chromodynamics (QCD). It is possible to produce a consistent spectroscopy of the lightest baryons by constructing flavour combinations of the three light quarks first conceived of by Gell-Mann and Zweig, in 1964 [7, 8]. The proton in this picture consists of two u quarks, carrying charge $+\frac{2}{3}e$ and one d quark, carrying charge $-\frac{1}{3}e$, to fulfil the requirement that its net charge is $+e$.

[3] As the scattering process is mediated by a *virtual* photon, it is not restricted to the physical transverse polarization, but rather can also possess unphysical longitudinal polarization states.

[4] These relations are true only within the context of this model. When a more sophisticated QCD analysis is used, the Callan-Gross relation is violated beyond leading order in α_s by logarithms in Q^2.

We can test the veracity of this view of proton structure by reference to the parton distribution functions defined in the previous section. In principle, these ought to provide a comprehensive description of the proton properties and so it should be possible to recover the net properties and quantum numbers of the proton by summing over the contributions from its constituent partons. We can recover the quantum numbers of the proton through the relations[5],

$$\int_0^1 dx\Big\{f_u(x) - f_{\bar{u}}(x)\Big\} = 2, \quad \int_0^1 dx\Big\{f_d(x) - f_{\bar{d}}(x)\Big\} = 1 \text{ and } \int_0^1 dx\Big\{f_{q'}(x) - f_{\bar{q}'}(x)\Big\} = 0.$$

Where $q' = s, c...$, those quark species not contributing to the quantum number of the proton.

We can also investigate the way in which the gross system momentum is distributed amongst the partons. Our initial expectation from the simple model is that the distributions in $F_2(x)$ should be peaked around $x \sim \frac{1}{3}$, as the momentum would naively be carried equally between the three quarks, with some smearing Fermi motion corrections due to their confinement within the proton. Experimentally, however, we find a quite different situation - the distribution peaks very strongly at smaller values of x, which leads us to the conclusion that our model is not sufficiently comprehensive to include all the constituents present in the proton, that are able to participate in the neutral current interaction.

Moreover, if we calculate the total momentum carried by the partons apparent in our model,

$$\sum_q \int_0^1 dx\, x f_q(x),$$

we should naturally expect that this will account for the total momentum of the proton. However, we find experimentally that only about one half of the net momentum is accounted for in this way, and so a substantial amount is clearly carried by electrically neutral particles that are invisible to the probing photon.

In the next section, these two inconsistencies will be resolved within the framework of perturbative quantum chromodynamics, the gauge theory of strong interactions with coupling α_s. The empirical shape of the momentum distribution will then be understood in terms of a *sea* distribution of charged quark-antiquark pairs, $q\bar{q}$, residing alongside the quantum number carrying *valence* quarks *uud*, and peaking at small values of x, whilst we will find that the gluon

[5]We anticipate, in passing, the potential for contribution to proton structure made by sea quark pairs, $q\bar{q}$.

content of the proton will readily account for the missing longitudinal momentum carried by uncharged particles.

4.3 The QCD improved parton model

We henceforth consider the naive quark-parton model of the previous section as the tree level, $\mathcal{O}(1)$, contribution to a perturbative expansion in α_s, the strong coupling. At the next order, $\mathcal{O}(\alpha_s)$, we must consider the possibility of the production of an additional parton, a gluon, in the final state, virtual gluon loops, or that the photon interacts with a gluon from the proton through the quark box mechanism of $\gamma^* g$ fusion. This latter $g \to q\bar{q}$ mechanism admits the possibility of an interaction occuring between the photon and quarks carrying quantum numbers not nominally found within a specific hadron according to the Gell-Mann and Zweig spectroscopy.

Qualitatively we can think in terms of the photon probing an intricate tapestry (see Fig. 4.3) not only of valence quarks, but also sea quarks and gluons within the proton. At ever increasing values of Q^2 we probe an increasing number of constituents within the proton, and the bulk momentum of the system must become correspondingly diluted amongst them - hence we should expect to witness a violation of the Bjorken scaling phenomenon. As Q^2 increases the structure functions should exhibit an enhancement at small x, as the probablility of finding a parton with a small momentum fraction increases, compensated by a suppression at large x.

In perturbative QCD we can calculate the $\mathcal{O}(\alpha_s)$ corrections to the naive parton model in the regime where the strong coupling α_s is small, namely $Q^2 \gg \Lambda^2_{\rm QCD}$, where $\Lambda_{\rm QCD} \sim 0.2$ GeV, due to asymptotic freedom. The graphs contributing to DIS at this order are shown in Fig. 4.4, which illustrates those corrections due to real, (d) - (e), and virtual, (a) - (c), emission of gluons, and a further important graph, (f), the mechanism by which the virtual photon interacts with a gluon from within the proton, $\gamma^* g$ fusion, Finally the *higher twist* graph is shown in Fig. 4.5. arising from an interaction between the proton remnants and the struck parton in the final state. These contributions are suppressed by a relative factor of $1/Q^2$ [3].

The effect of including real gluon emission in the analysis of the observable F_2 is to add an $\mathcal{O}(\alpha_s)$ correction to (4.10). This correction reflects the non-zero probability within pQCD of the

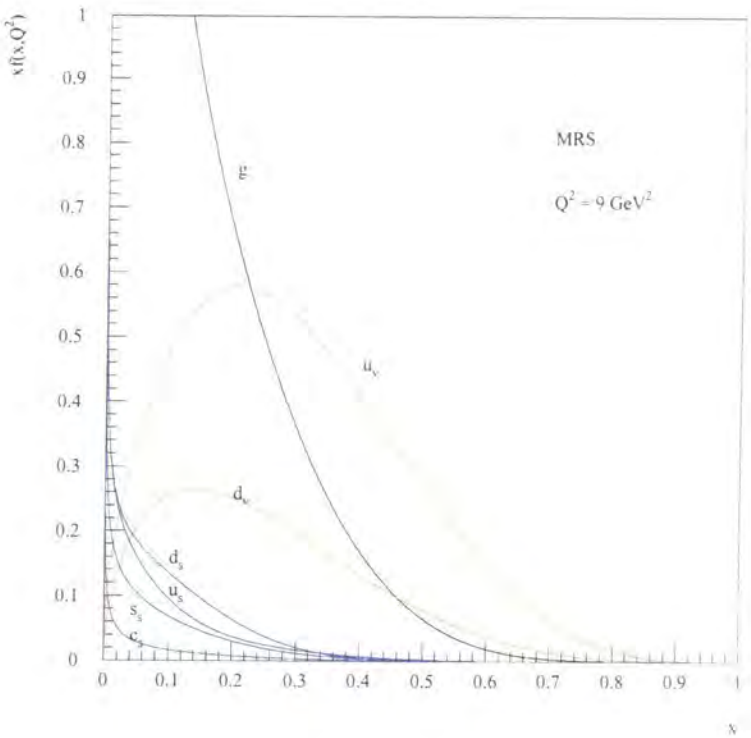

Figure 4.3: Plot illustrating the rich QCD structure of the proton, parton distributions taken from ref. [11]. The dominant distribution at small x is due to the gluon, g, while at intermediate values of x, the valence quark distributions $u_{\rm V}$ and $d_{\rm V}$ become significant. There also appear sea quark, $u_{\rm S}, d_{\rm S}, s_{\rm S}, c_{\rm S}$, (and anti-quark) distributions, including the heavy charm, which arise from $q\bar{q}$ pair production, and tend to become the significant quark component of the proton at small x.

propagating quark radiating a gluon and thus diminishing its longitudinal momentum fraction. This probability depends on Q^2, and so induces a momentum dependence that violates Bjorken scaling. F_2 is calculated [4],

$$F_2(x,Q^2) = x\sum_q Q_q^2 \int_x^1 \frac{d\xi}{\xi} f_q(\xi) \left\{ \delta\left(1-\frac{x}{\xi}\right) + \frac{\alpha_{\rm S}}{2\pi} P_{qq}\left(\frac{x}{\xi}\right) \log\left(\frac{Q^2}{\kappa^2}\right) \right\}. \qquad (4.11)$$

where $P_{qq}(z)$ is a *splitting function*, calculable within pQCD, and whose precise nature will be discussed in greater detail later. The appearance of κ^2 is a computational artifact introduced to prevent the integration over the emitted gluon's transverse momentum running into the

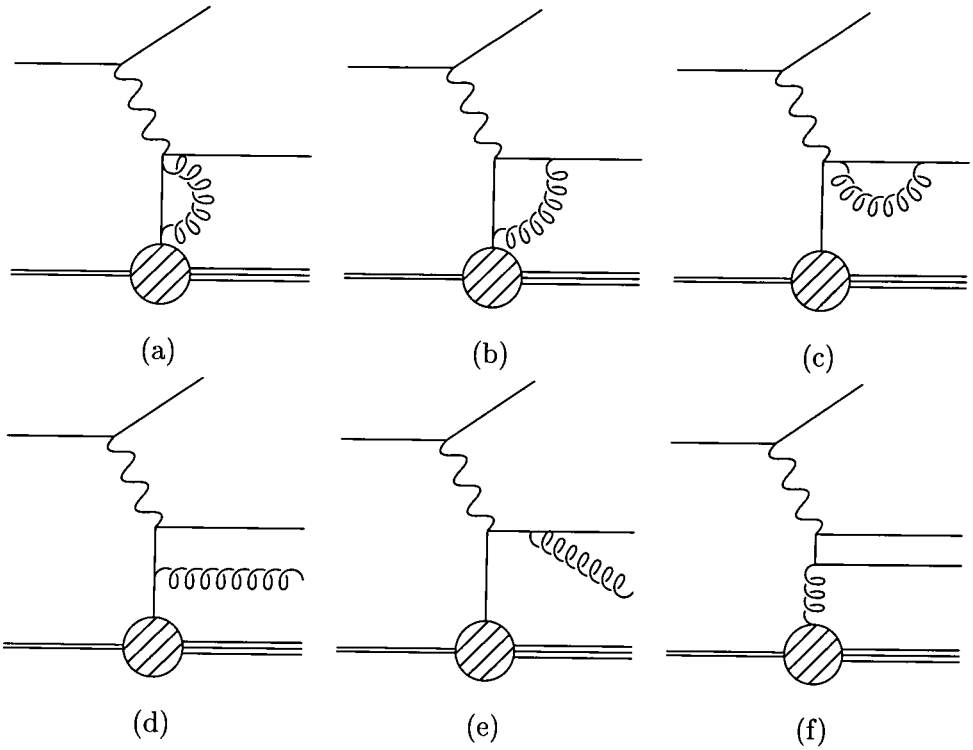

Figure 4.4: Graphs contributing at $\mathcal{O}(\alpha_s)$ to deep inelastic ep scattering. The virtual gluon loops, (a) - (c), generate an $\mathcal{O}(\alpha_s)$ contribution through interference with the tree level diagram. Graphs (d) - (e) correspond to real gluon emission and (f) corresponds to interaction with a gluon from within the proton.

singularity corresponding to the collinear limit, $k_T^2 = 0$,

$$\int_{\kappa^2}^{Q^2} \frac{dk_T^2}{k_T^2} = \log\left(\frac{Q^2}{\kappa^2}\right). \tag{4.12}$$

We can now sweep the initial state collinear singularities ($\kappa^2 \to 0$) into a redefinition of the parton distribution functions through a redefinition of the parton distribution functions,

$$f_q(x,\mu_F^2) = f_q(x) + \frac{\alpha_s}{2\pi}\int_x^1 \frac{d\xi}{\xi} f_q(\xi) P_{qq}\left(\frac{x}{\xi}\right) \log\left(\frac{\mu_F^2}{\kappa^2}\right),$$

where they are now dependent on some factorization scale, μ_F^2. The process of absorbing the singularities in this way gives rise to a gentle (logarithmic) scaling violation of the structure functions with Q^2 in the following manner [4],

$$F_2(x,Q^2) = x\sum_q Q_q^2 \int_x^1 \frac{d\xi}{\xi} f_q(\xi,\mu_F^2)\left\{\delta\left(1-\frac{x}{\xi}\right) + \frac{\alpha_s}{2\pi} P_{qq}\left(\frac{x}{\xi}\right)\log\left(\frac{Q^2}{\mu_F^2}\right)\right\}. \tag{4.13}$$

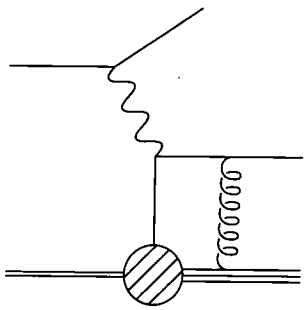

Figure 4.5: Graph illustrating the $\mathcal{O}(\alpha_s)$ higher twist contribution to deep inelastic *ep* scattering.

Perturbative QCD does not allow us to determine the structure functions from first principles but it does specify their Q^2 evolution. So if we determine them from experiment at some scale Q_0^2 then we can calculate them at any other perturbative scale Q^2. We can extract their value from experimental measurements of the structure functions through the relation

$$F_2(x, Q^2) = x \sum_q Q_q^2 f_q(x, Q^2).$$

Once we have a parameterization for them, pQCD permits us to evolve these empirical distributions throughout the relevant (x, Q^2) kinematic plane.

4.3.1 Factorization of the cross-section.

In the formulation of the naive quark-parton model, we found we were able to rather simply diagonalize observables such as F_2 into a convolution of structure functions and a partonic cross-section. Within a subsequent QCD analysis we witnessed the failure of this simple diagonalization, but discovered a more general concept of factorization [4]. We illustrated in the previous section how the observable cross-section for deep inelastic scattering is rendered a finite quantity through factorizing initial state singularities, corresponding to soft non-perturbative physics, into a redefinition of the parton distribution functions.

This behaviour is typical of treatments of QCD processes. The cross-section factorizes into a soft piece, comprising the long distance physics that cannot, in principle, be calculated perturbatively, $f_{i,h}(x, \mu_F^2)$, and a hard part, $\hat{\sigma}_i$, describing the short distance partonic scattering.

Such a formulation can be written

$$\sigma(x,Q^2) = \sum_{i=q,g} \int_x^1 d\xi \, f_{i,h}\left(\xi,\mu_F^2\right) \, \hat{\sigma}_i\left(\frac{x}{\xi},\frac{Q^2}{\mu_F^2},\frac{Q^2}{\mu_R^2},\alpha_s\right), \tag{4.14}$$

with μ_F^2 and μ_R^2 the factorization and renormalisation scales, typical of the hard process at hand, and usually set for computational simplicity such that $\mu_F^2 = \mu_R^2 = Q^2$. The factorization scale partitions the physics into long and short distance phenomena, whilst the renormalisation scale acts to regulate ultraviolet divergences arising from loop integrations. If the scale of a subprocess is less than the factorization scale, it is absorbed within the parton densities, whilst if the scale exceeds μ_F^2, then the subprocess is considered legitimately calculable within pQCD.

The quantities $f_{i,h}(x,Q^2)$ (for examples see ref. [11]) are globally extracted by a detailed fit to a broad portfolio of diverse experimental data. They have the property of universality, that is, although specific to the hadron, h, in question they are independent of the hard process in which they participate. The partonic cross-sections $\hat{\sigma}_i$ can, by construction, be expressed as a perturbative expansion in α_s. They are functions of the two scales μ_F^2 and μ_R^2 and the kinematic variables, and are independent of the hadronic system involved in the interaction.

Clearly μ_F^2 and μ_R^2 are artifacts of the perturbative computation and should exert no influence on observable quantities. For any observable quantity, U, this can be formulated

$$\frac{\partial U}{\partial \mu_F^2} = \frac{\partial U}{\partial \mu_R^2} = 0.$$

However, in any (necessarily!) truncated perturbative expansion of the observable U, there will be residual scale dependencies, arising from the disruption of the delicate way in which the higher order coefficients vary with the scale in order for the complete series to be independent. The greater the number of terms included in the expansion, the slighter will be any residual dependencies on the choice of scales, μ_R^2 and μ_F^2.

This property of factorization is a typical feature of pQCD, and can be generalized beyond the specific case at hand, for example to the case of hadron-hadron scattering.

4.4 The DGLAP evolution equations

To date in our QCD description of the proton we have included only the effect of the real and virtual gluon emission graphs in the evolution of the structure function, $F_2(x, Q^2)$. There is one more crucial $\mathcal{O}(\alpha_s)$ graph, hitherto neglected in our discussion - that corresponding to the possibility of the neutral current interacting with a gluon constituent of the proton indirectly through the quark box mechanism. At $\mathcal{O}(\alpha_s)$ this allows for the generation of a sea distribution of quarks as the radiated gluon is able to fragment further into a $q\bar{q}$ pair.

This process is illustrated in Fig. 4.4 (f), and as we move to smaller values of x, we will find that this is by far the dominant source of partons within the proton. Defining, for clarity of notation, $f_{q,h}(x, Q^2) = q(x, Q^2)$, and $f_{g,h}(x, Q^2) = g(x, Q^2)$, it is possible to show [1] that the effect of folding into the analysis this sixth $\mathcal{O}(\alpha_s)$ graph is to acknowledge the presence of gluons within the proton. The gluon distribution requires its own evolution equation which couples to the *singlet* combination of quark flavours, $\sum_{i=q,\bar{q}} q_i$, as quarks and gluons each contribute to the others splitting. We find a coupled pair of evolution equations [12, 13, 14], the DGLAP equations[6],

$$\begin{aligned}
\frac{\partial q_i(x,Q^2)}{\partial \log Q^2} &= \frac{\alpha_s}{2\pi}\int_x^1 \frac{d\xi}{\xi}\left\{q_i(\xi,Q^2)\mathcal{P}_{qq}\left(\frac{x}{\xi}\right) + g(\xi,Q^2)\mathcal{P}_{qg}\left(\frac{x}{\xi}\right)\right\} \quad \text{and} \\
\frac{\partial g(x,Q^2)}{\partial \log Q^2} &= \frac{\alpha_s}{2\pi}\int_x^1 \frac{d\xi}{\xi}\left\{g(\xi,Q^2)\mathcal{P}_{gg}\left(\frac{x}{\xi}\right) + \sum_{i=q,\bar{q}} q_i(\xi,Q^2)\mathcal{P}_{gq}\left(\frac{x}{\xi}\right)\right\}. \qquad (4.15)
\end{aligned}$$

The second term on the right hand side of each of the DGLAP equations corresponds to the eventuality of finding a daughter parton of type other than its parent species within the proton. Notice that the gluon receives contributions from all quark species $q, \bar{q}$.

We can define a set of *non-singlet* parton distributions, linear combinations of the quantity $q_{\rm NS} = q - \bar{q}$ which completely decouple from the gluon evolution.

$$\frac{\partial q_{\rm NS}(x,Q^2)}{\partial \log Q^2} = \frac{\alpha_s}{2\pi}\int_x^1 \frac{d\xi}{\xi}\mathcal{P}_{qq}\left(\frac{x}{\xi}\right).$$

The *splitting functions*, $\mathcal{P}_{fi}\left(\frac{x}{\xi}\right)$, at lowest order [14] give the probability of finding a daughter parton f with longitudinal momentum fraction x within a parent parton i carrying longitudinal

[6] So named after the progenitors of the equations, Dokshitzer, Gribov, Lipatov, Altarelli and Parisi.

momentum fraction ξ, and transverse momentum squared less than μ_F^2. They give the likelihood of a high momentum parton radiating some of its longitudinal momentum away and continuing to propagate with a reduced momentum fraction. Qualitatively, we understand that large x partons will move to lower values of x through this branching mechanism. The newly created partons will tend to have small momentum fractions, and so the bulk of the parton distribution functions becomes concentrated towards smaller values of x.

The splitting functions are determined as a pertubative expansion in α_s,

$$\mathcal{P}_{fi}(z) = P_{fi}^{(0)}(z) + \frac{\alpha_s}{2\pi} P_{fi}^{(1)}(z) + ...$$

where the lowest order coefficients are readily calculable using the Feynman rules of QCD, [14]. The splitting functions have been known at next-to-leading order for some time [15, 16, 17], and

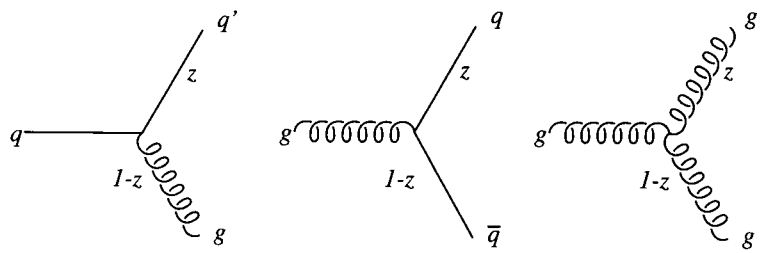

$P_{qq}^{(0)}(z),\ P_{gq}^{(0)}(1-z)$ $\qquad$ $P_{qg}^{(0)}(z)$ $\qquad$ $P_{gg}^{(0)}(z)$

Figure 4.6: Feynman graphs for the leading order QCD splitting functions.

partial information regarding their next-to-next-to-leading order behaviour has recently become available. The explicit calculation to leading order yields the following results for the $P_{ij}^{(0)}$:

$$\begin{aligned}
P_{qq}^{(0)}(z) &= C_F \left\{ \frac{1+z^2}{(1-z)_+} + \frac{3}{2}\,\delta(1-z) \right\}, \\
P_{qg}^{(0)}(z) &= T \left\{ z^2 + (1-z)^2 \right\}, \\
P_{gq}^{(0)}(z) &= C_F \left\{ \frac{1+(1-z)^2}{z} \right\} \quad \text{and} \\
P_{gg}^{(0)}(z) &= 2C_A \left\{ \frac{z}{(1-z)_+} + \frac{1-z}{z} + z(1-z) \right\} + \frac{11C_A - 4Tn_f}{6}\,\delta(1-z), \qquad (4.16)
\end{aligned}$$

corresponding to the graphs shown in Fig. 4.6. The number of active light flavours is denoted by n_f, and charge conjugation and flavour symmetry demand that P_{qg} and P_{gq} are independent of flavour, and identical for q and $\bar{q}$ respectively. The coefficients C_F, C_A and T are the colour

factors of QCD, and the plus prescription, which regulates the splitting functions at $z = 1$, is given by:

$$\int_0^1 dz \frac{f(z)}{(1-z)_+} = \int_0^1 \frac{f(z) - f(1)}{1-z}.$$

The origin of this prescription lies in a delicate cancellation of singularities from graphs containing virtual gluon loops. Such a cancellation is a necessary requirement of the Kinoshita, Lee and Nauenburg theorem [18], which requires that sufficiently inclusive quantities be free from singularities in the massless limit.

4.5 Resummations and ladders

Evolution equations can also be viewed from a complementary direction, that of performing a *resummation* in large logarithms of the kinematic variables. For sizeable values of Q^2, terms containing $\log(Q^2/Q_0^2)$ can become dangerously large, overwhelming the smallness of the coupling in a series expansion. We will briefly sketch the way in which the leading DGLAP equations resum contributions from terms of type $[\alpha_s \log(Q^2/Q_0^2)]^r$ to all orders. For simplicity we only consider the non-singlet parton distributions, $q_{\rm NS} = q - \bar{q}$, noticing that the contribution from the gluon content of the proton in Eqn. (4.15) cancels in the difference. The evolution equation for the non-singlet distribution reads [2]

$$\frac{\partial q_{\rm NS}(x,Q^2)}{\partial \log Q^2} = \frac{\alpha_s}{2\pi}\int_x^1 \frac{d\xi}{\xi} q_{\rm NS}(\xi,Q^2) P_{qq}\left(\frac{x}{\xi}\right) = \frac{\alpha_s}{2\pi}\int_0^1 d\xi \int_0^1 dz\ \delta(x-\xi z) q_{\rm NS}(\xi,Q^2) P_{qq}(z). \tag{4.17}$$

In order to disentangle the convolution in ξ and x, we now introduce the concept of a *moment* defined by the Mellin transform

$$\tilde{q}_{\rm NS}(\omega,Q^2) = \int_0^1 \frac{dx}{x} x^\omega q_{\rm NS}(x,Q^2). \tag{4.18}$$

The use of Mellin transforms in this way is ubiquitous in analytic studies of DIS. For fixed values of the coupling α_s, they diagonalize the evolution equation, putting it in an algebraically tractable form in moment space,

$$\frac{\partial \tilde{q}_{\rm NS}(\omega,Q^2)}{\partial \log Q^2} = \frac{\alpha_s}{2\pi}\int_0^1 \frac{d\xi}{\xi}\xi^\omega q_{\rm NS}(\xi,Q^2)\int_0^1 \frac{dz}{z} z^\omega P_{qq}(z) = \frac{\alpha_s}{2\pi}\tilde{q}_{\rm NS}(\omega,Q^2)\ A(\omega). \tag{4.19}$$

It is a simple procedure to invert this and obtain a solution for the moment, $\tilde{q}_{\rm NS}(\omega, Q^2)$,

$$\tilde{q}_{\rm NS}(\omega, Q^2) = C \exp\left(\frac{\alpha_{\rm s}}{2\pi} \log(Q^2/Q_0^2) A(\omega)\right) = C \sum_r \frac{1}{r!} \left[\frac{\alpha_{\rm s}}{2\pi} \log(Q^2/Q_0^2) A(\omega)\right]^r \qquad (4.20)$$

where in the final equality we have performed a series expansion for small values of $\alpha_{\rm s}$. It has been shown [13] that for an axial gauge, in which the gluon possess simply two physical polarization states, each of the terms $C[\alpha_{\rm s} \log(Q^2/Q_0^2) A(\omega)]^r$ corresponds to a *ladder diagram* with r rungs, for example, Fig. 4.7. A nested integral over transverse momentum k_r^2 in the

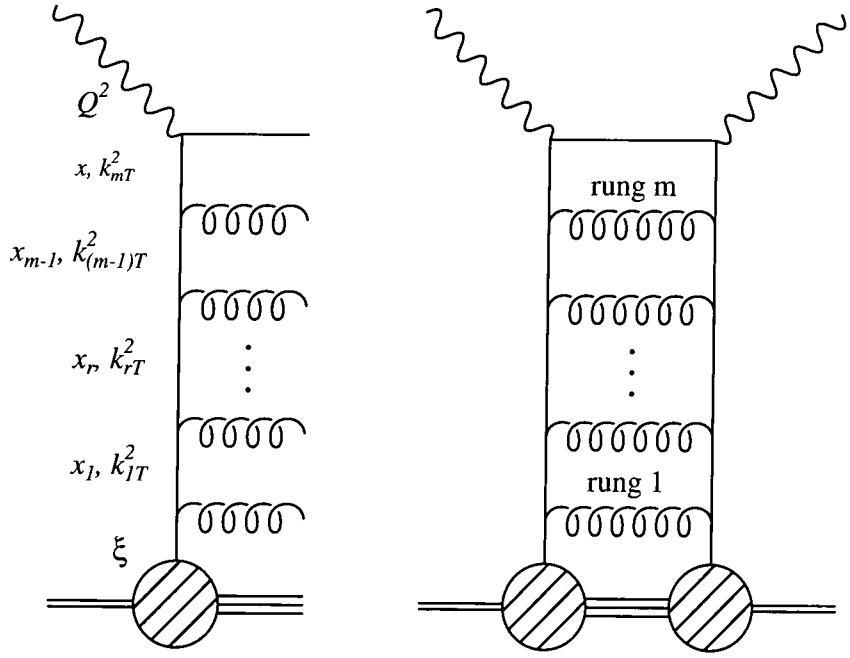

Figure 4.7: On the left a representation of a ladder amplitude of Eqn. (4.20), upon squaring this produces the ladder diagram on the right. A high virtuality photon probes the proton via an m rung parton cascade. The DGLAP formalism resums $\log(Q^2/Q_0^2)$ terms arising from the kinematic region where the transverse momentum of the emitted partons are strongly ordered, and the longitudinal momentum fractions are weakly ordered.

region of phase space where they are strongly ordered,

$$\int^{Q^2} \frac{dk_{m-1}^2}{k_{m-1}^2} \cdots \int^{k_{r+1}^2} \frac{dk_r^2}{k_r^2} \cdots \int^{k_2^2} \frac{dk_1^2}{k_1^2}$$

$$Q^2 \gg \ldots \gg k_r^2 \gg \ldots \gg k_1^2,$$

yields the logarithm in Q^2, whilst the coefficients $A(\omega)$ are obtained from a similarly nested integral over the weakly ordered longitudinal momentum fractions,

$$\int_x^1 \frac{dx_{m-1}}{x_{m-1}} \ldots \int_{x_{r+1}}^1 \frac{dx_r}{x_r} \ldots \int_{x_1}^1 \frac{d\xi}{\xi} \xi g(\xi)$$
$$x < x_{m-1} \ldots < x_r < \ldots < \xi.$$

4.6 The double leading logarithmic approximation

As we probe to smaller values of x, the gluon becomes the dominant component of the proton and we can also neglect the quark contributions to the gluon distribution function. From Eqn. (4.16) it is apparent that the singular part of $P_{gg}^{(0)}$ dominates the evolution,

$$P_{gg}^{(0)}(z) \simeq \frac{2C_A}{z}.$$

Notice that this formalism now corresponds to that discussed in the previous section for a non-singlet distribution, Eqn. (4.17), with the replacements $q_{\rm NS} \to g$ and $P_{qq} \to P_{gg}$. In this case (and for a fixed $\alpha_{\rm s}$) we can evaluate what kind of form we expect for the evolution at large Q^2 and smaller x. We have Eqn. (4.20), with the coefficient function given by

$$A(\omega) = \frac{\alpha_{\rm s}}{2\pi} \int_0^1 \frac{dz}{z} z^\omega P_{gg}(z) \simeq \bar{\alpha}_{\rm s} \int_0^1 \frac{dz}{z} z^{\omega-1} = \frac{\bar{\alpha}_{\rm s}}{\omega - 1}.$$

The inversion of the Mellin transform Eqn. (4.18) is written, and we obtain the gluon distribution in kinematic space

$$\begin{aligned} xg(x,Q^2) &= \oint_{C-i\infty}^{C+i\infty} \frac{d\omega}{2\pi i} x^{1-\omega} \tilde{g}(\omega, Q^2) \\ &= \int_{-i\infty}^{+i\infty} \frac{d\omega}{2\pi i} \tilde{g}(\omega, Q_0^2) \exp\left((\omega - 1) \log\left(\frac{1}{x}\right) + \frac{\bar{\alpha}_{\rm s}}{\omega - 1} \log\left(\frac{Q^2}{Q_0^2}\right)\right). \end{aligned}$$

This latter form can be evaluated in the saddle point approximation to eventually obtain an expression for the gluon distribution [4]

$$xg(x,Q^2) \sim \exp\left(2 \left[\bar{\alpha}_{\rm s} \log\left(\frac{1}{x}\right) \log\left(\frac{Q^2}{Q_0^2}\right)\right]^{\frac{1}{2}}\right). \tag{4.21}$$

This gluon distribution will grow more rapidly than any power of $\log(1/x)$, but more slowly than any power of x as $x \to 0$. The limiting behaviour of this gluon distribution function corresponds

to ladder diagrams whose emitted gluons have strong ordering in their longitudinal momenta as well as their transverse momenta, that is

$$x \ll x_{m-1} ... \ll x_r \ll ... \ll \xi.$$

This limit of the DGLAP equations effectively resums terms containing double logarithms of the type $[\alpha_s \log(Q^2/Q_0^2) \log(1/x)]^r$.

4.7 Other large logarithms

Along with the logarithm $\alpha_s \log(Q^2/Q_0^2)$, and the double logarithm $\alpha_s \log(Q^2/Q_0^2) \log(1/x)$ described in the previous section, as the centre of mass energies probed by HERA increased ever further (equivalently as we probe smaller x) it becomes possible that we encounter logarithms in $1/x$ fully non-leading in $\alpha_s \log(Q^2)$ which can become large. These too need to be addressed and resummed for a complete description of the parton distribution functions in this region of (x, Q^2).

At modern day particle colliders, events are generated whose kinematics correspond to considerable $\log(1/x)$, at moderate values of Q^2. In such a configuration the leading contribution will not be given by resummed logarithms of Q^2, but rather terms of the type $[\alpha_s \log(1/x)]^r$, such that the smallness of the coupling is overwhelmed by a logarithm in x. The prescription for resumming a series of this type is given by the BFKL equation[7].

We shall see that the BFKL equation predicts a very striking behaviour for the parton distributions at small x, and illustrate why it has not been possible to unambiguously identify the BFKL signature in standard observables. The remainder of this thesis is given over to phenomenological analyses of experimental processes where characteristic BFKL effects should become apparent.

[7]So named after its progenitors, Balitsky, Fadin, Kuraev and Lipatov.

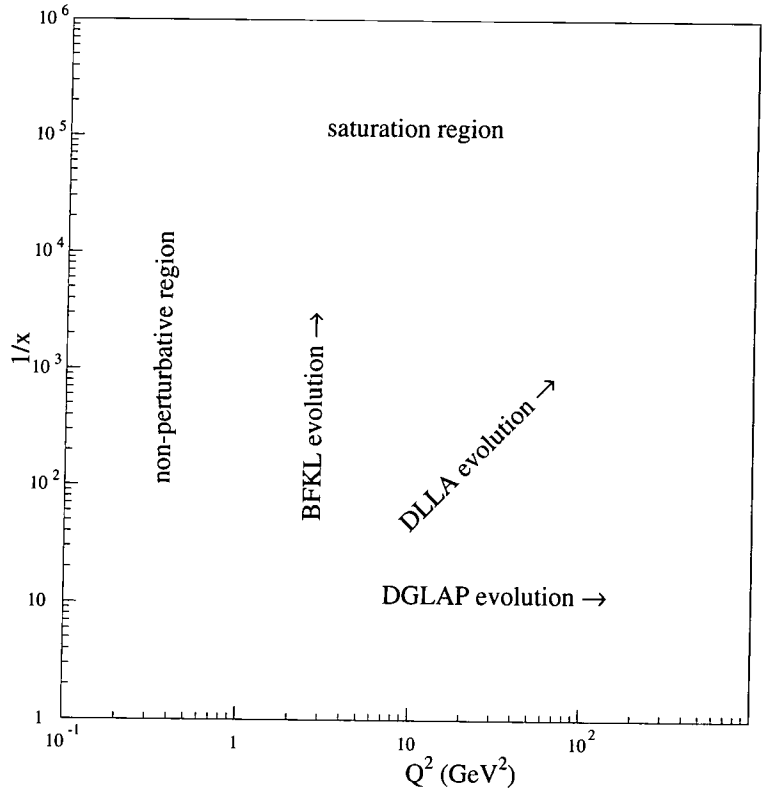

Figure 4.8: Plan of where potentially dangerous logarithms reside in the (x, Q^2) kinematic plane, and the appropriate formalism for their resummation. DGLAP evolution for large values of Q^2, DLLA for large values of Q^2 and moderately small values of x and BFKL for small x, and moderate values of Q^2.

Chapter 5

Gluon evolution at small x

In this chapter we will introduce the formalism necessary to apply QCD in the kinematic domain of small x and moderate Q^2, where terms of type $[\log(1/x)]^r$ are the dominant contribution to a perturbative expansion. We sketch the origins of the appropriate evolution equation in this region, and illustrate briefly the methodology for an analytic solution. This solution will highlight characteristic features, unique to small x physics, which we qualitatively assess. In the second part of the chapter, we discuss why resummation of the leading logarithm in $1/x$ appears to be deficient by reference to the next-to-leading-log[1] (NLL) corrections. We then motivate a physical constraint on the leading formalism that contributes at all orders, resulting in a modified BFKL equation, more appropriate for use in phenomenological applications. We then quantify, with reference to both leading-log (LL) and NLL results, the effect of imposing this correction on the BFKL kernel.

5.1 A brief resumé of the BFKL equation

When Q^2 is not too large, and x is small double logarithms in the kinematic variables no longer dominate, and we should focus instead on resumming completely the more significant

[1] A next-to-leading-log formalism resums terms of the type $\alpha_s\,[\alpha_s \log(1/x)]^r$, in comparison with the leading-log which simply sums terms of the form $[\alpha_s \log(1/x)]^r$.

$[\alpha_s \log(1/x)]^r$ terms, appreciating that we only took into account terms of this type accompanied by a logarithm in Q^2 in the DLLA previously. In order to include terms in $\alpha_s \log(1/x)$ fully, including those independent of logarithms in Q^2, we relax the strong ordering in the transverse momenta along the parton (gluon) emission cascade. In contrast to DGLAP evolution, we now have complete disarray, a random walk, in the transverse momenta of the emitted partons, characterized by a similarity in scale along the chain,

$$Q^2 \simeq ... \simeq k_r^2 \simeq ... \simeq k_1^2.$$

Recall that the strong ordering of the kinematic space in transverse momenta developed the $\log(Q^2/Q_0^2)$ dependence in the resummation previously. The appropriate quantity to describe the full transverse momentum dependence (and thus collect all $\log(1/x)$ terms) in this formalism will be an *unintegrated gluon distribution*, related to the conventional gluon distribution by

$$g(x, Q^2) = \int^{Q^2} dk^2 f(x, k^2). \tag{5.1}$$

We have unzipped the integration over the transverse momenta of the final parton in the chain. This makes explicit the full k^2 dependence of the gluon distribution, and not simply the leading $\alpha_s \log(Q^2/Q_0^2)$ terms.

The disorder of transverse momenta can in principle permit an intermediate parton to encroach into the infrared, $k^2 \lesssim 1$ GeV^2, where we anticipate our perturbative description will become inappropriate. This has ramifications for the application of the BFKL formalism in phenomenology, we should take care to ensure a fully consistent perturbative approach. How this is achieved practically will be discussed in greater depth later.

As in the case of the DLLA limit of DGLAP evolution, the longitudinal momenta, x_r of the emitted partons exhibit a strong ordering,

$$x \ll x_{m-1} \ll ... \ll x_r \ll ... \ll \xi,$$

and as before this gives rise to the logarithms in x. A full account of the derivation of the BFKL equation is beyond the scope of this thesis and can be found, for example, in [4, 19, 20, 21]. Instead we sketch a brief outline of its origins.

5.1.1 Bare bones of the BFKL kernel

We can illustrate how the structure of the BFKL equation arises without delving too deeply into a technical calculation in the following way. We consider the tree level parton-parton scattering process with gluon exchange in the t-channel[2], of Fig. 5.1 (a) as the bare, base unit of particular interest, and see how in the small x limit of QCD this generates the appropriate leading $\log s$ behaviour.

(a) Tree level amplitude (b) Reggeized gluon and effective vertex

Figure 5.1: Parton-parton scattering via gluon exchange in the t-channel. Graph (a) shows the tree-level process, graph (b) is an effective diagram, whose t-channel gluon has been reggeized by virtual gluonic corrections to (a), and whose effective vertex Γ incorporates the real gluonic corrections.

As in our earlier discussion of the QCD improved parton model, at NLO in α_s we should supplement our basic graph with a variety of (higher order) gluonic emissions. It can be shown that the diagrams that contribute to real gluon emission at $\mathcal{O}(\alpha_s^3)$ collectively conspire to generate an effective graph containing a non-local effective vertex factor, Γ, whose square Γ^2, is given by [2, 21]

$$\Gamma^2 = \bar{\alpha}_s \frac{k_T^2}{k_T'^2 q_T^2},$$

where the transverse momenta are as illustrated in Fig. 5.1(b). The asymmetry of the transverse momenta within the expression for the vertex factor originates in the strong ordering of the longitudinal momenta. There is a second generic type of graph that is manifest at $\mathcal{O}(\alpha_s^3)$, namely those involving virtual gluon loops, which generate interference terms when coupled to

[2]Here s and t refer to the invariant *Mandelstam variables* for two-body scattering, namely for the process $A + B \to C + D$, $s = (p_A + p_B)^2$ and $t = (p_A - p_C)^2$.

the tree-level diagram. In a similar way to the real emissions, these virtual gluon loops can be synthesized into a single, effective graph whose t-channel gluon propagator has been *reggeized*, that is, whose behaviour has been dressed in the Regge limit $s \gg -t$ with a gluon *Regge trajectory* [19, 20], α_g,

$$\frac{s}{k^2} \to \left(\frac{s}{k^2}\right)^{\alpha_g(k^2)}.$$

The net action of all higher order gluon emissions on the tree-level process is to generate a single effective gluon emission diagram, shown in Fig. 5.1 (b), which is leading in $\log s$.

5.1.2 An effective ladder diagram

The second crucial piece of machinery is the use of the eikonal approximation which allows a simplification of the diagrams involved in calculating the effective graph [21]. We are free to replace (imposing the appropriate colour factor) the quark lines of Fig. 5.1 (b) with gluons, and can then iterate the procedure of dressing the normal propagators, legs and vertices of the gluon components to the graphs akin to the previous subsection ad infinitum, at each stage collecting a contribution leading in $\log s$, to construct the generic amplitude for parton-parton scattering involving the emission of r gluons [22].

The full BFKL equation then describes a gluon evolution that pictorially comprises an infinite sum of effective ladder diagrams, consisting of amplitudes of the type depicted in Fig. 5.2 squared. The 'rails' of the ladder consist of reggeized gluons in the t-channel, and are coupled to the 'rungs', the emitted gluons via a non-local vertex, Γ. The BFKL evolution kernel is then constructed from the reggeized gluon propagator and the sum of graphs containing multiple gluon emissions from the effective vertices, keeping only the leading $\log s$ terms.

5.2 The leading log BFKL equation

In the LL BFKL formalism, whose origins have been sketched above, the evolution equation for the unintegrated gluon distribution, Eqn. (5.1), (performing a role analagous to the DGLAP

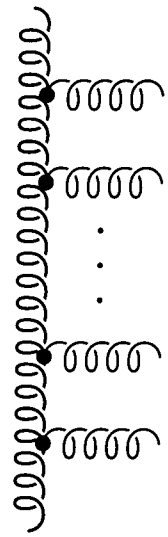

Figure 5.2: Effective amplitude contributing to the leading $\log(1/x)$ effective ladder diagram for high energy parton-parton scattering. The graph consists of reggeized gluons in the t-channel and a non-local effective vertex, which embody all manner of real and virtual gluon emissions. The ladder is generated by iterating successive units of Fig. 5.1 (b).

equations) is given by [19, 20, 21]

$$f(x,\boldsymbol{k}) = f^{(0)}(x,\boldsymbol{k}) + \bar{\alpha}_s \int_x^1 \frac{dz}{z} \int \frac{d^2\boldsymbol{q}}{\pi q^2} \left\{ f\left(\frac{x}{z}, \boldsymbol{k}+\boldsymbol{q}\right) - \frac{k^2}{q^2+(\boldsymbol{k}+\boldsymbol{q})^2} f\left(\frac{x}{z},\boldsymbol{k}\right) \right\}. \tag{5.2}$$

Here $\boldsymbol{k}$ is the transverse momentum vector, $k = |\boldsymbol{k}|$ and $\bar{\alpha}_s = N_c\ \alpha_s/\pi$. The equation displays the full angular dependence of the unintegrated gluon, whose role will be dominant at the small values of longitudinal momentum fraction x where the equation is valid. The inhomogeneous driving term, $f^{(0)}(x,\boldsymbol{k})$, is the boundary condition for the equation, from where we initiate BFKL evolution in $\log(1/x)$ at the reference point x_0.

Note the explicit angular dependence on the transverse momentum vector of the emitted gluon, $\boldsymbol{q}$, leading to non-trivial angular integrations in the kernel denominators. We can treat the dependence on the azimuthal angle, φ, by defining a new dimensionless unintegrated gluon structure function, $\phi(x,\boldsymbol{k})$, and making a Fourier decomposition [21],

$$k^2 f(x,\boldsymbol{k}) = \phi(x,\boldsymbol{k}) = \sum_m e^{im\varphi} \phi_m(x,k^2), \tag{5.3}$$

and performing the angular integrals explicitly. (For details see Appendix A).

Typically, the higher Fourier components will be rather subleading leaving the dominant $m = 0$ term to drive the gluon distribution. In the case of this simplification, the BFKL equation can be written [19, 20, 21]

$$\phi_0(x,k^2) = \phi_0^{(0)}(x,k^2) + \bar{\alpha}_s k^2 \int_x^1 \frac{dz}{z} \int \frac{dk'^2}{k'^2} \left\{ \frac{\phi_0\left(\frac{x}{z},k'^2\right) - \phi_0\left(\frac{x}{z},k^2\right)}{|k^2-k'^2|} + \frac{\phi_0\left(\frac{x}{z},k^2\right)}{(4k'^4+k^4)^{1/2}} \right\} \quad (5.4)$$

We note that the IR divergence as $k \to k'$, corresponding to the transverse momenta of the emitted gluon, $q \to 0$, is regulated by an explicit cancellation between terms whose origins lie in real and virtual gluon emission. Moreover the integral kernel is conformally invariant, that is $k \to \lambda k$ leaves the equation's form unaltered, and allows an analytic solution to be effected through the ubiquitous Mellin transforms, as before. However, unlike the previous DGLAP case, the BFKL equation requires a transformation in both x and k^2 variables, in order to completely diagonalize it.

5.3 Skeleton solution of the leading log BFKL equation

In later sections higher order corrections to the leading logarithmic BFKL equation are discussed, and a modified form, more readily suited for phenomenological analysis is motivated. We will see in detail in Appendix A how the solution of this modified equation proceeds, for the case of a fixed $\bar{\alpha}_s$, and is a generalization of the asymptotic solution of the leading logarithmic scenario. In anticipation of this, we present a cursory sketch of the solution of Eqn. (5.4) whose gross features we will later contrast with those of the modified version.

We are able to exploit the conformal nature of the BFKL equation, in an analagous manner to the DGLAP solution, to undo the coupled convolution. We apply the following Mellin transforms, extending the machinery of Eqn. (4.18),

$$\tilde{\phi}(x,\varrho) = \int_0^\infty \frac{dk^2}{k^2} \left(\frac{k^2}{Q_0^2}\right)^{-\varrho} \phi(x,k^2), \quad \text{and} \quad \hat{\phi}(\omega,\varrho) = \int_0^1 \frac{dx}{x} x^\omega \tilde{\phi}(x,\varrho), \quad (5.5)$$

where Q_0^2 is an arbitrary scale, and ω and ϱ are the conjugate variables to x and k^2 respectively, in Mellin space. The BFKL equation simplifies quite dramatically into a readily tractable form:

$$\hat{\phi}(\omega,\varrho) = \frac{\omega\, \hat{\phi_0}^{(0)}(\omega,\varrho)}{\omega - \bar{\alpha}_s \mathcal{K}^{\mathrm{LL}}(\varrho)} \quad (5.6)$$

with $\mathcal{K}^{\rm LL}(\varrho)$ the famous BFKL kernel function,

$$\mathcal{K}^{\rm LL}(\varrho) = 2\psi(1) - \psi(\varrho) - \psi(1-\varrho), \tag{5.7}$$

where ψ is the logarithmic derivative of the Euler-Γ function, with an integral representation

$$\psi(z) = \frac{d}{dz}\log\Gamma(z) = -\gamma - \int_0^1 d\nu \frac{\nu^{z-1}-1}{1-\nu}. \tag{5.8}$$

Notice the kernel is symmetric under $\varrho \to 1-\varrho$, which connects the large and small transverse momentum behaviour of the unintegrated gluon distribution. It is a consequence of the symmetry under exchange of the two transverse momentum scales, from the first of the definitions of the Mellin transforms, Eqns. (5.5),

$$\frac{1}{k^2}\left(\frac{k^2}{Q_0^2}\right)^{\varrho} = \frac{1}{Q_0^2}\left(\frac{Q_0^2}{k^2}\right)^{1-\varrho}.$$

We can transform the solution back from the complex (ω, ϱ) plane using the inverse transformations to Eqns. (5.5), given respectively by:

$$\phi_m(x,k^2) = \oint_{C-i\infty}^{C+i\infty} \frac{d\varrho}{2\pi i}\left(\frac{k^2}{Q_0^2}\right)^{\varrho} \tilde{\phi}_m(x,\varrho) \text{ and } \tilde{\phi}_m(x,\varrho) = \oint_{C-i\infty}^{C+i\infty} \frac{d\omega}{2\pi i} x^{-\omega}\hat{\phi_m}(\omega,\varrho). \tag{5.9}$$

Typically, the input distribution $\phi^{(0)}$, will not contribute to the pole structure in ϱ, and so we have only a single simple pole, $\omega = \bar{\alpha}_{\rm s}\mathcal{K}(\varrho)$, to which we can readily apply the Residue theorem to evaluate $\hat{\phi}_0(x,\varrho)$. Furthermore, an approximation to the full solution in (x,k^2) space can then be calculated by noting the symmetry in the kernel and performing a saddle point integral along the contour $\nu = 1/2 + i\varrho$. We illustrate the structure of the leading logarithmic BFKL kernel in the complex ρ plane in Fig. 5.3, along with the appropriate choice of contour for the saddle point integration. The kernel achieves its maximal value, $\mathcal{K}_0^{\rm LL}(\varrho = 1/2) = 4\log 2$, along this path, and dies away sufficiently rapidly for the leading contribution to the integral to be obtained from around $\nu \sim 0$. We finally obtain (including the diffusive factor in transverse momenta) a form for the dimensionless unintegrated gluon distribution,

$$\phi(x,k^2) = \frac{\left(\frac{x}{x_0}\right)^{\omega_0^{\rm LL}}\tilde{\phi}_0(x_0,1/2)}{\left[2\pi\left([\log\tilde{\phi}]''|_{\nu=0} + \bar{\alpha}_{\rm s}\log(x/x_0)\psi''(1/2)\right)\right]^{1/2}} \exp\left\{\frac{-\left[[\log\tilde{\phi}]'|_{\nu=0} + \log(k^2/Q_0^2)\right]^2}{2\left[[\log\tilde{\phi}]''|_{\nu=0} + \bar{\alpha}_{\rm s}\log(x/x_0)\psi''(1/2)\right]}\right\} \tag{5.10}$$

as the celebrated asymptotic solution to the leading logarithmic BFKL equation. The exponent of the evolution length (x/x_0) is given by $\omega_0^{\rm LL} = -\bar{\alpha}_{\rm s}4\log 2 \simeq -0.5$, and $\bar{\alpha}_{\rm s}\psi''(1/2) = \bar{\alpha}_{\rm s}28\zeta(3) \simeq 6.4$, where we have used a typical value of $\alpha_{\rm s} \simeq 0.2$ to quantify the defining parameters.

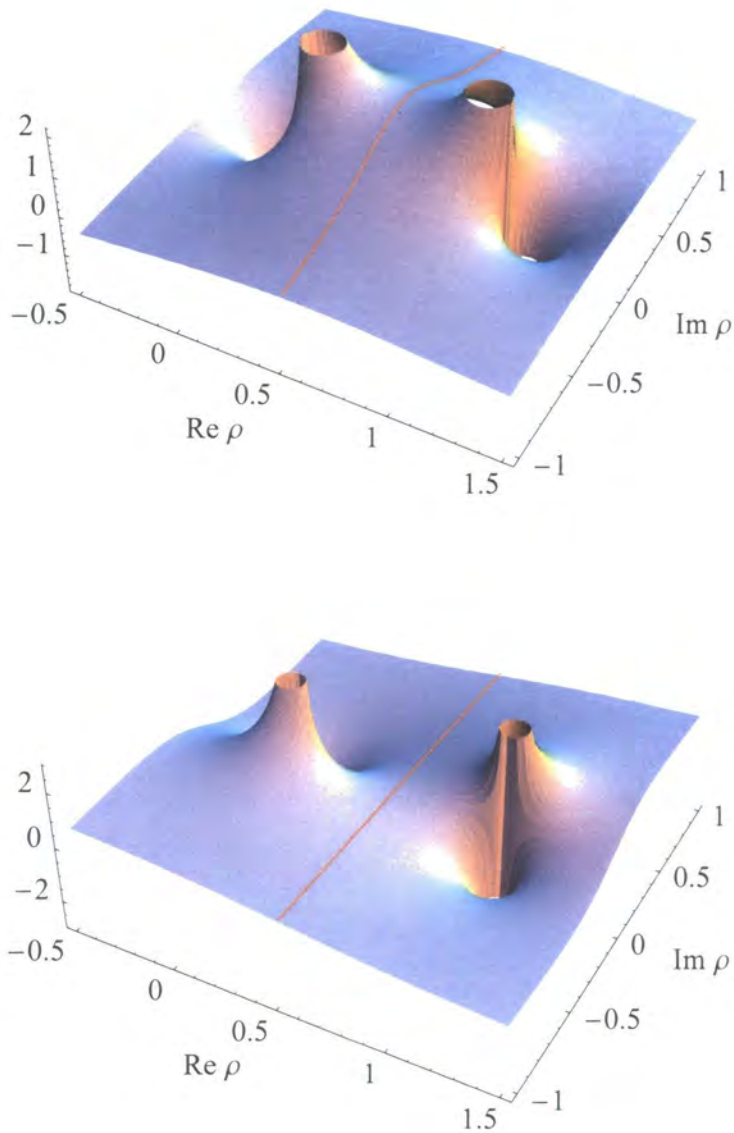

Figure 5.3: Structure of the LL BFKL function determining the leading eigenvalue, $\bar{\alpha}_s \mathcal{K}_0^{\rm LL}(\varrho)$, in the complex ϱ plane. The uppermost plot illustrates $\bar{\alpha}_s {\rm Re}\, \mathcal{K}_0^{\rm LL}(\varrho)$, whilst beneath $\bar{\alpha}_s {\rm Im}\, \mathcal{K}_0^{\rm LL}(\varrho)$ is shown. Note the saddle point structure at $\varrho = 1/2$, the contour of integration, ${\rm Re}\, \varrho = 1/2$, is marked in red.

5.3.1 Qualitative properties of the leading BFKL gluon distribution

Using the asymptotic solution presented in the previous section we can broadly discuss the types of features that typify BFKL dynamical effects. In a kinematic regime where the BFKL formalism is appropriate, we should expect to see rather stark characteristic behaviour of the unintegrated gluon distribution, distinct from that arising from DGLAP evolution, which will propagate through to observable quantities via k_T-factorization[3]. We anticipate a strong rise in cross-sections governed by BFKL-type behaviour with increasing centre of mass energy, $s \sim 1/x$. In the following chapter we examine some phenomenological processes which might best allow us to isolate a BFKL dynamics 'smoking gun', but for now we proceed with a more qualitative discussion of its chief distinguishing features.

The most striking of BFKL signatures is the singular behaviour of the unintegrated gluon distribution, $f(x,k^2) \sim x^{\omega_0^{\rm LL}}$, as $x \to 0$. This leads to a swift growth for the gluon distribution $g(x,Q^2) \sim x^{\lambda_{\rm BFKL}}$, with $\lambda_{\rm BFKL} = 1 - \omega_0^{\rm LL} \simeq 3/2$ for $\alpha_{\rm s} \simeq 0.2$, a rise which is to be compared with that obtained from the DLLA gluon distribution Eqn. (4.21). It is inconclusive as yet as to whether BFKL dynamics are necessary to describe the observed rise in small x observables. The freedom to select suitable input forms means the DLLA approximation can adequately describe the features of many inclusive quantities. Subsequent chapters will tackle phenomenology specifically tailored to highlight small x dynamics, whilst precluding the development of evolution in Q^2.

The second notable feature of the analytic BFKL solution is that there exists a diffusive component to the unintegrated gluon distribution, corresponding to the exponential term in Eqn. (5.10). This has the form of a Gaussian of width $2\left[[\log\tilde{\phi}]''|_{\nu=0} + \bar{\alpha}_{\rm s}\log(x/x_0)\psi''(1/2)\right]$, and whose maximum is predetermined by the boundary condition set by the quantity $\left[\log\tilde{\phi}\right]'|_{\nu=0}$ and implies that we see a diffusion in $\log k^2$ as we evolve towards lower x. In principle the integral in k^2 can now penetrate into the IR region where we have no quantitative description of the physics mechanisms in play. An ad hoc cut off is usually introduced in the transverse momentum integral [23, 24] to prevent this incursion into the IR region, but this carries with it

[3] k_T-factorization essentially says that observable quantities in a perturbative expansion are obtained through a convolution in both longitudinal and transverse momenta

an associated dependence on a new computational artifact, k_0^2, which will need investigation.

5.4 Beyond the leading logarithm

The leading logarithmic BFKL formalism has some readily apparent deficiencies. Foremost of these is the fact that the equation does not conserve energy-momentum, a consideration that is technically subleading in the LL BFKL picture. The fact that this most physical of requirements, associated with multi-gluon emission, is not strictly adhered to ought to be troubling if we hope to accurately describe real processes in high energy colliders, which certainly *do* subscribe to energy-momentum conservation. In Monte-Carlo implementations [25] of the LL BFKL equation it is possible to impose this requirement explicitly by hand. It has been illustrated that the imposition of energy-momentum conservation on the leading log BFKL equation yields a gluon distribution which exhibits a non-negligible effect on small x observables, with the chief effect seen to be a suppression of the gluon density in the small x region.

A further important consideration is the running of the strong coupling [26], α_s - we have analysed the BFKL equation in a scheme of fixed α_s, for computational elegance, in order to elicit the characteristic behaviour of the solutions. The scale of the strong coupling is not determined at the LL level, and so we have a normalization ambiguity from whatever selection of typical (fixed) scale we decide to make. We should acknowledge that by including a full running coupling the detailed behaviour of the unintegrated gluon in the small x regime may shift. Qualitatively, running α_s will tend to shift the distribution towards the lower values of $\mu_R^2 \simeq k^2$, as we weight the integral in transverse momentum in Eqn. (5.4) towards the IR.

That the LL BFKL formalism is not a complete description of the small x dynamics is evinced by reference to the Froissart-Martin bound. From quite general unitarity considerations, it can be shown that asymptotically the total hadronic cross-section is constrained from above by $\sigma_{\text{tot}} \leq \log^2 s$. Yet in the preceding BFKL formalism we have seen a total hadronic cross-section that posseses a power law behaviour, $\sigma_{\text{tot}} \sim s^{\lambda}$! At some point the Froissart-Martin bound is breached, and it is apparent that there must exist subleading corrections which act in concert to eventually tame this singular behaviour and restore compliance with unitarity.

In the following sections we will briefly discuss the ramifications of the explicit NLL BFKL calculations and subsequently motivate higher order corrections to the LL BFKL equation which can be included to *all orders*, and compare and contrast the effect of their inclusion with the explicit NLL case.

5.4.1 Formally next-to-leading log corrections

The full formal next-to-leading log corrections[4] to the BFKL kernel arise via two distinct classes of mechanism. We relax the strong ordering in longitudinal momenta, x, along the real gluon emission chain, in such a way that two gluons in the cascade can have similar momentum fractions. This will generate one less factor of $\log(1/x)$ relative to the case of strictly strong ordering in x of the kinematic phase space that we demand for the leading log BFKL scenario. We must also admit the possibility of more complicated virtual interactions. The effective BFKL vertex should now contain one loop QCD corrections, and we must also include other virtual corrections which contribute to the NLL reggiezation of the exchanged gluon.

The next-to-leading log corrections were computed explicitly over the period of the past decade by a variety of authors [27, 28, 29], and to the surprise and consternation of the high energy physics community, resulted in large and negative corrections to the LL kernel function. The calculations of the maximum eigenvalue of the BFKL kernel at next-to leading order yielded the following result [30], at the point $\varrho = 1/2$, in the $\overline{\text{MS}}$ scheme:

$$\lambda_{\text{NLL}} = \lambda_{\text{LL}}[1 - 6.5\bar{\alpha}_{\text{s}}], \tag{5.11}$$

where $\lambda_{\text{LL}} = \bar{\alpha}_{\text{s}} 4 \log 2$ denotes the maximum eigenvalue of the leading log BFKL kernel. Note the final coefficient contains a weak dependence on the number of active flavours, n_f.

This is an extremely large correction for a typical value of the strong coupling, $\alpha_{\text{s}} \simeq 0.2$, corresponding to characteristic exponents of $\lambda_{\text{LL}} \simeq 0.5$ and $\lambda_{\text{NLL}} \simeq -0.12$. This result appears indicative of the apparent instability of the series, which is clearly unpalatable - the NLL corrections per se seem to suggest that phenomenology based around the leading log BFKL formalism is at best somewhat naive, and at worst actually misleading.

[4] NLL corrections resum terms of a type $\alpha_{\text{s}}[\alpha_{\text{s}} \log(1/x)]^r$ in addition to the LL terms $[\alpha_{\text{s}} \log(1/x)]^r$.

We should naturally question the convergence of the resummation program and correspondingly reevaluate the reliability of its phenomenological applications. Do we need the NNLL corrections in order to calculate observables with the assurance of stability? The NLL corrections were a truly prodigious computational task, and further levels of sophistication in the BFKL formalism appears impractical, simply in terms of computational time. The lesson is clear - we should try to address alternative methods of stabilizing the small x resummation.

5.5 The consistency constraint

In the previous section we discussed the ways in which the LL BFKL resummation is considered an incomplete physical description, and illustrated that the inclusion of NLL corrections pose more questions than they resolve. In light of the magnitude of the negative shift of the NLL corrections, which cloud the quantitative predicitive ability of a standard LL or NLL BFKL approach to phenomenology, we require some technique to resum, at all orders, the higher order corrections. Unfortunately, such a method does not currently, and is not likely, in the near future, to exist. For phenomenological applications, however progress can be made by resumming *dominant* portions of the higher order corrections.

One such method for incorporating higher order effects is granted by implementing the so-called *consistency constraint* [31]. Briefly put, this is the formally subleading requirement that the virtuality of the exchanged gluons along the evolution chain should arise predominantly from their transverse components of momentum, expressed in its most primitive form [31], see Fig. 5.4,

$$|k'|^2 \simeq k_T'^2. \tag{5.12}$$

This requirement ensures that the small x approximation, applied in the derivation of the BFKL equation remains strictly in place throughout.

With a little manipulation the constraint can be most succinctly formulated for its inclusion within the BFKL equation by

$$q_T^2 < \frac{1-z}{z} k_T^2 \quad \sim \quad q_T^2 < \frac{k_T^2}{z}, \tag{5.13}$$

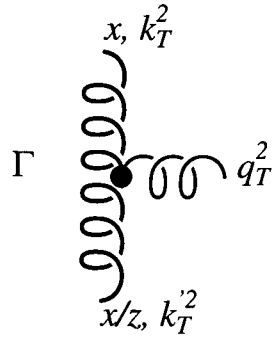

Figure 5.4: The consistency constraint: the transverse momentum of a reggeized t-channel gluon, $k_T'^2$, is restricted via Eqn. (5.12). x and x/z refer to the fractions of the proton's longitudinal momentum carried by the exchanged gluon. k_T^2, $k_T'^2$ and q_T^2 correspond to the square of the transverse momentum of the exchanged and emitted gluons respectively.

where q_T^2 is the transverse momentum squared of the emitted gluon, and z is the longitudinal momentum fraction, see Fig. (5.4). The constraint acts as longitudinal momentum fraction dependent upper bound on the transverse momentum integration of Eqn. (5.4), which manifests itself in a dependence of the Mellin transformed BFKL kernel on the conjugate variables of *both* longitudinal and transverse momenta, see Appendix A.

A second crucial physical source of sub-leading contributions arises from the imposition of energy-momentum conservation in multi-gluon emission, which was studied in [32]. For a gluon emitted along a BFKL-type evolution chain we require for the subprocess $\hat{s} = (q + k')^2 > 0$, with q now the four-momentum of the photon probing the system. In the very high energy limit where the BFKL equation is applicable, we have [31]

$$k_T'^2 < \frac{k_T^2}{z} \lesssim \frac{Q^2}{x}.$$

Where the weaker piece of the (approximate) relation is demanded by energy-momentum conservation, and the more stringent part is required by the consistency constraint, Eqn. (5.13), in the small x domain, $Q^2 \simeq k_T^2$ and $z \ll x$. The energy-momentum restrictions are *pinned* by those imposed by the consistency constraint in the areas of the (x, Q^2) kinematic plane that provide the dominant contributions. The consistency constraint can be said to subsume explicit energy-momentum conservation over a broad region of the allowed phase space.

One further compelling feature of the consistency constraint is that it preserves the scale invariance we witnessed in the LL BFKL equation. As this still holds, we can utilize the well-known Mellin transforms of the asymptotic LL solution in order to quantify the effect of its imposition, which we discuss in the subsequent section, and address fully in Appendix A.

A final comment is that the dual inclusion of a running coupling and the consistency constraint is expected to tend to dilute the effect of the latter's inclusion. The integrand in Eqn.(5.14) will be weighted by $\alpha_s(k_T'^2)$ more heavily away from larger values of $k_T'^2$, where the constraint becomes active.

5.6 The modified BFKL equation

As was discussed previously the consistency constraint places restrictions on the available phase-space under the integration in the BFKL equation. Constructed in the form given in Eqn. (5.13), this manifests itself as a Θ-function multiplying the LL BFKL kernel component governing real gluon emissions [31]. We can simply implement this, maintaining the valuable scale invariance of the LL BFKL equation to obtain a modified BFKL equation whose solution will exhibit properties we hope will be better suited to phenomenology. The modified equation is written:

$$f(x,\boldsymbol{k}) = f^{(0)}(x,\boldsymbol{k}) + \bar{\alpha}_s \int_x^1 \frac{dz}{z} \int \frac{d^2\boldsymbol{q}}{\pi q^2} \left\{ f(\frac{x}{z}, \boldsymbol{k}+\boldsymbol{q})\, \Theta\left(\frac{k^2}{q^2+k^2} - z\right) - \frac{k^2}{q^2+(\boldsymbol{k}+\boldsymbol{q})^2} f(\frac{x}{z}, \boldsymbol{k}) \right\}, \tag{5.14}$$

which in the case of a fixed coupling $\bar{\alpha}_s$ we treat analytically in appendix A. We note that the cancellation as $\boldsymbol{q} \longrightarrow \boldsymbol{0}$ between terms arising from real and virtual gluon emission is unaffected, as, reiterating, the consistency constraint affects only the upper limit of the inner integration. This is the form of the BFKL equation that we will exclusively deal with in later chapters of this thesis.

5.6.1 Modified BFKL kernel structure

We saw before how the behaviour of the leading BFKL equation is determined by the pole structure of the kernel function $\mathcal{K}^{\mathrm{LL}}(\varrho)$. The consistency constraint has the effect of entangling

further the z and $\boldsymbol{q}$ integrations which force an ω dependence (the conjugate variable to z) on the modified kernel function $\mathcal{K}^{\mathrm{CC}}(\omega, \varrho)$. We find

$$\mathcal{K}_m^{\mathrm{CC}}(\omega, \varrho) = 2\psi(1) - \psi(m/2 + \varrho) - \psi(m/2 + \omega - \varrho + 1). \tag{5.15}$$

In order to invert the Mellin transforms we wish to perform an integration through the Residue theorem, and we must find poles in ω, which correspond to zeros of the implicit equation

$$\omega(\varrho) = \bar{\alpha}_{\mathrm{s}} \mathcal{K}_m^{\mathrm{CC}}(\omega(\varrho), \varrho). \tag{5.16}$$

In an analagous way to the leading kernel having a saddle point at $\varrho = 1/2$, the modified kernel will achieve its maximal value along the contour defined implicitly by $\varrho = (\omega(\varrho) + 1)/2$.

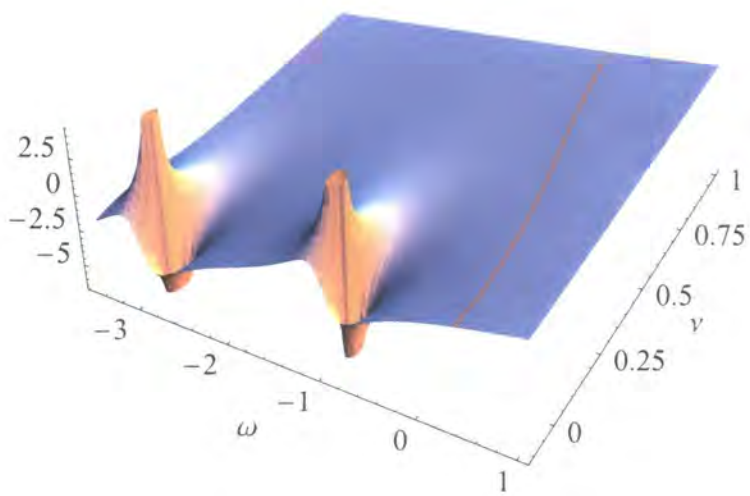

Figure 5.5: Structure of the surface $\omega - \bar{\alpha}_{\mathrm{s}} \mathcal{K}_0^{\mathrm{CC}}(\omega, \nu)$, for $\bar{\alpha}_{\mathrm{s}} = 0.2$. The intersection of this surface and the $z(\omega, \nu) = 0$ plane gives the poles, $\omega_0^i(\nu) = \bar{\alpha}_{\mathrm{s}} \mathcal{K}_0^{\mathrm{CC}}(\omega_0^i(\nu), \nu)$, corresponding to the solution of the modified BFKL equation in Mellin transform space for real values of ω and ν. Superimposed on the surface in red is the leading singularity, $\omega_0^0(\nu) = \bar{\alpha}_{\mathrm{s}} \mathcal{K}_0^{\mathrm{CC}}(\omega_0^0(\nu), \nu)$.

We anticipate performing a saddle point integration along this contour to determine the leading behaviour of the solution to the modified BFKL equation, and to this end, make the modified kernel transparently symmetric through the shift in variables, $\varrho = (\omega + 1)/2 + i\nu$, to

obtain

$$\mathcal{K}_m^{\rm CC}(\omega,\nu) = 2\psi(1) - \psi(\frac{m+\omega+1}{2} + i\nu) - \psi(\frac{m+\omega+1}{2} - i\nu). \tag{5.17}$$

It should be noted that the single simple pole we obtained in the ω plane in the leading logarithmic BFKL approximation has been superseded by a far richer pole structure, illustrated in Fig. (5.6.1). We now obtain a series of poles, each a solution of the equation $\omega_m^i(\nu) = \bar{\alpha}_{\rm s}\mathcal{K}_m^{\rm CC}(\omega_m^i(\nu),\nu)$, and in principle requiring inclusion in the sum over poles in the residue theorem. However, the leading pole is the only one contributing a significant exponent in x, and we anticipate that the inclusion of the subleading poles in expressions for the unintegrated gluon distribution is not great, and that to a good approximation their contributions can be neglected. The subleading poles are paired and each pair lie successive units of $\Delta\omega \sim 1$ beneath one another.

5.6.2 Comparative behaviour of the modified BFKL exponent

Through the asymptotic solutions we have seen how the extent of the BFKL type behaviour is determined by the characteristic Lipatov exponent. In this subsection we compare the relative strengths of this power for four variants of the BFKL solution: the LL approximation, the NLL approximation, the LL with consistency constraint imposed and the LL with consistency constraint imposed but truncated at $\mathcal{O}(\alpha_{\rm s}^2)$.

We have shown in the appendix that for small x the unintegrated gluon distribution is driven by the relevant characteristic exponent. It is an informative exercise to truncate the perform a series expansion of the CC exponent, truncate it to NLL, $\mathcal{O}(\alpha_{\rm s}^2)$, and compare the resulting quantity with the exact NLL exponent. This will tell us qualitatively the extent to which the formal NLL higher order corrections to the LL BFKL are implicitly contained within the physical requirement of the consistency constraint.

We consider the phenomenologically dominant $m = 0$ term and, for ease of notation, throughout the following we suppress both sub and superscripts, and write $\omega_0^0(0) = \omega$, aware of the implicit dependence on $\bar{\alpha}_{\rm s}$ of ω. The expansion reads, keeping only the next-to-leading term,

$$\omega \simeq \omega|_{\bar{\alpha}_{\rm s}=0} + \bar{\alpha}_{\rm s}\left.\frac{\partial\omega}{\partial\bar{\alpha}_{\rm s}}\right|_{\bar{\alpha}_{\rm s}=0} + \frac{\bar{\alpha}_{\rm s}^2}{2}\left.\frac{\partial^2\omega}{\partial^2\bar{\alpha}_{\rm s}}\right|_{\bar{\alpha}_{\rm s}=0}.$$

Eqn. (5.17) implies an implicit equation for ω, from which we can determine the pertinent coefficients

$$\begin{aligned}
\omega|_{\bar{\alpha}_s=0} &= 0 \\
\left.\frac{\partial\omega}{\partial\bar{\alpha}_s}\right|_{\bar{\alpha}_s=0} &= 2\psi(1) - 2\psi(1/2) = \bar{\alpha}_s 4\log 2 \\
\left.\frac{\partial^2\omega}{\partial^2\bar{\alpha}_s}\right|_{\bar{\alpha}_s=0} &= -2\psi'(1/2)\left.\frac{\partial\omega}{\partial\bar{\alpha}_s}\right|_{\bar{\alpha}_s=0} = \bar{\alpha}_s 4\log 2\psi'(1/2)
\end{aligned}$$

In contrast with the explicit NLL solution of Eqn. (5.11) we obtain the following form for the truncated all orders consistency constraint solution:

$$\lambda_{\text{trunc}} = \lambda_{\text{LL}}\left[1 - \frac{\pi^2}{2}\bar{\alpha}_s\right]. \tag{5.18}$$

Comparing the $\mathcal{O}(\alpha_s^2)$ coefficients of Eqns. (5.11) and (5.18), it appears that we exhaust some 75% of the explicit NLL corrections. This figure should give us some confidence that our formalism is indeed incorporating the dominant higher order effects.

The characteristic exponents of the four approximations are plotted with one another in Fig. (5.6.2). The first thing to notice is that even for rather small values of α_s, higher order

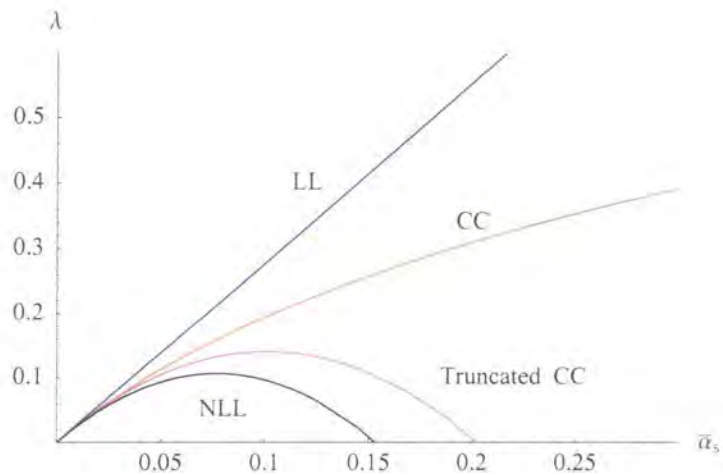

Figure 5.6: Comparison of the exponents, λ, of the power law behaviour of $x^{-\lambda}$ of the gluon distribution, obtained in (blue) the leading log and (black) the next-to-leading log approximation. The red curve is generated by imposing the consistency constraint on the LL BFKL equation. and the magenta curve corresponds to that same solution truncated to NLL.

corrections are crucial. Even at $\alpha_s \simeq 0.1$, the exponents vary between ~ 0.1 and ~ 0.3, and this spectrum diverges rapidly as α_s increases. Indeed for larger (but still perturbative) values of α_s, the exponent switches sign! It is apparent that the LL BFKL exponent dramatically overestimates the strength of the singular behaviour, and that the exact NLL exponent strongly underestimates the growth.

The all order resummation contained within the consistency constrained exponent lies comfortably between these two extreme bounds of behaviour, which is reassuring if we expect to model genuine physics.

In Fig. 5.7 the functions $\omega_m(\nu)$ are plotted for the first few eigenvalues of the azimuthal components of both LL and CC BFKL kernels. There is a clear suppression for the $m = 0$ solution of the consistency constraint eigenvalues in comparison with those of the leading logarithm solution in the dominant region of ν. As well as the leading azimuthal component, we can also examine the higher coefficients. We see that the effect of imposing the consistency constraint on these is somewhat lessened with increasing m. This is to be anticipated, as the (typically small) values of ω appearing in the arguments of the ψ-functions of Eqn. (5.17) are overwhelmed by the increasing m of the azimuthal projection. This will mean that the higher azimuthal projections have a comparatively more significant effect in the consistency constraint formalism than that of the LL. Correspondingly, the CC formalism will exhibit stronger azimuthal dependence than that of the leading log.

5.7 A small x caveat, unitarity constraints

Recall that we mentioned in passing that the singular behaviour predicted by the summation of logarithms of x in the small x domain could not go unchecked indefinitely by reference to the Froissart-Martin bound. Eventually we enter a kinematic regime so extreme that we can no longer treat the partons within the proton as isolated, their number density becomes such that spectator partons are no longer passive and can act as a screening agent. The partonic density is such that gluons *recombine* within the proton [22, 33]. These processes are described by additional multi-ladder diagrams which at very high energies will provide the required suppression,

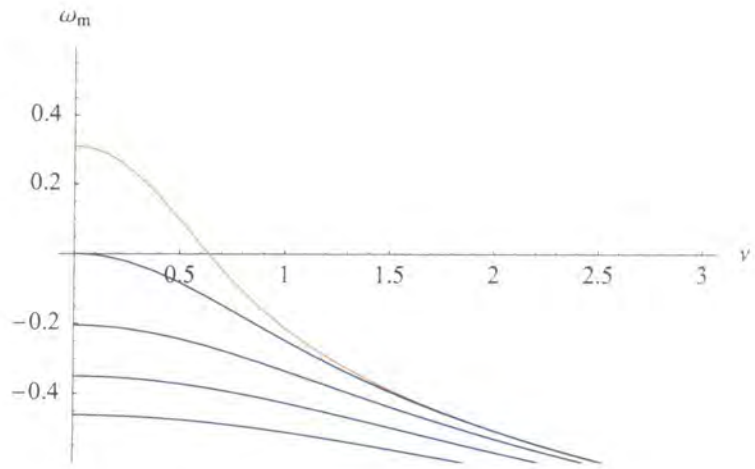

Modified BFKL exponent, $\bar{\alpha}_s = 0.2$.

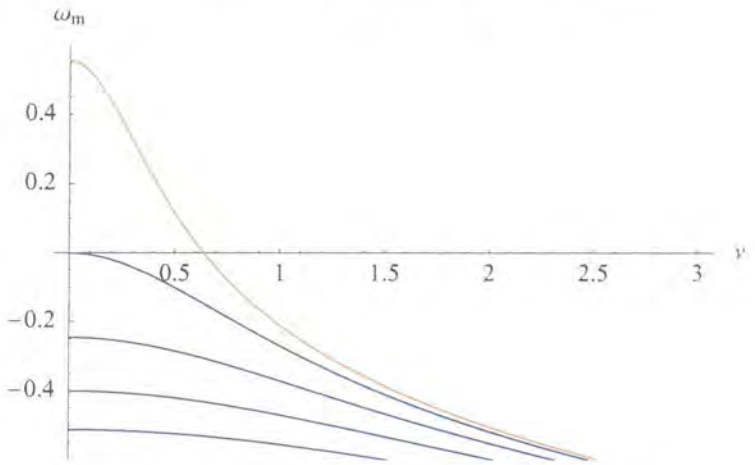

Leading logarithmic BFKL exponent, $\bar{\alpha}_s = 0.2$.

Figure 5.7: The functions $\omega_m(\nu)$, $m = 0, 1, 2, 3, 4$, corresponding to the first five azimuthal projections of the characteristic exponents of the solutions to the BFKL equations. The dominant $m = 0$ function is shown in red. Above are shown the solutions corresponding to the BFKL equation with consistency constraint imposed, and below the strictly LL approximation. Observables sensitive to the angular behaviour of the small x gluon and thus the relative magnitudes of the $m = 0$ and $m > 0$ azimuthal projections might provide a further test of the validity of the consistency constraint.

they add a non-linear term to the BFKL equations which at very small x acts to damp the singular behaviour and thus saturate the proton. Detailed numerical studies [33] suggest that these effects are not required in the kinematic regime currently accessible to HERA.

Chapter 6

BFKL phenomenology at HERA

In this chapter we examine certain DIS processes that in principle afford a clean view of BFKL-type dynamics in vivo. In particular, we examine how exclusive measurements of the final state eliminate theoretical and experimental ambiguities that can cloud the interpretation of results as we enter the small x regime. We calculate the DIS + forward jet cross-section, subject to those higher order effects whose origin and effects were detailed in the previous chapter, and compare these predictions with data from the H1 and ZEUS collaborations at HERA. We then motivate a further refinement to the forward jet process, that of DIS + forward π^0, and again compare theoretical calculations to recent experimental distributions from the H1 collaboration. We will also identify and quantify certain residual uncertainties that arise within the framework of the theoretical analysis. We end with a brief discussion of a contrasting alternative mechanism for generating forward jets, the resolved photon.

6.1 Inclusive measurements and the Mueller proposal

In the previous chapter we saw how, in specific high energy regimes, terms of the type $[\alpha_s \log(1/x)]^r$ come to dominate a perturbative expansion and require a prescription for their resummation, leading naturally to a quite distinct small x behaviour. The challenge faced by the high energy physics community is to unambiguously identify characteristic features, principle amongst

them the inverse power law $x^{-\lambda}$ behaviour of the unintegrated gluon distribution at small x, in reactions occurring at particle colliders, such as the facility at HERA.

Theoretically, we anticipate that the strong steepening as $x \to 0$ will feed through into observable quantities through the k_T-factorization theorem [34]. As the full extent of the (x, Q^2) plane that can be probed at the HERA facility has dramatically broadened [1] during recent years, it was expected that a clear signal for BFKL dynamics might be observed. However, in observables as inclusive as $F_2(x, Q^2)$, the proton structure function, it is problematic to cleanly disentangle small x effects from those dynamics which might arise from the double logarithmic resummation of terms of the type $[\alpha_s \log(Q^2/Q_0^2) \log(1/x)]^r$ in the more conventional small x limit of DGLAP evolution. Recall, (4.21), that these also predict an increase in the gluon distribution with decreasing x,

$$xg(x, Q^2) \simeq \exp\left(2\left[\bar{\alpha}_s \log\left(\frac{1}{x}\right) \log\left(\frac{Q^2}{Q_0^2}\right)\right]^{\frac{1}{2}}\right),$$

although comparatively less steep than that required by BFKL dynamics.

It transpires that although a clear rise with decreasing x in F_2 is evident in the experimental data from HERA [35], it can be adequately described by the next-to-leading DGLAP evolution, as well as BFKL dynamics[2]. We can tune the DLLA description of the gluon distribution in such a way as to build in the observed rise of F_2 at small x. We are at liberty to alter the choice of evolution length, $\log(Q^2/Q_0^2)$, by decreasing Q_0^2, which will enhance the increase of the DLLA gluon distribution. Alternatively, we can impose a singular form for the initial input distribution $xg(x, Q_0^2)$, which, fit to data, will (trivially) ensure singular behaviour in the final, evolved distribution. The available freedom in the choice of initial conditions erodes completely our capacity to discriminate theoretically between the pQCD evolution modes that might arise.

Approaching from the BFKL standpoint we will also encounter subtleties that tend to render any inclusive approach to small x physics at least ambiguous. The lack of ordering in transverse momentum along the evolution cascade results in a random walk of the emitted gluon momentum, encapsulated by the gaussian structure in k_T^2 of the solution to the BFKL equation,

[1] Currently, $F_2^P(x, Q^2)$ is accessible at HERA down to values of $x \simeq 10^{-5}$ and reaching up to $Q^2 \simeq 10^4$ GeV^2.

[2] A quantitative analysis of the structure function F_2 within a unified DGLAP and consistency constraint supplemented BFKL scheme was studied in [36]

Eqn. (5.10). This diffusion implicitly permits an infiltration of the infrared region of transverse momentum, 1 GeV$^2 \lesssim k_T^2$, by the emitted gluons, and we can thus collect non-perturbative contributions that we de facto have no formal description of.

One resolution to these deficiencies in the choice of F_2 as an observable has been known for some time. Mueller in 1991 [37] appreciated that the chief problem lay in the fact that F_2 is rather too inclusive an observable quantity to allow truly discriminatory testing. He proposed that were we to consider a more exclusive final state, in a very specific kinematic configuration, then the problems highlighted above could be to a greater extent alleviated. Specifically, Mueller suggested that the measurement of an identified jet of hadrons, distinct from the current jet, and in a very forward region relative to the proton direction, would be a choice process to study in order to isolate BFKL dynamics:

$$\gamma^* + P \rightarrow \text{jet} + X.$$

This process is of paramount interest on the grounds that the kinematic configuration of these jet events minimizes opportunity for DGLAP-type evolution whilst maximizing BFKL-type evolution, and moreover, they at the same time possess secondary characteristics which circumvent some of the subtler difficulties discussed above. We show a schematic diagram for a sample Mueller event in Fig. 6.1.

The DGLAP evolution length is approximately nullified, $\log(k_{jT}^2/Q^2) \simeq 0$, by the insistence that the jet's transverse momentum, k_{jT}^2, is of the same order as the virtuality of the probing photon - we only sample that subset of DIS events which allows us to isolate those containing the small x dynamics of interest. A corollary to this requirement is that we deny the emitted transverse momentum along the chain access to the the non-perturbative infrared region through the diffusion mechanism. By pinning the transverse momentum at substantial $Q^2 \simeq k_{jT}^2$ at either end of the evolution, the gaussian is unable to appreciably penetrate so low in k_{jT}^2 that the use of perturbative techniques is invalidated.

We secondly restrict ourselves to only those jets carrying away a significant fraction of the proton's longitudinal momentum, x_j^p. This corresponds to the most favourable conditions for BFKL dynamics to occur. We try to elongate the BFKL evolution length, $\log(x/x_j^p)$, to provide the strongest possible potential for the appearance of a characteristic signature. A secondary

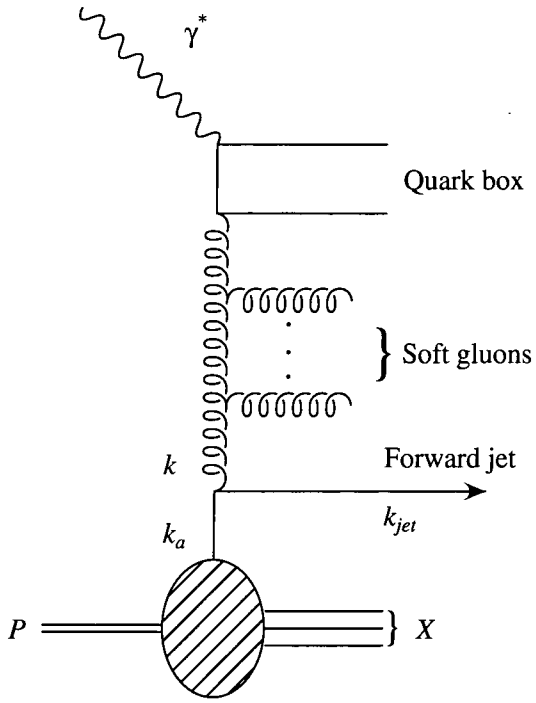

Figure 6.1: Diagram showing forward jet production driven by $\gamma^* g$ fusion coupled to evolution through a BFKL-type ladder. The struck parton, a, ejected from the proton, could in principle be either a gluon or a quark.

advantage to this requirement from the theoretical standpoint is that the deep inelastic scatter occurs from a known parton within the proton. The parton distribution functions are well known at (x_j^p, k_{jT}^2) from global fits and analysis, thus minimizing a further potential source of ambiguity.

6.2 QCD formalism for the production of forward jets in DIS

We now present the QCD framework for describing the production of a forward jet, specified in terms of the longitudinal momentum fraction x_j^p and the transverse momentum $\boldsymbol{k_{jT}}$. The differential cross-section for forward jet production can be written in the following way [38, 39]:

$$\frac{\partial \sigma_j}{\partial x \partial Q^2 \partial x_j^p \partial k_{jT}^2} = \frac{4\pi\alpha^2}{xQ^2}\left((1-y)\frac{\partial F_2}{\partial x_j^p \partial k_{jT}^2} + \frac{1}{2}y^2 \frac{\partial F_T}{\partial x_j^p \partial k_{jT}^2}\right). \tag{6.1}$$

The two differential structure functions, F_T and F_L, parameterise the physics of that subset of DIS events containing an identified jet in the forward region. We use the same DIS nomenclature as was introduced in Chapter 4, where $y = (p \cdot q)/(p_e \cdot q)$ and have defined $F_T = 2xF_1$, and $F_L = F_2 - 2xF_1$, the transverse and longitudinal structure functions.

The strong ordering condition at the jet vertex of Fig. 6.1, $x \ll x_a$, requires that the momentum fractions of the outgoing jet and the struck parton, a, with four-momentum $p_a \simeq x_a p$, are to a good approximation equal, $x_a \simeq x_j^p$. In this situation, the differential structure functions have the following form [24, 37, 38, 39, 40, 41]:

$$\frac{\partial F_i}{\partial x_j^p \partial k_{jT}^2} = \frac{\bar{\alpha}_s}{k_{jT}^4} \left(\sum_a f_{a,P}(x_j^p, k_{jT}^2) \right) \Phi_i \left(\frac{x}{x_j^p}, k_{jT}^2, Q^2 \right), \tag{6.2}$$

where $i = T, L$. The denominator factor k_{jT}^4 of Eqn. (6.2) is a direct consequence of the gluon propagators, the quantities Φ_i are the unintegrated gluon distributions, and the functions $f_{a,P}$ are the parton distribution functions describing the number density for parton species a within the proton.

We find that the scattering that occurs is t-channel pole dominant, that is $|\mathcal{M}|^2 \sim 1/t^2$. In the limit of $t/s \to 0$, the sum over a in brackets of Eqn. (6.2), which describes the proton-parton a subprocess, can be simplifed through the asymptotic relation

$$\sum_a f_{a,P}(x_j^p, k_{jT}^2) = g + \frac{4}{9}(q + \bar{q}),$$

with g the gluon distribution and q and $\bar{q}$ the quark and anti-quark distributions respectively. In the current analysis we allow the index a to run over the light u, d, s quarks, and the heavy c quark, given a mass parameter $m_c = 1.4$ GeV.

The Φ_i contain the information concerning how the gluon distibution couples to the probing virtual photon, in particular it describes the gluonic ladder-like structure seen in the generic associated jet amplitude of Fig. 6.1.

6.2.1 The unintegrated gluon content of virtual photon

In contrast to previous analyses [42], we use a uniform gluon evolution, in the sense that as well as allowing the k_T^2 diffusion from the quark box, the longitudinal momentum fractions are *also*

defined with respect to the photon end of the ladder.

$$x_g^\gamma \ll (x_g^\gamma)_1 \ll ... \ll (x_g^\gamma)_n$$

We now use Eqn. (5.14) to evolve the gluon distribution from the virtual photon end of the evolution chain *down* to the struck parton. The inhomogeneous or driving terms for the modified BFKL equation comprises of the quark box mechanism, which couples the gluon to the virtual photon.

We have invoked strong ordering in the longitudinal momentum at the parton-gluon vertex at the lower end of the chain, and have previously asserted that the struck parton is ejected collinearly to the parent proton, and thus its transverse momentum is negligible:

$$k_{aT}^2 \ll k_{jT}^2.$$

We relate the longitudinal momentum fractions at the jet vertex through the strong ordering and the jet on-shell condition, in the high energy limit where masses are negligible, given by

$$k_{jT}^2 \simeq 0.$$

We make a standard Sudakov decomposition of the four momentum in terms of the light-like momenta p, $q' = q + xp$ and a transverse piece, and are then able to deduce the relations

$$\begin{aligned} 2x_j^p x_j^\gamma (p \cdot q') &= k_{jT}^2 \text{ and} \\ x_g^\gamma \simeq x_j^\gamma &= \frac{k_{jT}^2}{2x_j^p (p \cdot q)} = \frac{k_{jT}^2 x}{Q^2 x_j^p}, \end{aligned}$$

and we can finally determine the unintegrated gluon distribution as it enters the differential cross-section expressed in Eqn. (6.2):

$$\Phi_i\left(\frac{x}{x_j^p}, k_{jT}^2, Q^2\right) = \phi_i\left(x_g^\gamma = \frac{k_{jT}^2 x}{Q^2 x_j^p}, k_{jT}^2, Q^2\right). \tag{6.3}$$

We require the functions ϕ_i to satisfy the modified BFKL equation of Eqn. (5.14), allowing the strong coupling to run and denying access to the infrared part of the $k_T'^2$ integration via a blunt instrument, a crude cut-off in the transverse momentum at the infrared boundary, $k_{jT}^2 > k_0^2$. The small x evolution equation in this case reads:

$$\phi_i(x_g^\gamma, k_{jT}^2, Q^2) = \phi_i^{(0)}(x_g^\gamma, k_{jT}^2, Q^2) + k_{jT}^2 \int_{x_g^\gamma}^1 \frac{dz}{z} \int_{k_0^2}^\infty \frac{dk_T'^2}{k_T'^2} \tag{6.4}$$

$$\bar{\alpha}_s(k_T'^2) \left\{ \frac{\Theta\left(k_T^2/k_{jT}'^2 - z\right) \phi_i(x_g^\gamma/z, k'^2, Q^2) - \phi_i(x_g^\gamma/z, k_{jT}^2, Q^2)}{|k_{jT}^2 - k_T'^2|} + \frac{\phi_i(x_g^\gamma/z, k_{jT}^2, Q^2)}{(4k_T'^4 + k_T^4)^{\frac{1}{2}}} \right\}$$

In summary, this description of the behaviour of the quark box-gluon chain system can be considered as a calculation of the unintegrated gluon content of the photon, γ^*, whose Q^2 dependence is generated dynamically through a perturbative calculation of the inhomogeneous terms, $\phi_i^{(0)}(x_g^\gamma, k_{jT}^2, Q^2)$.

6.2.2 The quark box as inhomogeneous or driving term

The virtual photon gluon fusion process is catalysed by the quark box, [41, 43] appearing at $\mathcal{O}(\alpha\alpha_s)$ by the sum of the box and crossed box diagrams of Fig. 6.2. It is evaluated by making a

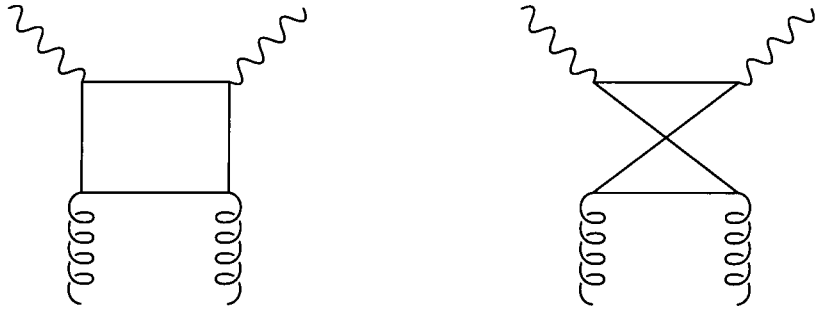

(a) Quark box (b) Crossed box

Figure 6.2: The quark box and crossed box graphs contributing to the inhomogeneous driving terms of the BFKL equation, virtual photon-gluon fusion.

Sudakov expansion of the internal four momenta of the box diagrams in terms of basic light-like quantities, p and $q' = q + xp$ and a transverse momentum vector:

$$\kappa = \alpha p - \beta q' + \boldsymbol{\kappa}$$

$$\begin{aligned}
\phi_T^{(0)}(x_g^\gamma, k_T^2, Q^2) &= \sum_q e_q^2 \frac{\bar{\alpha}_s}{4\pi^2} Q^2 \int_{x_g^\gamma}^1 d\beta \int d^2\boldsymbol{\kappa} \left\{ [\beta^2 + (1-\beta)^2] \left(\frac{\boldsymbol{\kappa}}{D_1} - \frac{\boldsymbol{\kappa} - \boldsymbol{k}}{D_2} \right)^2 + m_q \left(\frac{1}{D_1} - \frac{1}{D_2} \right)^2 \right\}, \\
\phi_L^{(0)}(x_g^\gamma, k_T^2, Q^2) &= \sum_q e_q^2 \frac{\bar{\alpha}_s}{4\pi^2} Q^2 \int_{x_g^\gamma}^1 d\beta \int d^2\boldsymbol{\kappa}\, \beta^2(1-\beta)^2 \left(\frac{1}{D_1} - \frac{1}{D_2} \right)^2,
\end{aligned} \tag{6.5}$$

where the denominator functions, D_1 and D_2 are given by

$$\begin{aligned}
D_1 &= \kappa^2 + \beta(1-\beta)\, Q^2 + m_q^2 \text{ and} \\
D_2 &= (\boldsymbol{\kappa} - \boldsymbol{k})^2 + \beta(1-\beta)\, Q^2 + m_q^2.
\end{aligned}$$

We can readily perform the azimuthal integrations, and the remaining integrations are performed numerically. We take the light quarks as massless, $m_{u,d,s} = 0$, and use a charm quark mass parameter $m_c = 1.4$ in order to enumerate the driving terms.

6.3 Numerical solution of the modified BFKL equation

In order to model the Mueller process as completely as possible we will allow the strong coupling to run with an appropriate hard scale of the order of the transverse momentum of the emitted jet. This qualification invalidates the conformal invariance of the BFKL equation and we must evaluate the unintegrated gluon distribution numerically. In this section we develop the technology necessary to implement this new methodology and discuss explicitly the consequent calculational uncertainties this generates.

6.3.1 Running α_s and Chebyshev polynomials

One other subleading effect that we have yet to take quantitative account of is the running of the coupling α_s, which will weight the unintegrated gluon distributions (6.5) towards smaller values of the scale, usually identified with the transverse momentum of the emitted jet, $\mu_R^2 \sim k_{jT}^2$. This is a potentially significant effect for phenomenological purposes, and ought to be taken into account.

In the expression for the differential cross-section for forward jet production (6.1), we implement a leading order set of parton distribution functions [11]. To be internally consistent we use the leading order expression for the scale dependence of α_s, which reads,

$$\alpha_s(\mu_R^2) = \frac{4\pi}{\beta_0 \log(\mu_R^2/\Lambda_{\rm QCD}^2)},$$

and to match the parameterization of the parton distribution functions we take $\Lambda_{\rm QCD} = 174$ MeV, corresponding to $\alpha_s(M_Z^2) = 0.125$, and β_0 is as given in section 1.4.

The running coupling should be prevented from encroaching into the non-perturbative region, and so ought not to be evaluated beneath $\mu_R^2 \simeq 1$ GeV^2. To this end we impose the crude cut-off,

k_0^2, on the transverse momentum integration of Eqn. (5.14) in order to ensure the infrared is not breached.

The unfortunate cost of the better phenomenological description afforded by implementing a running coupling is that we can no longer solve the BFKL equation analytically as in Appendix A, and must resort to a numerical solution of the unintegrated gluon distribution. Full details are given in Appendix. B, but briefly the unintegrated gluon distribution is approximated using Chebyshev polynomials on a set of node points in the space of longitudinal and transverse momenta, (x, k^2). Discretizing the unintegrated gluon in this manner renders the BFKL equation a problem in (large) matrix inversion, with the matrix entries given by integrations of the kernel function. These integrations can be performed numerically, and the matrix inverted to obtain the solution to the BFKL equation on the Chebyshev nodes, from which the behaviour of the unintegrated gluon can be reconstructed across the kinematic plane.

6.3.2 Residual theoretical uncertainties

We can try to quantify the sensitivity of the calculation to some remaining parametric freedom within the formulation. This arises in two main ways. Firstly, at leading order we have to make a 'sensible' choice for the renormalization scale, μ_R^2, which enters as the argument of the running coupling, $\alpha_s(\mu_R^2)$.

Secondly, the integration over transverse momentum in Eqns. (6.1) and (6.5) in principle runs over the interval $0 \leq k_{jT}^2 < \infty$. This means we clearly breach the infrared region, where the physics is no longer treatable with perturbative methods. The running coupling, with a scale linked to the transverse momentum, blows up at the Landau pole for very small values of k_{jT}^2.

There is in principle an ambiguity arising from choice of the particular set of parton distribution functions used in the analysis. This is not a serious issue in this case, as the functions are evaluated at significant x_j^p where they are well determined. Irrespective of the choice of parameterization, they are so well constrained in this kinematic region as to become indistinguishable.

We define three different calculation 'schemes', (i-iii), corresponding to variations in the scale,

$\mu_R^2 \to \mu_R^2/4$, and infrared cut-off, k_0^2, varying between 1 GeV and 0.5 GeV. For the lower choice of scale, $k_{jT}^2/4$, we *freeze* the coupling beneath $k_{jT}^2/4 = k_0^2$ to avoid its blowing up. The final column refers to the line types of curves in Fig. 6.4 and subsequent comparitive distributions.

(i)	$(k_{jT}^2 + m_q^2)/4$,	$k_{jT}^2/4$,	$k_0^2 = 0.5$ GeV^2,	(blue curve),
(ii)	$(k_{jT}^2 + m_q^2)/4$,	$k_{jT}^2/4$,	$k_0^2 = 1$ GeV^2,	(red curve),
(iii)	$(k_{jT}^2 + m_q^2)$,	k_{jT}^2,	$k_0^2 = 0.5$ GeV^2,	(green curve).

We can test the sensitivity of the calculation to the choice of scale in α_s by comparing the curves (i) and (iii), and the sensitivity to the value chosen for infrared cut-off by contrasting the predictions of (i) and (ii).

6.4 DIS + forward jet, a comparison with HERA data

We now have the machinery in a place to calculate predictions, and confront these with the available experimental results. We compute a variety of distributions corresponding to the kinematic cuts imposed by the H1 [44] and ZEUS [45] collaborations at the HERA *ep* collider, and compare these results with the experimental data. We also illustrate their sensitivity to the theoretical residual ambiguities intrinsic to the analysis.

6.4.1 Event kinematics and cuts at H1 and ZEUS

The HERA facility collides positrons and protons with energies in the lab frame of $E_e = 27.5$ GeV and $E_p = 820$ GeV respectively, corresponding to events with centre of mass energy $\sqrt{s} \simeq 300$ GeV. In measurements at HERA, the kinematic configuration of an event is reconstructed from information obtained from the scattered lepton, which deposits a high energy cluster in the outermost calorimeters. The two experimental groups necessarily impose a variety of kinematic cuts on the (x, Q^2) space of events measured at HERA. These can be broadly categorised into two groups, those cuts that originate from physical detector limitations, that define the electron acceptance region for the H1 and ZEUS detectors, and those that we impose in order to preclude contamination of the event sample from processes of a genus other than those of immediate

interest for small x phenomenology. We summarize the form of, and motivation for, the cuts on the accessible DIS phase space.

Detector architecture requires that for a scattered electron to trigger the leptonic calorimeter, its polar angle relative to the z-axis is required to satisfy $\theta_{\min} < \theta_e < \theta_{\max}$. The restrictions are naturally specific to the design of the individual detector, so the H1 and ZEUS collaborations will each require a tailored calculation.

By decomposing the four momentum of the incident lepton and proton in the HERA frame, and using the kinematic quantities defined in Section 4.1.1, we can directly reconstruct the event in terms of the standard kinematic quantities. We find

$$Q^2 = 4E_e E'_e \cos^2 \frac{\theta_e}{2}, \quad \text{and} \quad y_e = 1 - \frac{E_e}{E'_e} \sin^2 \frac{\theta_e}{2}. \tag{6.6}$$

Eliminating E'_e, we obtain bounding curves on Q^2 in terms of x and s arising from the accessible polar regions

$$Q^2 = \frac{sx}{1 + xE_p \tan^2 (\theta_e/2) / E_e}. \tag{6.7}$$

In order to reduce the background arising from initial state radiation the experimentalists make the cut $y_e = xQ^2/s > 0.1$. This completes the contours delineating the HERA electron acceptance region marking where we can make DIS observations.

The previous set of restrictions defines a region in (x, Q^2) where the experimental collaborations can in principle make inclusive DIS measurements. However, as was discussed, we require a subset of the full class of DIS events, those containing an identified forward jet, that open a window on small x dynamics. We make additional jet selection criteria in order to suppress extraneous background events. We require a large momentum fraction, $x_j^p = E_j/E_p$, and insist that the jet is scattered through a rather low polar angle, θ_{jet}. Finally, the suppression of the DGLAP evolution length takes the explicit experimental form $0.5 < k_{jT}^2/Q^2 < 2$.

The collected set of kinematic requirements for the various electron acceptance regions and jet selection criteria are given in Table 6.1. Note the marginal difference between the requirements of the H1 and ZEUS collaborations. The electron acceptence region is illustrated in Fig. 6.3.

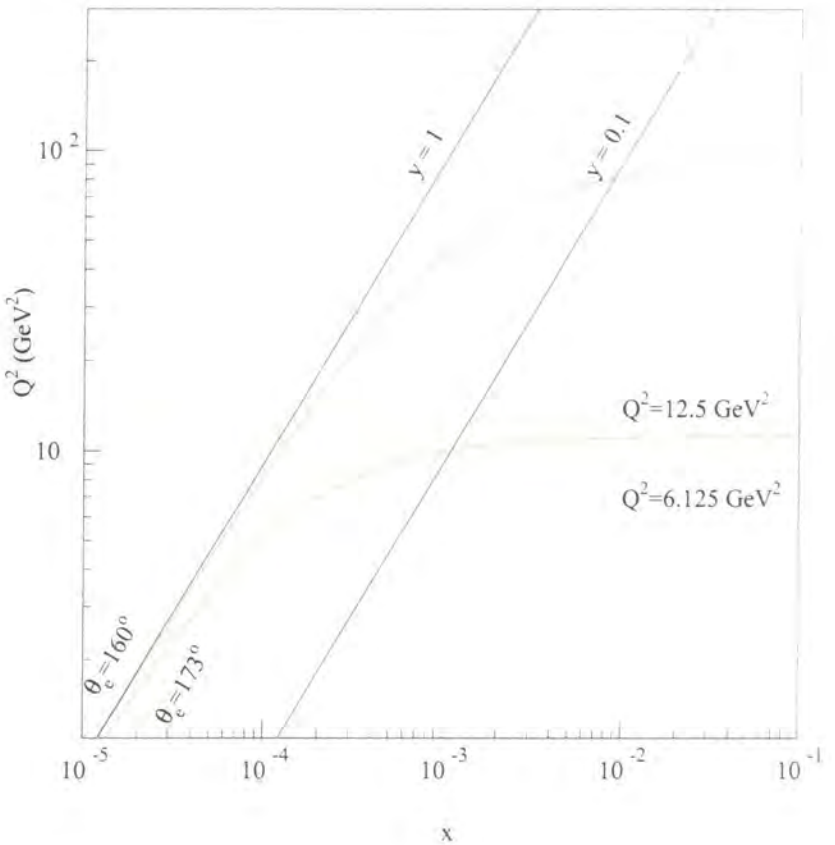

Figure 6.3: The HERA (x, Q^2) kinematic plane, and electron acceptance region (central enclosed area) available to the H1 and ZEUS collaborations subject to cuts originating from detector configuration.

6.4.2 Comparison of experimental and theoretical jet distributions

From Fig. 6.4 we see that the shape of the differential cross-section in x is modelled well for all of the scheme choices. Moreover we obtain a satisfactory normalization of the curve for a physically reasonable choice of scales and infrared cut-off, and is best described by (ii) of (6.3.2).

We see that the uncertainty intrinsic to the calculation due to k_0^2 is much less than the uncertainty due to the scale selection.

We note that explicit fixed order calculations at next-to-leading [46, 47] predict distributions that are a factor of 4 or more beneath the experimental data.

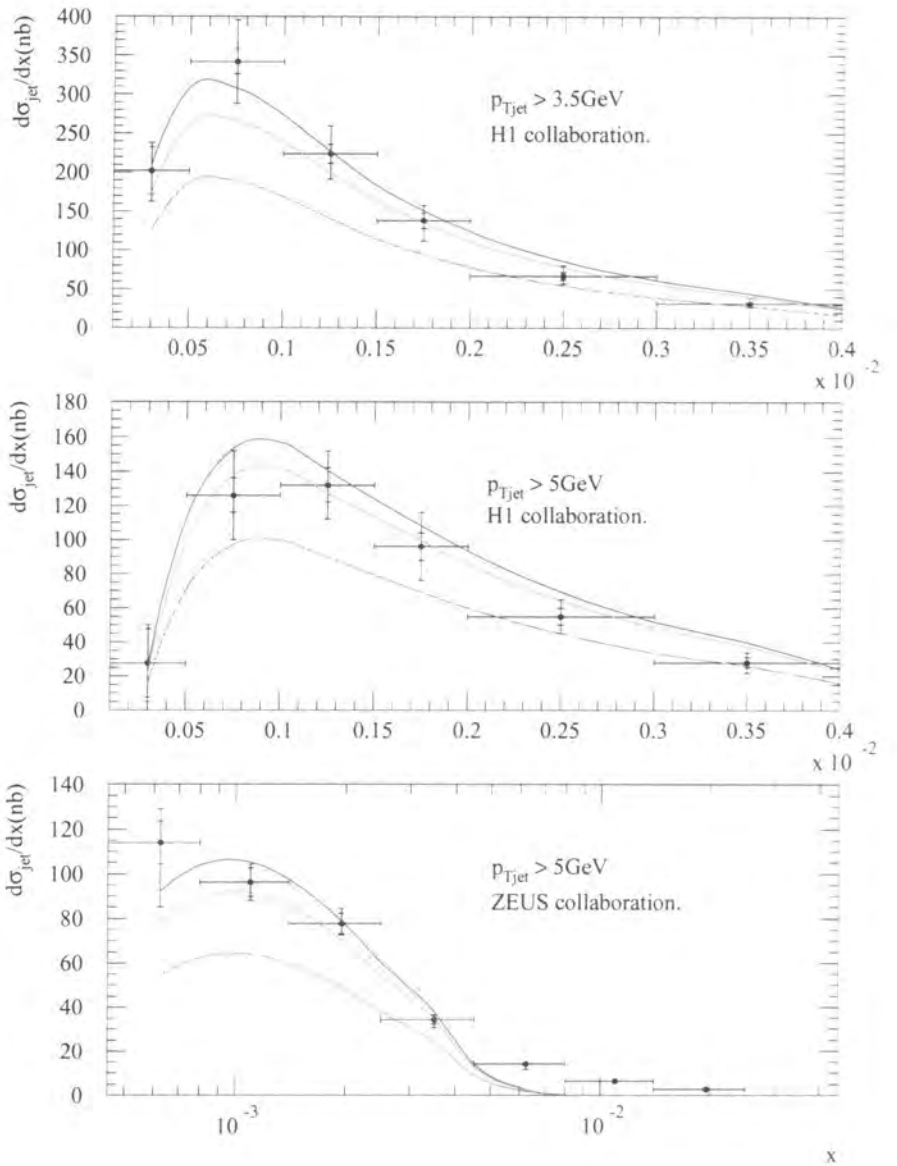

Figure 6.4: The DIS + forward jet differential cross-section versus Bjorken-x as measured at the hadron level by the H1 [44] and ZEUS [45] collaborations. The kinematic cuts are given in Table 6.1. The curves are predictions at the parton level, based on the BFKL formalism including sub-leading corrections, corresponding to the three choices of scales and infrared cut-off given in (6.3.2).

H1 cuts	ZEUS cuts
$E'_e > 11$ GeV	$E'_e > 10$ GeV
$y_e > 0.1$	$y_e > 0.1$
$160^o < \theta_e < 173^o$	
$x_j^p > 0.035$	$x_j^p > 0.036$
$k_{jT} > 3.5$ GeV	$E_{jT} > 5$ GeV
$0.5 < k_{jT}^2/Q^2 < 2$	$0.5 < E_{jT}^2/Q^2 < 2$
$7^o < \theta_{jet} < 20^o$	$\eta_{jet} < 2.6$

Table 6.1: Table showing the kinematic restrictions imposed on DIS events at HERA for forward jet production, by the H1 [44] and ZEUS [45] collaborations.

6.4.3 A caveat - hadronization effects

The experimentalists at HERA naturally make observations of energy deposits arising from hadronic objects, as the initial partonic jet decays into a spray of hadrons with unit probability. The perturbative QCD treatment we have described generates the cross-section for production of a *partonic* forward jet - we have not made any statement about how hadronization occurs, and what effect this might have on the shape of our distributions. Indeed, by comparing hadron level measurments with parton level calculations we implicitly assume that the underlying characteristics of the partonic jet are reflected well by the experimentally defined jet. That this is the case is not readily clear, and there is some evidence that the process of hadronization can enhance a partonic cross-section at small x by $\lesssim 20\%$ [48].

Hadronization corrections have been implemented in monte carlo event generators through phenomenological fragmentation models such as the Lund string model and the HERWIG cluster fragmentation model. These seem to illustrate a significant enhancement when translating results from partonic to hadronic level, see Fig. 6.5 [49].

The definition of a hadronic jet is a 'sensible' convention more than an objective statement. The HERA collaborations choose a cone in azimuth-rapidity space such that particles triggering the detector and lying within a radius of $R < \sqrt{\varphi^2 + \eta^2}$ are taken to originate from a single partonic jet possessing the net kinematics of the observed hadronic jet.

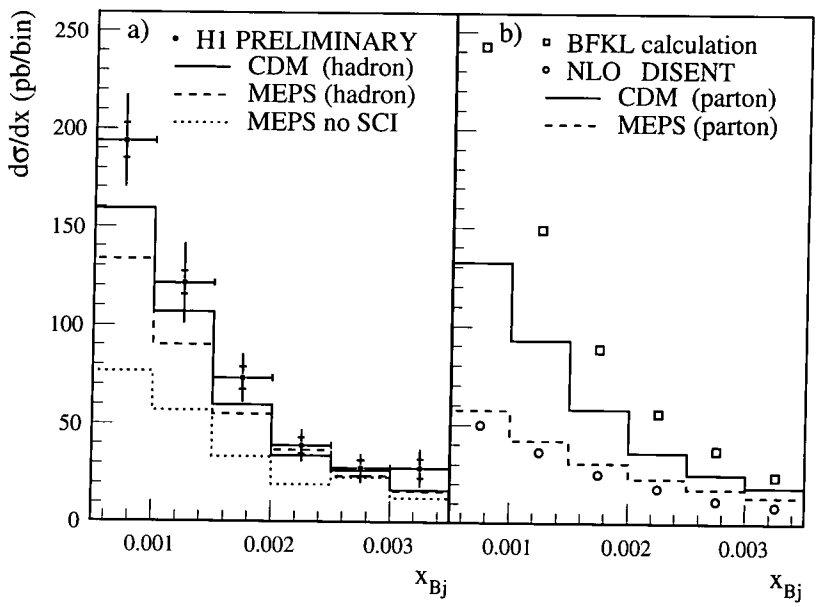

Figure 6.5: Plot [49] illustrating the significant difference between forward jet cross-sections measured at the hadron and parton levels. Plots are shown for hadronization models implementing the Colour Dipole Model, and Matrix Element Parton Showers (with and without soft colour interactions).

In the measurement under consideration, we must clearly identify a hadronic jet at a low polar angle relative to the proton direction. The danger of including detritus arising from the inelastic break-up of the proton is clear - there may be a hadronic bleed from the proton remnants into the observed forward region.

The net effect of hadronization is to undermine the strict forward jet observable as a stringent test of the small x dynamics. Whilst we see broad agreement comparing the features of the H1 and ZEUS distributions, the mismatch in the nature of the calculated and measured observable, and latent model dependence mean that we would be premature in unilateraly identifying the presence of BFKL-type dynamics. A more refined measurement is required to illuminate yet more cleanly the dynamics in play in this region.

6.5 A more exclusive measurement - DIS and a forward π^0

A complementary measurement to Mueller's forward jet process is provided by the production of forward π^0's in deep inelastic events [42],

$$\gamma^* + P \rightarrow \pi^0 + X \tag{6.8}$$

The basic process is the same as before, we derive BFKL type evolution from photon-gluon fusion which couples to a parton from within the proton. At this point, rather than treat the resulting hadron shower in the forward region inclusively, we demand that it contains an identified π^0, assumed to have been produced collinearly with the initial parton jet.

6.5.1 Motivation for the measurement

Practically, measuring an identified hadron in the very forward region proves to be a very difficult procedure. If we require a single very energetic fragment within a jet, we must dramatically reduce the number of candidate events that we can study, which carries along with it a reduction in statistics. Why should time be invested in measuring a process fraught with technical difficulties, and which is a complementary measurement to one less experimentally difficult? It transpires that by requiring an identified hadron in the forward direction, we alleviate many of the remaining uncertainties from which the strictly forward jet measurement suffers.

Pions are selected as the most appropriate hadron to examine, as the lightest particles they are correspondingly the most abundent in the final state. Moreover, neutral pions afford the cleanest experimental signature for identification, their decay $\pi^0 \rightarrow \gamma\gamma$ resulting in a characteristic electromagnetic shower. The sterility of this signal allows a broad region of $(x_\pi, p_{T\pi}^2)$ space to be quantitatively probed at the HERA facility, particularly at the H1 collaboration in the 1994 [44] and 1996 [50] machine runs.

The reconstruction of the jet structure of an event culminating in a shower of hadronic activity is not uniquely defined. Typically an algorithm is invoked which clusters hadrons in the final state by their position in (η, ϕ) space, and different algorithms may generate slightly differing event profiles. If we measure a specific final state we eliminate residual dependence of

the cross-section on jet-finding algorithms.

We saw previously that hadronization effects may have a rather significant effect on the observed cross-section, yet the formalism we have used so far takes no account of them, and should be strictly used for generating parton level cross-sections. Upon extending our formalism to forward pions, the non-perturbative hadronization effects are swept into the fitted parameterizations of *fragmentation functions.*

The final great advantage of looking for forward pions in the final state is that we can probe otherwise unavailable regions of the kinematic space. We replace jet selection criteria with those of the pion and by measuring π^0's at relatively low x_π and $p_{T\pi}$ we effectively collect data for their parent energetic forward jets with $x_j > x_\pi$ and $k_{jT} > p_{T\pi}$, which might otherwise escape detection or be excluded by the jet selection cuts.

6.6 QCD formalism for the production of forward π^0 in DIS

The probability of finding a hadron of species h within a partonic (species i) jet is parameterized by the *fragmentation functions*, $D_i^h(z, \mu^2)$. In some sense these are the 'inverse' of the familiar parton distribution functions, except they parameterize the probability of finding a hadron carrying momentum fraction z of the parent parton at a scale μ^2.

Physically we picture the parton fragmenting through repeated emission of colour charged particles - eventually the potential energy in the system is such that it becomes favourable for the partons to coalesce, in a non-perturbative fashion, into hadronic structure. A schematic for the production of a π^0 from such a partonic jet is shown in Fig. 6.6.

We use a specific parameterization by Binnewies et al. [51] which readily lends itself to incorporation into the numerical convolution. They present leading order fragmentation functions for charged hadrons which assume the particular form

$$D_i^h(z, \mu^2) = N_i(\mu^2)\ z^{\alpha_i(\mu^2)}(1-z)^{\beta_i(\mu^2)}, \tag{6.9}$$

where $i = g, q, \bar{q}$ and μ^2 is the fragmentation scale.

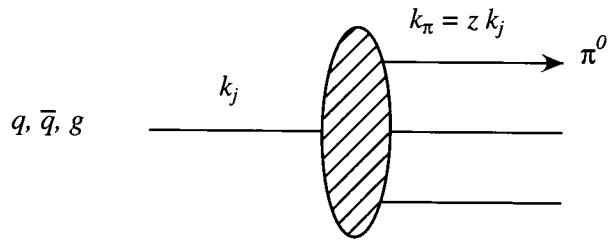

Figure 6.6: Illustration of the hadronization process used for the forward π^0 analysis. An incoming partonic jet fragments into hadronic 'components' through a non-perturbative mechanism represented by the hatched blob. The hadron is produced approximately collinearly with the parent parton with momentum fraction z.

Having identified the π^0 as the most suitable particle for our needs, we need to relate the $D_i^{\pi^0}$ to the functions for charged pions $D_i^{\pi^\pm}$. Fortunately SU(2) isospin symmetry allows us to make an identification of the fragmentation functions corresponding to neutral pion production with those pertaining to charged pion production

$$D_i^{\pi^0}(z,\mu^2) = \frac{1}{2}\left\{D_i^{\pi^+}(z,\mu^2) + D_i^{\pi^-}(z,\mu^2)\right\}.$$

The fragmentation functions require the produced π^0 to carry a fraction $z = x_\pi/x_j^p$ of the partonic jets momentum, in a direction collinear with the initial partonic jet. This is encapsulated within the statement

$$k_\pi = zk_j. \tag{6.10}$$

We then obtain the cross-section for π^0 production by convoluting the DIS + forward jet cross-section, Eqn.(6.1), with the π^0 fragmentation functions, Eqn. (6.9), [42]

$$\frac{\partial\sigma_{\pi^0}}{\partial x_\pi \partial p_{T\pi}^2 \partial x \partial Q^2} = \int_{x_\pi}^1 dz \int dx_j^p \int k_{jT}^2 \delta(x_\pi - zx_j^p)\delta(p_{T\pi} - zk_{jT}) \tag{6.11}$$
$$\left\{\frac{\partial\sigma_g}{\partial x_j^p \partial k_{jT}^2 \partial x \partial Q^2} D_g^{\pi^0}(z,k_{jT}^2) + \frac{4}{9}\sum_{a=q,\bar{q}}\left[\frac{\partial\sigma_a}{\partial x_j^p \partial k_{jT}^2 \partial x \partial Q^2} D_a^{\pi^0}(z,k_{jT}^2)\right]\right\},$$

where the δ-functions ensure Eqn. (6.10), and the differential cross-sections are given by Eqn. (6.2). Note we have explicitly expanded the sum over parton species in the subprocess approximation, and that we take the fragmentations scale of the process, $\mu^2 = k_{jT}^2$.

6.6.1 Event kinematics and cuts at H1

We have a similar variety of kinematic cuts defining the available (x, Q^2) space for DIS events containing a forward π^0 measurement as for the forward jet measurement, Table 6.2. The

1994 H1 data	New H1 data
$E'_e > 12$ GeV	
$y_e > 0.1$	$0.6 > y_e > 0.1$
$156^o < \theta_e < 173^o$	$2 < Q^2 < 70$ GeV^2
$x_\pi > 0.01$	$x_\pi > 0.01$
$p_{T\pi} > 1$ GeV	$p_{T\pi} > 2.5$ GeV
$5^o < \theta_\pi < 25^o$	$5^o < \theta_\pi < 25^o$

Table 6.2: Table showing the kinematic restrictions imposed on DIS events by the H1 collaboration for forward π^0 production.

electron acceptence regions for the 1994 H1 forward jet and forward π^0 [44] data are rather similar, although there is in principle a slight broadening of the phase space allowed by more lax cuts on the polar angle of the scattered electron. In the 1996 H1 data sample [50], the cuts assume a different form - the bounding of y_e together with explicit restrictions on the allowed Q^2 obviates the need for the implicit limitations on (x, Q^2) provided by the θ_e isolines.

6.6.2 Comparison of experimental and theoretical π^0 distributions

There exist two sets of measurements of deep inelastic events containing an identified π^0 in the forward region, both released by the H1 collaboration, corresponding to data taken from HERA runs in 1994 and 1996, and subject to the sampling cuts summarized in Table 6.2.

The earlier data are in the form of π^0 spectra, defined through [42]

$$\frac{1}{N}\frac{dn_\pi}{dx} = \frac{1}{\sigma_{tot}}\frac{\partial\sigma_\pi}{\partial x}, \tag{6.12}$$

where n_π is the number of observed neutral pions in an x bin and N is the total number of DIS events. In Fig. 6.7 we plot the predictions of our analysis corresponding to the 'scheme' choices of Eqn. (6.3.2) with the 1994 H1 π^0 [44] observed spectra in three bins of x_π.

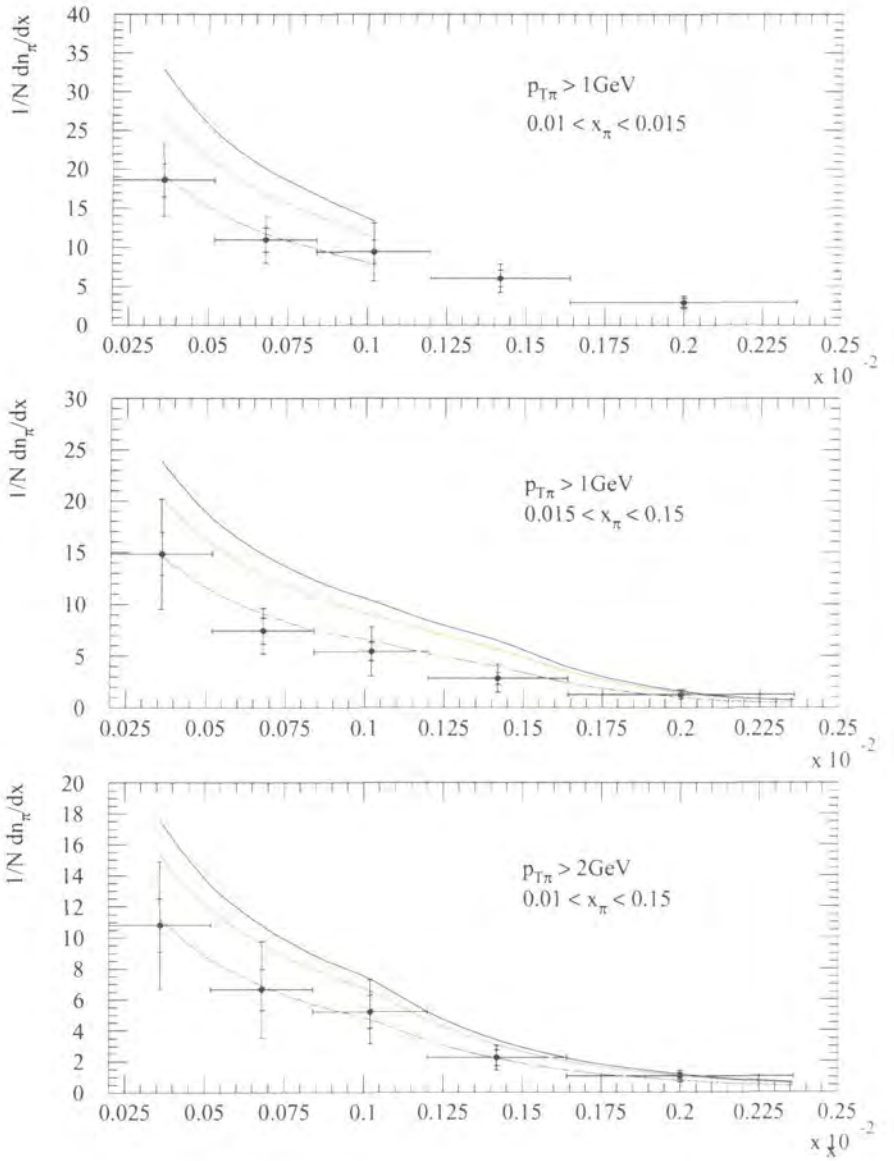

Figure 6.7: The π^0 spectra (6.12) versus Bjorken-x obtained from 1994 H1 data [44]. The curves are predictions, based on the BFKL formalism including sub-leading corrections, corresponding to the three choices of scales and infrared cut-off given in (6.3.2). [The restriction $x/x_\pi < 0.1$ limits the comparison to the domain $x \lesssim 10^{-3}$ in the upper plot.]

In each case of the three choices of scales of α_s and infrared cut-off k_0^2, we find that the shape is described satisfactorily and that the *absolute* normalization is best given by the curve corresponding to (iii) of (6.3.2).

We note that a previous analysis of the same data [42] through a strictly leading logarithmic BFKL formalism yielded distributions (with normalization fixed by reference to forward jet data) which overshot the data by a factor of two. We ascribe this substantial reduction in cross-section as evidence that the imposition of the higher order consistency constraint (5.12) is an important condition for any BFKL based QCD model wishing provide an adequate phenomenological description of data.

The later results of 1996 [50] are completely comprehensive, providing differential cross-section distributions as functions of x, Q^2, $p_{T\pi}$ and the pion pseudorapidity, η_π. We can garner crucial information about the underlying parton dynamics at play[3] in this region by examining each of these distributions in turn.

The single most telling distributions will be the differential cross-sections as a function of x. We have carefully constructed the observable to highlight the characteristic behaviour in x, and hope that the steep $x^{-\lambda}$ behaviour of the gluon distribution, characteristic of the $\log x$ resummation, and central to the calculation, decsribes the data well.

The differential cross-sections as a function of the pseudorapidity variable furnish a complementary insight. A strong ordering in the transverse momenta of the emitted partons (as, for example, in DGLAP evolution) along the chain will necessarily lead to a suppression of jet production at high η_π. The lack of ordering in transverse momentum for the BFKL formalism will manifest itself as a flattening of the distribution as η_π increases.

Both Q^2 and $p_{T\pi}^2$ are potential scales for α_s in a pQCD analysis - we have used $\mu_R^2 \sim k_{jT}^2 = p_{T\pi}^2/z$ as a natural choice for the subprocess. As the scale increases we would anticipate the pQCD description to become more reliable, as α_s decreases, and the perturbative calculation converges more quickly.

In Figs. 6.8 through 6.11 we compare calculations of the π^0 differential cross-sections with

[3]Recall the strong correlation between the parton dynamics and pion behaviour

the most recent H1 data. As for the forward jet process, and the 1994 data, we see broad consistency between our predictions and the observed distributions.

6.7 DIS + 2 forward jets

A small subset of those DIS events satisfying the forward jet criteria possess a distinct *supplementary* jet in the forward region which again fit the qualification conditions met by the initial jet. This process has the following generic description [52]:

$$\gamma^* + P \to \text{jet}_1 + \text{jet}_2 + X.$$

In our picture of small x gluon radiation in the t-channel this corresponds to one of the gluons along the emission chain being real and resolved. We label the forward jets 1 and 2, with jet 2 corresponding to the resolved gluon emission from the BFKL chain. In principle, the second jet can arise from any part of the gluon ladder, although in practise, because of the stringent kinematic cuts required to ensure jet production in the forward region the second jet will be emitted adjacent to the primary forward jet.

The differential cross-section for production of a pair of forward jets is obtained from a modification of Eqn. (6.1) as [52]

$$\frac{\partial\sigma}{\partial x\partial Q^2\partial x_{j1}\partial x_{j2}\partial k_{j1}^2\partial k_{j2}^2} = \frac{4\pi\alpha^2}{xQ^2}\left\{(1-y)\frac{\partial F_2}{\partial x_{j1}\partial x_{j2}\partial k_{j1}^2\partial k_{j2}^2} + \frac{y^2}{2}\frac{\partial F_2}{\partial x_{j1}\partial x_{j2}\partial k_{j1}^2\partial k_{j2}^2}\right\}. \quad (6.13)$$

The additional jet is required to fulfill the same experimental selection criteria of Table 6.2 as for the single jet case which implicitly precludes the development of evolution in $\log 1/x$ between the pair of forward jets. Both partonic jets must possess a significant longitudinal momentum fraction,

$$x_{j2} \lesssim x_{j1} \sim \mathcal{O}(1),$$

such that a strongly ordered configuration between the two, $x_2 \ll x_1 \sim \mathcal{O}(1)$, is forbidden [52]. This restriction in phase space allows us to reject the possibility of soft gluon radiation between the foward jets, which significantly simplifies the formalism for forward dijet production. A schematic for such a process is illustrated in Fig. 6.12. The rate of forward dijet production offers us a further complementary measurement for probing small x dynamics.

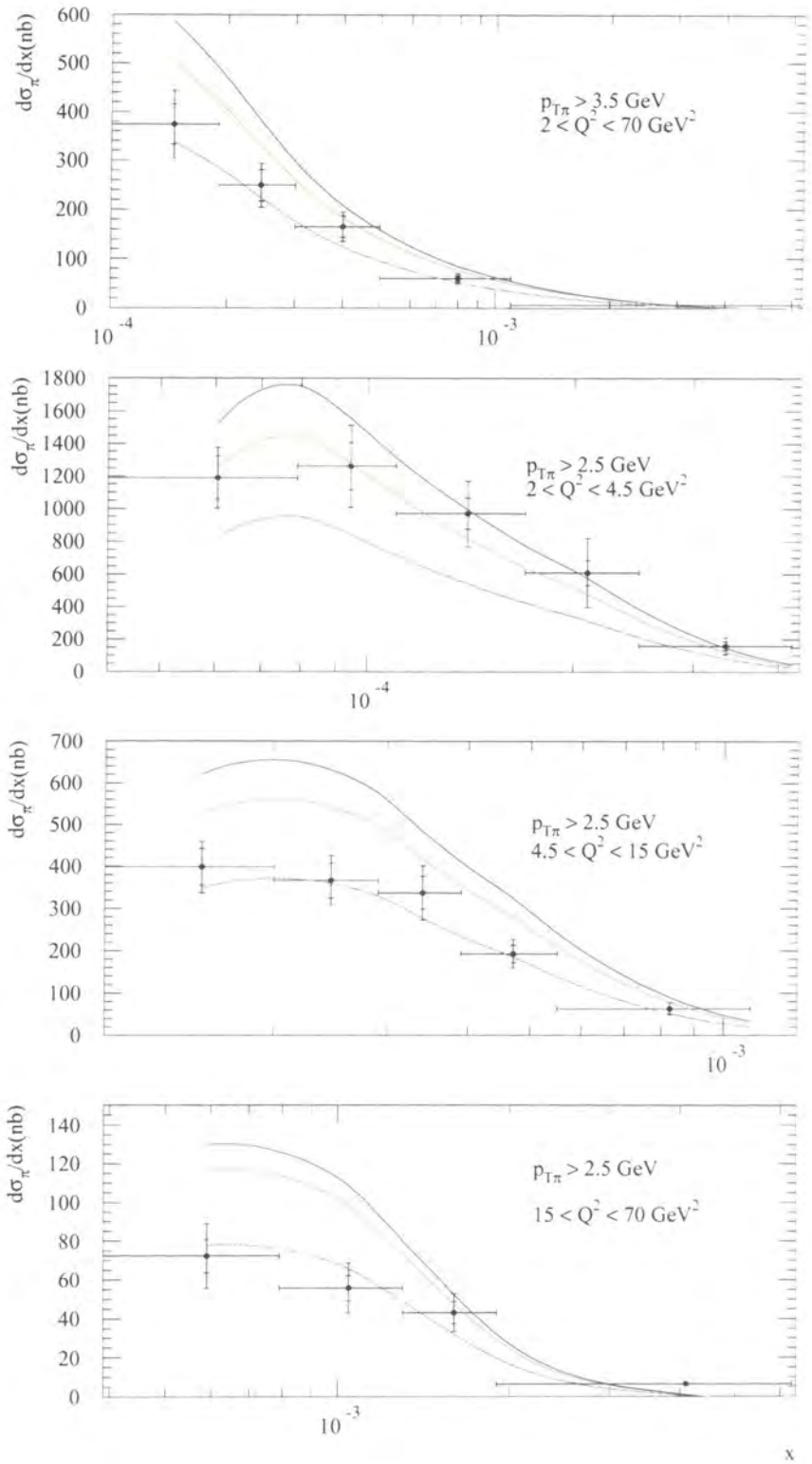

Figure 6.8: The π^0 differential cross-section versus Bjorken-x obtained from 1996 H1 data [50]. The curves are predictions, based on the BFKL formalism including sub-leading corrections. corresponding to the three choices of scales and infrared cut-off given in (6.3.2).

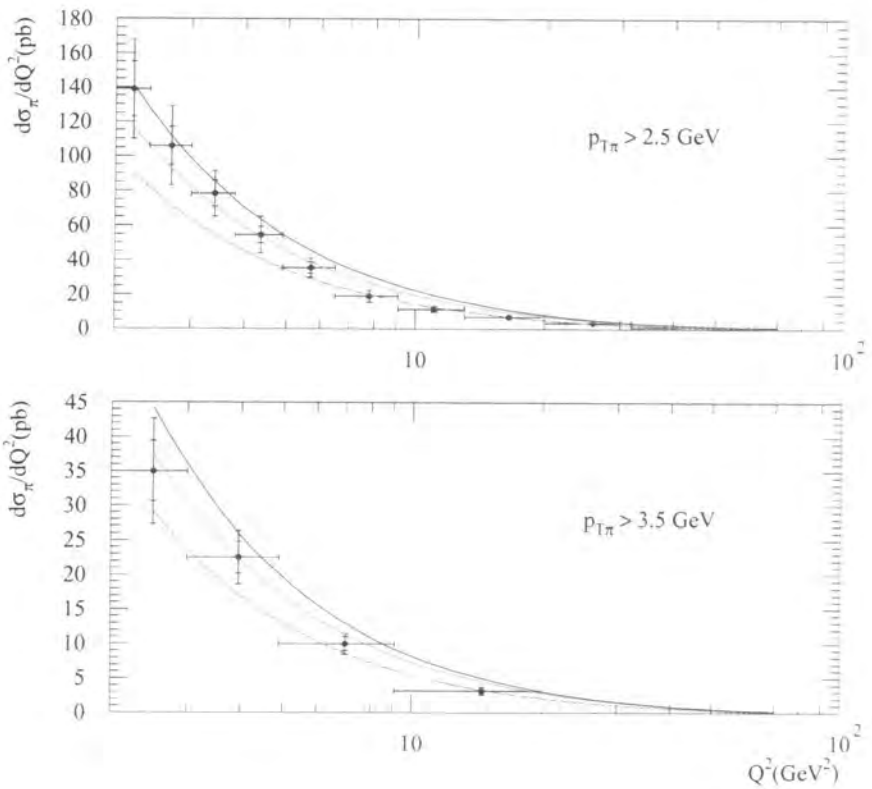

Figure 6.9: The π^0 differential cross-section versus Q^2 obtained from 1996 H1 data [50]. The curves are predictions, based on the BFKL formalism including sub-leading corrections. corresponding to the three choices of scales and infrared cut-off given in (6.3.2).

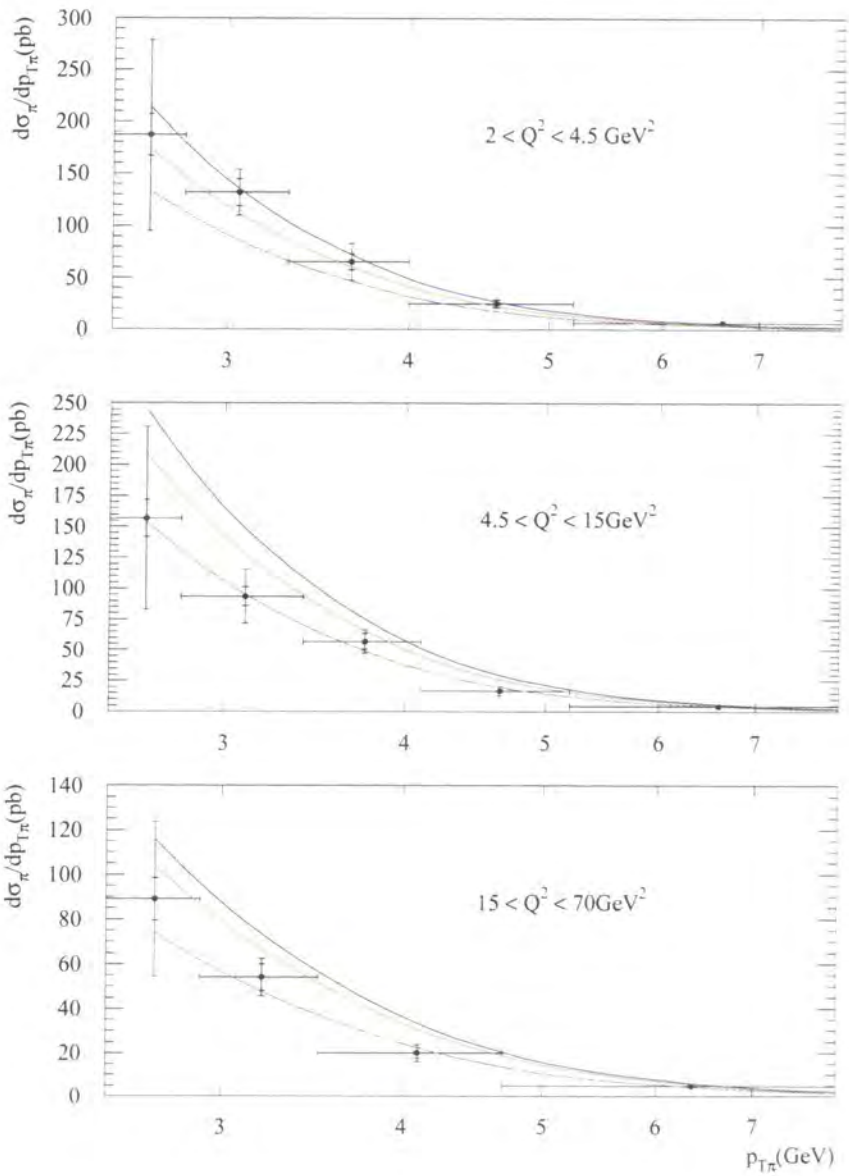

Figure 6.10: The π^0 differential cross-section in transverse momentum, obtained from 1996 H1 data [50]. The curves are predictions, based on the BFKL formalism including sub-leading corrections, corresponding to the three choices of scales and infrared cut-off given in (6.3.2).

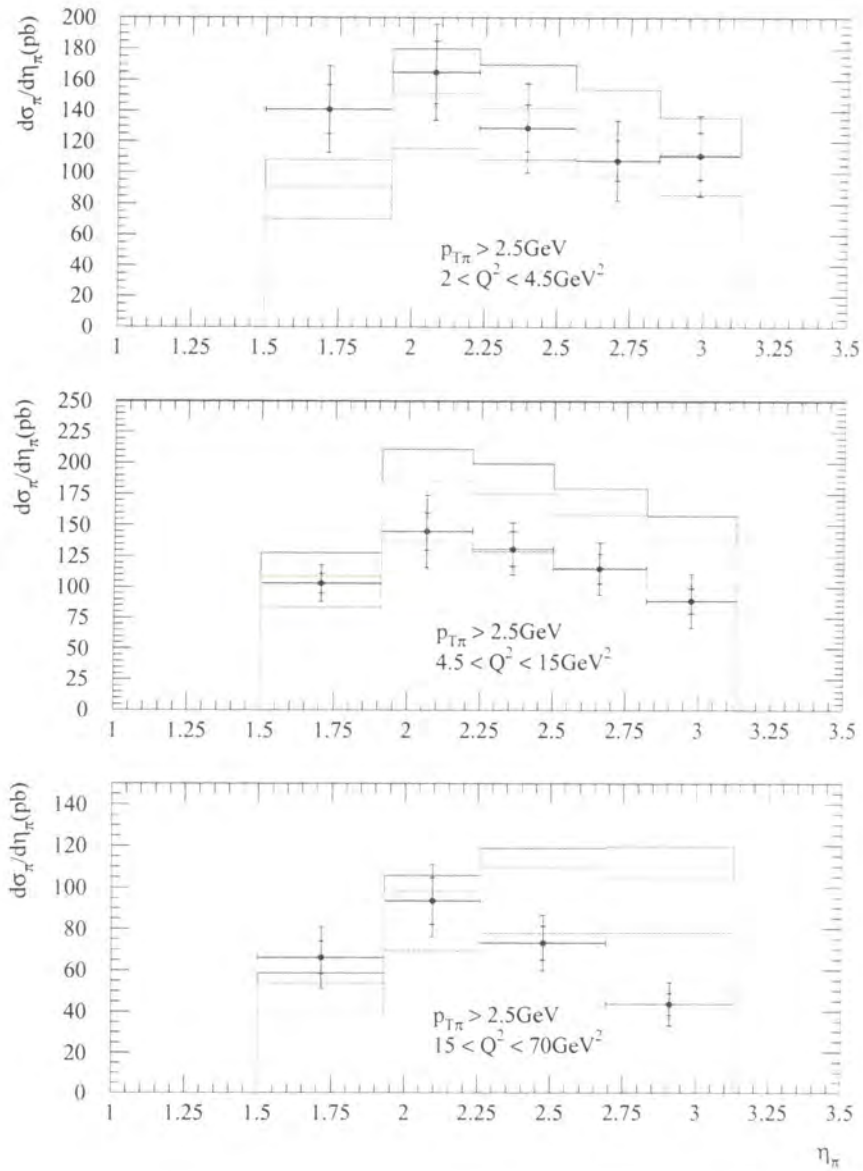

Figure 6.11: The π^0 differential cross-section versus rapidity obtained from 1996 H1 data [50]. The curves are predictions, based on the BFKL formalism including sub-leading corrections, corresponding to the three choices of scales and infrared cut-off given in (6.3.2).

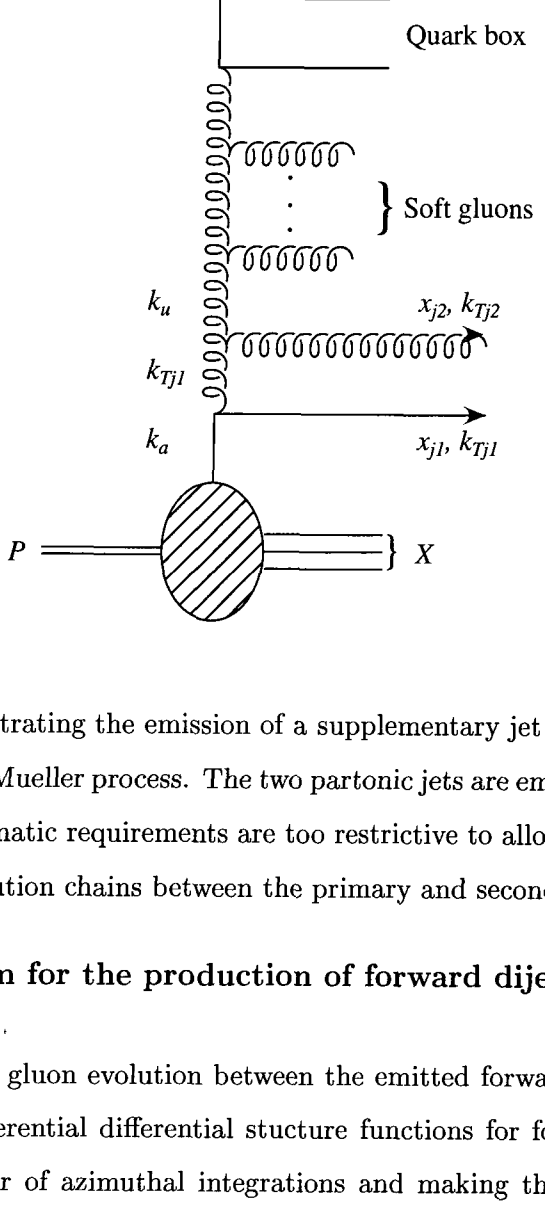

Figure 6.12: Diagram illustrating the emission of a supplementary jet in the forward region, in adddition to the standard Mueller process. The two partonic jets are emitted consecutively along the gluon chain - the kinematic requirements are too restrictive to allow for the development of further small-x gluon evolution chains between the primary and secondary forward jets.

6.7.1 QCD formalism for the production of forward dijets in DIS

The suppression of further gluon evolution between the emitted forward jets greatly simplifies the expression for the differential differential stucture functions for forward dijet production. After performing a number of azimuthal integrations and making the approximation of null evolution between jets it is found that the differential structure functions take the form [52]

$$x_{j2}\frac{\partial F_i}{\partial x_{j1}\partial x_{j2}\partial k_{j1}^2\partial k_{j2}^2} = \frac{1}{2\pi}\int_0^{2\pi} d\varphi\ \Phi_i(x/x_{j2}, k_u^2, Q^2)\frac{\bar{\alpha}_s(k_{j1}^2)\bar{\alpha}_s(k_{j2}^2)}{k_u^2 k_{j1}^2 k_{j2}^2}\sum_a f_a(x_{j1}, k_{j1}^2). \quad (6.14)$$

where φ is here the azimuthal angular separation between the two forward jets, and $\boldsymbol{k_u} = \boldsymbol{k_{j1}} + \boldsymbol{k_{j2}} \rightarrow k_u^2 = k_{j1}^2 + k_{j2}^2 + 2k_{j1}k_{j2}\cos(\varphi)$. The functions Φ_i are numerically evaluated using the Chebyshev polynomial technique.

As well as insisting that the secondary jet adheres to the same criteria as the primary forward jet, we must ensure that both jets are distinguishable. We make a supplementary requirement on the system of partonic jets which insists each can be resolved individually in an experimental event reconstruction. If the two jets were to be produced close to one another in phase space, there is the possibility that the jet finding algorithms used would be unable to separate the hadronic final states as originating from distinct jet events - these would be classified as single jet events. We insist on two distinct partonic jets by requiring that they are well separated in pseudo-rapidity azimuth space, that is the kinematics of the jets contravene the jet cone selection algorithm,

$$\sqrt{(\Delta\varphi)^2 + (\Delta\eta)^2} > R_{\min} = 1.$$

In principle, 'misidentified' multijet events should be included within the single jet cross-sections, however, their rate proves to be negligible in comparison to the proper single forward jet cross-section.

6.7.2 Comparison of experimental and theoretical forward dijet rates

The H1 collaboration published a result [44] in 1994 corresponding to a total cross-section for forward dijet prouction of 6 ± 0.8 (stat) ± 3.2 (sys) pb. In our formalism we are subject to the same parametric freedoms in choice of scale and infrared cutoff as before, and so we calulate a set of results corresponding to the calculation schemes given in (6.3.2). We find total cross-sections of 5.2, 4.8 or 2.7pb respectively.

Given the variation in absolute normalization for the prediction it is instructive to examine the total two-jet/one-jet ratio. The predictions for this quantity are rather stable at 1.0, 1.1 and 0.8% respectively, to be compared with the H1 observation of $1.1 \pm 0.6\%$ [44]. We conclude that small x QCD is able to satisfactorily reproduce the observed rate of forward dijet production.

6.8 An alternative description - the resolved photon

In Fig. 6.13 we illustrate a second mechanism by which forward jets in DIS can be modelled, the *resolved photon* [53, 54]. This approach separates the analysis into two distinct scenarios.

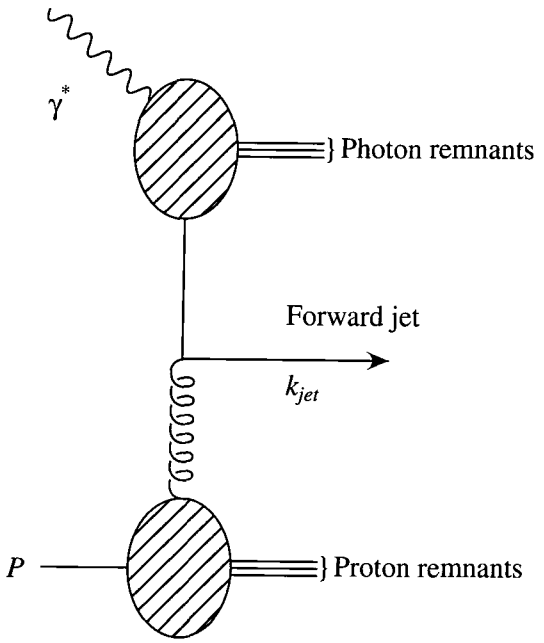

Figure 6.13: Diagram illustrating the resolved photon model of the forward jet process. Two k_T^2 ordered parton cascades extend from the photon and the proton ends of the evolution.

When the characteristic scale of the process satisfies $\mu^2 < Q^2$ a standard perturbative approach is used. However, when the converse is true and $Q^2 < \mu^2$ the parton is able to resolve partonic structure *within* the virtual photon, which is parameterized by a set of parton density functions, $f_{a,\gamma^*}(x,\mu^2)$, for example [55], analagous to the familiar hadronic pdfs, $f_{a,P}(x,\mu^2)$. Both sets of partonic structure can then be allowed to develop k_T^2 ordered parton showers, and in some sense the treatment then mimics the k_T^2 disorder inherent in the BFKL formalism.

We have emphasized that the gluon distribution arising in our analysis can also be considered as a hard scattering of partons in the virtual photon. This formalism is somewhat more aesthetic in the sense that the Q^2 dependence of the virtual photon partons is generated dynamically through the quark box. It also has the conceptual advantage of treating in a unified way all

possible kinematic configurations, we avoid a demarcation of the process according to the two potentially large scales Q^2 and k_{jT}^2 of the problem.

Chapter 7

Summary and conclusions for BFKL phenomenology

The second half of this thesis consists of studies of small Bjorken x phenomenology, that is the physics of deep inelastic scattering events which are selected on the basis that their intrinsic characteristics highlight the underlying low x dynamics.

We began in Chapter 4 with a brief review of the basic deep inelastic scattering process, introducing the nomenclature and ideas used throughout the remainder of the thesis. Chief amongst these was the concept of resummation of large logarithms of the kinematic variables, Q^2 and x, which become important according to the kinematic domain of the particular DIS event. This led naturally to the DGLAP and BFKL evolution equations which (at leading logarithmic level) resum terms containing $[\alpha_s \log(Q^2/Q_0^2)]^r$ and $[\alpha_s \log(1/x)]^r$ and correspond to ladder diagrams in distinct regimes of ordering of the kinematic variables. These equations predict starkly differing behaviour for the evolution of the parton distributions, and it is an obvious test of QCD to try and distinguish which of the dynamical modes operates at the currently accessible energy reach of today's colliders.

However, in the course of reviewing the BFKL formalism, we illustrated (by reference to the next-to-leading-log kernel) that the leading-log prescription was inadequate as a reliable description of small x phenomenology, and that the full next-to-leading corrections also suffered

from sufficient deficiences to invalidate its phenomenological application.

Following the suggestion of [31], a subleading modification, preserving the crucial scale invariance of the leading-log BFKL equation was motivated - the so-called 'consistency constraint', which is readily implemented at all orders. This correction limits the transverse momentum of the emitted gluons along the small x evolution chain, and by reference to an analytic solution to each of the leading-log and modified BFKL equations for fixed α_s was shown to suppress the characteristic exponent of the dominant small x unintegrated gluon distribution.

We then examined the prospects for identifying BFKL dynamics at the positron-proton collider at HERA in the DESY facility. As is well known, inclusive observables prove to be too theoretically flexible to allow a truly discriminatory test of the underlying physics, parametric freedom in the input gluon distribution permitting sufficient leeway for the double logarithmic limit of DGLAP evolution to model the observed rise in quanitities such as F_2, which might otherwise be attributable to BFKL resummation.

Exclusive measurements of the final state prove a more fruitful alternative prospect. By selecting events (Mueller jets) with kinematics tailored to exclude DGLAP evolution $k_{jT}^2 \simeq Q^2$, and maximise the small x evolution length $x \ll x_j$, we enhance the prospect for unambiguous identification of the BFKL dynamics. Experiments measuring the behaviour of jets in the very forward region are exactly what is required.

In this thesis we model a variety of exclusive processes using the modified BFKL formalism described previously, along with a running coupling. We first examine the behaviour of identifed hadronic jets in the very forward regions of the detectors. Both H1 and ZEUS collaborations have sets of data which are well modelled for physical sets of the scale of α_s and infrared cut off imposed to ensure a perturbative treatment. We investigate the sensitivity of the results to the theoretical parameters of the calculation, the aforementioned scale and cut-off, and find that the shape of the distibutions are stable, although the normalization is less well determined, being comparatively more sensitive to shifts in scale than cut-off.

Following this, we discuss briefly the uncertainties engendered by hadronization effects - we have made predictions on the partonic level, whilst experimentalists measure hadrons in the

final state. Motivated by this caveat, we introduce a set of corollary measurements, the subset of DIS events containing an energetic identified forward pion, and discuss its chief merits. By requiring a π^0 we obviate the need for discussion of the effects of hadronization - these are swept into phenomenologically fitted parameterizations, fragmentation functions. Simultaneously we circumvent ambiguities due to jet algorithms and are also effectively probing a broader kinematic space for the parent jet than if we required an inclusive hadronic jet. We do not gain these advantages for free however - clearly the rate for production of forward pions is severely diminished compared with the forward jet measurements.

Despite the experimental difficulties, two sets of data on the forward pion process have been collected by the H1 collaboration at HERA. The first and earlier of these are in the form of spectra, and again can be modelled well by the same sets of reasonable choice of scale and cut-off as for the forward jet case, albeit subject to similar normalization uncertainties.

The second set of data is comprehensively decomposed as differential cross-sections, which highlight the features of the data as functions of all the pertinent quantities. Once more we find that we are able to consistently model the features with a similar choice of model parameters, and again investigate the normalization uncertainies implicit in the model dependence on scale and cut-off.

We finally turn to one further measure of the dynamics that can be extracted from the data. A certain proportion of those DIS forward jet events possess a supplementary jet in the forward region also adhering to the same criteria. The rate of these forward dijet events was measured by the H1 collaboration and found to amount to some 1% of the total forward jet sample. Upon modelling the forward jet process supplemented with an additional forward jet arising from the base of the gluon evolution chain, we find good agreement for the two-jet/one-jet ratio for all the choices of the computational parameters.

In summary, we feel that experimental studies of the production of hadronic jets and pions in the forward region require small x resummation effects for good phenomenological description. (Recall that fixed order calculations lay significantly beneath the data [46, 47]). Moreover, we believe the modified BFKL framework provides an economical and ready prescription for including *to all orders* the dominant subleading effects, which appear to be a prerequisite for

modelling real processes.

We finally discuss briefly the concept of the resolved photon, an alternative mechanism that produces a crude disorder in Q^2 along the evolution chain, according to the scale of the subprocess. We sketch intuitively that the BFKL formalism is a more aesthetic way of describing the hadronic content of the photon, generating dynamically Q^2 dependence through the quark box mechanism.

Clearly further and broader phenomenological examinations of the BFKL formalism are necessary to establish its presence in the HERA kinematic domain, and especially the need for subleading corrections in the form of the consistency constraint. One promising avenue of enquiry is the angular dependence of observables in hadronic collisions. The suppression of the dominant $m = 0$ angular projection of the modified BFKL equation was shown to be weakened for higher $m \geq 1$ projections, for fixed α_s. In principle this affords a discriminatory mechanism between the strictly leading-log and modified BFKL equations, the dominant $m = 0$ projection dominates the higher terms contributing to angular dependence, washing out the azimuthal angle dependence of the full gluon distribution in comparison with the modified case. Observables such as the azimuthal decorrelation of dijets at the Tevatron provide a good platform to test the necessity for the subleading corrections, indeed it has already been shown [56], that the leading-log BFKL formalism overestimates the amount of decorrelation. Further study in this area would be a fascinating indication of the validity of the modified BFKL small x formalism.

Appendix A

Analytical, asymptotic solution to the BFKL equation

In this appendix we present the solution of the modifed BFKL equation containing the full azimuthal dependence, φ. The method described follows that of A.J.Askew, [57] and is applied to the more phenomenologically appropriate modified BFKL equation containing the *consistency constraint.* We can formulate an asymptotic analytic solution to the BFKL equation by choosing the coupling α_s fixed. We will explore how the modified equation is diagonalized by the Mellin transforms already introduced, and illustrate how the leading behaviour can be recovered.

A.1 The complete azimuthal dependent modified BFKL kernel

The modified BFKL equation, written in its raw form is given by

$$f(x,\boldsymbol{k}) = f^{(0)}(x,\boldsymbol{k}) + \bar{\alpha}_s \int_x^1 \frac{dz}{z} \int \frac{d^2\boldsymbol{q}}{\pi q^2} \left\{ f\left(\frac{x}{z}, \boldsymbol{k}+\boldsymbol{q}\right) \Theta\left(\frac{k^2}{q^2+k^2} - z\right) - \frac{k^2}{q^2+(\boldsymbol{k}+\boldsymbol{q})^2} f\left(\frac{x}{z}, \boldsymbol{k}\right) \right\}.$$

We first shift the integration variables, letting $\boldsymbol{k'} = \boldsymbol{k} + \boldsymbol{q}$, and approximate the consistency constraint, manifest in the argument of the Θ-function, by

$$\Theta\left(\frac{k^2}{k^2+q^2} - z\right) \to \Theta\left(\frac{k^2}{k'^2} - z\right).$$

We now Fourier expand the unintegrated gluon distributions in accordance with Eqn. (5.3), and insist that the BFKL equation must hold simultaneously for each of the azimuthal projections m. It now reads

$$e^{im\varphi}\phi_m(x,k^2) = e^{im\varphi}\phi_m^{(0)}(x,k^2) + \bar{\alpha}_s k^2 \int_x^1 \frac{dz}{z}\int \frac{dk'^2}{k'^2}\frac{d\varphi'}{2\pi} \tag{A.1}$$
$$\left\{ \frac{\phi_m(x/z,k'^2)\ \Theta\left(\frac{k^2}{k'^2}-z\right) e^{im\varphi'}}{k'^2+k^2-2k'k\cos(\varphi'-\varphi)} - \frac{k'^2\phi_m(x/z,k^2)e^{im\varphi}}{[2k'^2+k^2-2k'k\cos(\varphi'-\varphi)][k'^2+k^2-2k'k\cos(\varphi'-\varphi)]} \right\}.$$

The azimuthal integrations can readily be performed using complex analysis. Integrating over φ' in the real emission term we obtain

$$\int_0^{2\pi}\frac{d\varphi'}{2\pi}\frac{e^{im\varphi'}}{k'^2+k^2-2k'k\cos(\varphi'-\varphi)} = \frac{e^{im\varphi}}{|k'^2-k^2|}\min\left(\frac{k^2}{k'^2},\frac{k'^2}{k^2}\right)^{m/2}$$

We can use partial fractions to split the virtual emission term into two,

$$\int_0^{2\pi}\frac{d\varphi'}{2\pi}\frac{1}{[k'^2+k^2-2k'k\cos(\varphi'-\varphi)]} = \frac{1}{|k'^2-k^2|},$$

which simply corresponds to the $m=0$ case of the real emission term and

$$\int_0^{2\pi}\frac{d\varphi'}{2\pi}\frac{1}{[2k'^2+k^2-2k'k\cos(\varphi'-\varphi)]} = \frac{1}{(4k'^4+k^4)^{1/2}}.$$

Once substituted back into Eqn. (A.1), and factoring out common factors of $e^{im\varphi}$ we obtain the base form of the equation used throughout this thesis

$$\phi_m(x,k^2) = \phi_m^{(0)}(x,k^2) + \bar{\alpha}_s k^2\int_x^1\frac{dz}{z}\int_0^\infty\frac{dk'^2}{k'^2} \tag{A.2}$$
$$\left\{\frac{\phi_m(x/z,k'^2)\ \Theta\left(\frac{k^2}{k'^2}-z\right)\min\left(\frac{k^2}{k'^2},\frac{k'^2}{k^2}\right)^{m/2}-\phi_m(x/z,k^2)}{|k'^2-k^2|}+\frac{\phi_m(x/z,k^2)}{(4k'^4+k^4)^{1/2}}\right\}$$

Crucially, the scale invariance of the equation is once again apparent, its form remaining unchanged under the transformation $k\to\lambda k$, which admits the analytic approach using Mellin transforms. We now perform the transforms given in Eqns. (5.5) to diagonalize the double convolution and obtain

$$\hat{\phi}_m(\omega,\varrho) = \hat{\phi}_m^{(0)}(\omega,\varrho) + \bar{\alpha}_s\hat{\phi}_m(\omega,\varrho)\int_0^\infty\frac{dk'^2}{k'^2}k^2 \tag{A.3}$$
$$\left\{\frac{\tilde{\phi}_m(\omega,k'^2)}{\tilde{\phi}_m(\omega,k^2)}\frac{\min\left(\frac{k^2}{k'^2},\frac{k'^2}{k^2}\right)^{m/2}}{|k'^2-k^2|}\int_0^1 dz\ z^{\omega-1}\ \Theta\left(\frac{k^2}{k'^2}-z\right)-\frac{1/\omega}{|k'^2-k^2|}+\frac{1/\omega}{(4k'^4+k^4)^{1/2}}\right\}.$$

We now exploit a change of variables, $k'^2 = uk^2$, and noticing that $\tilde{\phi}_m(\omega, k'^2)/\tilde{\phi}_m(\omega, k^2) = u^{\varrho}$ [1] the equation is rendered in (ω, ϱ) space as an eigenfunction problem for $\hat{\phi}_m(\omega, \varrho)$,

$$\hat{\phi}_m(\omega,\varrho) = \hat{\phi}_m^{(0)}(\omega,\varrho) + \bar{\alpha}_s \hat{\phi}_m(\omega,\varrho) \int_0^\infty \frac{du}{u} \left\{ \frac{u^\varrho \ \min(u,1/u)^{m/2}}{|u-1|} \int_0^1 dz \ z^{\omega-1} \ \Theta\left(\frac{1}{u} - z\right) - \frac{1/\omega}{|u-1|} + \frac{1/\omega}{(4u^2+1)^{1/2}} \right\}. \tag{A.4}$$

To resolve the form of the BFKL kernel we distinguish between the distinct intervals of integration, $0 \leq u \leq 1$ and $1 < u < \infty$, corresponding to $k'^2 \leq k^2$ and $k'^2 > k^2$. This allows us to complete the z integration in each region

$$\int_0^1 dz \ z^{\omega-1} \ \Theta\left(\frac{1}{u} - z\right) = \begin{cases} 1/\omega & \text{if } u \leq 1 \\ u^{-\omega}/\omega & \text{if } u > 1 \end{cases}$$

and gives our equation for the eigenfunction $\hat{\phi}_m(\omega, \varrho)$

$$\begin{aligned} \hat{\phi}_m(\omega,\varrho) = \hat{\phi}_m^{(0)}(\omega,\varrho) \ &+ \ \hat{\phi}_m(\omega,\varrho)\frac{\bar{\alpha}_s}{\omega}\int_0^1 \frac{du}{u}\left\{\frac{u^{\varrho+m/2}-1}{u-1} + \frac{1}{(4u^2+1)^{1/2}}\right\} \\ &+ \ \hat{\phi}_m(\omega,\varrho)\frac{\bar{\alpha}_s}{\omega}\int_1^\infty \frac{du}{u}\left\{\frac{u^{\varrho-m/2-\omega}-1}{1-u} + \frac{1}{(4u^2+1)^{1/2}}\right\}. \end{aligned}$$

In the latter integral we now let $v = 1/u$ and obtain

$$\begin{aligned} \hat{\phi}_m(\omega,\varrho) = \hat{\phi}_m^{(0)}(\omega,\varrho) \ &+ \ \hat{\phi}_m(\omega,\varrho)\frac{\bar{\alpha}_s}{\omega}\int_0^1 du\left\{\frac{u^{\varrho+m/2-1}-1}{u-1} - \frac{1}{u} + \frac{1}{u(4u^2+1)^{1/2}}\right\} \\ &+ \ \hat{\phi}_m(\omega,\varrho)\frac{\bar{\alpha}_s}{\omega}\int_0^1 \frac{dv}{v}\left\{\frac{v^{m/2+\omega-\varrho}-1}{1-v} + \frac{1}{(4/v^2+1)^{1/2}}\right\} \end{aligned}$$

Finally we utilise a series of standard integrals [58] to obtain the modified BFKL kernel in Mellin transform space,

$$\begin{aligned} \int_0^1 du\left(\frac{u^{z-1}-1}{1-u}\right) &= -\gamma_\epsilon - \psi(z) \\ \int_0^1 \frac{du}{u}\left(\frac{1}{(4u^2+1)^{1/2}} - 1\right) &= -\log\left(\frac{1+\sqrt{5}}{2}\right) \\ \int_0^1 \frac{du}{(4+u^2)^{1/2}} - 1 &= \log\left(\frac{1+\sqrt{5}}{2}\right), \end{aligned}$$

with $\psi(z)$ being the logarithmic derivative of the Euler Γ function, $\psi(z) = \Gamma'(z)/\Gamma(z)$, defined for $Re\ z > 0$, and $\gamma_\epsilon = -\psi(1) \simeq 0.577$ is the Euler-Mascheroni constant.

[1] The origin of this relation can be made clear by evaluating $\tilde{\phi}_m(\omega, uk^2)$ and $\tilde{\phi}_m(\omega, k^2)$ using the first of the Mellin transforms of Eqns. (5.5).

We obtain a succinct representation of the modified BFKL equation, diagonalized in (ω, ϱ) space and expressed as

$$\hat{\phi}_m(\omega,\varrho) = \hat{\phi}_m^{(0)}(\omega,\varrho) + \frac{\bar{\alpha}_s}{\omega}\hat{\phi}_m(\omega,\varrho)\ \mathcal{K}_m^{CC}(\omega,\varrho), \tag{A.5}$$

where the modified kernel function, $\mathcal{K}_m^{CC}(\omega,\varrho)$, is given by [2]

$$\mathcal{K}_m^{CC}(\omega,\varrho) = 2\psi(1) - \psi(\varrho + m/2) - \psi(\omega - \varrho + m/2 + 1). \tag{A.6}$$

A.2 Recovering the leading logarithmic BFKL kernel

It is worthwhile briefly explaining how we recover the leading logarithmic BFKL equation from the previous analysis. The chief characteristic of the modifed equation is the introduction of the Θ-function limiting the phase space available to the real gluon emissions. Were we to omit this restriction, and follow the arguments outlined above, we would find instead of distinct ω dependence induced in the regions $0 \leq u \leq 1$ and $1 < u < \infty$ for Eqn. (A.4), we would instead have a global factor of $1/\omega$. All ω dependence drops out from within the u integrals, which feeds through into an independence of the leading logarithmic kernel function from ω,

$$\hat{\phi}_m(\omega,\varrho) = \hat{\phi}_m^{(0)}(\omega,\varrho) + \frac{\bar{\alpha}_s}{\omega}\hat{\phi}_m(\omega,\varrho)\ \mathcal{K}_m^{LL}(\varrho), \tag{A.7}$$

with the well known leading kernel given by

$$\mathcal{K}_m^{LL}(\varrho) = 2\psi(1) - \psi(\varrho + m/2) - \psi(m/2 - \varrho + 1). \tag{A.8}$$

whose $m = 0$ component saturates its maximal value of $4\log 2$ at $\varrho = 1/2$.

A.3 Asymptotic solution

The solution of the BFKL equation in (ω, ϱ) space is readily obtained from Eqn. (A.5) via a simple rearrangement

$$\hat{\phi}_m(\omega,\varrho) = \frac{\omega\ \hat{\phi}_m^{(0)}(\omega,\varrho)}{\omega - \bar{\alpha}_s\mathcal{K}_m^{CC}(\omega,\varrho)}. \tag{A.9}$$

[2] The subscript m refers to the Fourier projection, whilst the superscript CC refers to the consistency constraint adaption of the leading logarithmic BFKL equation (and not charged current!).

We can use the inverse Mellin transforms of Eqns. (5.9) to recover an asymptotic solution for the unintegrated gluon in the kinematical space (x, k^2).

We first undo the $x \to \omega$ transformation

$$\tilde{\phi}_m(x,\varrho) = \oint_{C-i\infty}^{C+i\infty} \frac{d\omega}{2\pi i} x^{\omega} \hat{\phi}_m(\omega,\varrho) \tag{A.10}$$

where the contour of integration lies to the right of all poles in ω. We assume that the inhomogeneous driving term does not contribute to the zeroes of the denominator of $\hat{\phi}_m(\omega,\varrho)$, so the poles are completely determined by the series of solutions to the implicit equation $\omega_m^i(\varrho) = \bar{\alpha}_s \mathcal{K}_m^{CC}(\omega_m^i(\varrho),\varrho)$. We can then evaluate the integrand using the Residue theorem giving

$$\tilde{\phi}_m(x,\varrho) = \sum_i x^{\omega_m^i(\varrho)} R_m^i(\varrho), \tag{A.11}$$

where $R_m^i(\varrho)$ is the residue associated with the ith pole of the mth fourier projection, determined by the $\omega\hat{\phi}_m^{(0)}(\omega,\varrho)$ numerator of Eqn. (A.9).

The leading pole, $\omega_m^0(\varrho)$ will be dominant in phenomenological applications, and so we henceforth drop the subleading poles, $i > 0$. For some $x_0 > x$, with both x and x_0 sufficiently small for the use of the BFKL equation to be justified, we can write

$$\tilde{\phi}_m(x,\varrho) = \tilde{\phi}_m(x_0,\varrho)\left(\frac{x}{x_0}\right)^{\omega_m^0(\varrho)}. \tag{A.12}$$

The next task is to undo the $k^2 \to \varrho$ transformation, acheived through the integral

$$\phi_m(x,k^2) = \oint_{C-i\infty}^{C+i\infty} \frac{d\varrho}{2\pi i} \tilde{\phi}_m(x_0,\varrho)\left(\frac{x}{x_0}\right)^{\omega_m^0(\varrho)}\left(\frac{k^2}{Q_0^2}\right)^{\varrho}. \tag{A.13}$$

We anticipate performing a saddle point integration, and note that $\omega_m^0(\varrho)$ is maximal for some ϱ satisfing the implicit equation $\varrho = (\omega_m^0(\varrho)+1)/2$. Choosing an integration contour $\varrho = (\omega_m^0(\nu)+1)/2 + i\nu$ in order to collect the dominant piece of the integral,

$$\phi_m(x,k^2) = \int_{-\infty}^{\infty} \frac{d\nu}{2\pi} \tilde{\phi}_m\left(x_0, \frac{\omega_m^0(\nu)+1}{2} + i\nu\right)\left(\frac{x}{x_0}\right)^{\omega_m^0(\nu)}\left(\frac{k^2}{Q_0^2}\right)^{(\omega_m^0(\nu)+1)/2+i\nu}, \tag{A.14}$$

where $\omega_m^0(\nu)$ is given implicitly by the equation incorporating the symmeterized kernel,

$$\omega_m^0(\nu) = \bar{\alpha}_s\left\{2\psi(1) - \psi\left(\frac{m+\omega_m^0(\nu)+1}{2} + i\nu\right) - \psi\left(\frac{m+\omega_m^0(\nu)+1}{2} - i\nu\right)\right\}. \tag{A.15}$$

For $x \ll x_0$, the dominant contribution arises from the saddle point region where $\nu \simeq 0$, and so we approximate the integrand in Eqn. (A.14) about this point, noting that $\omega_m^0(\nu) \to -\infty$ for $|\nu| \to \infty$, allowing us to perform the integration. Close to $\nu = 0$ the component parts of the integrand will have the approximate forms:

$$\begin{aligned}
\left(\frac{k^2}{Q_0^2}\right)^{(\omega_m^0(\nu)+1)/2+i\nu} &\simeq \left(\frac{k^2}{Q_0^2}\right)^{(\omega_m^0(0)+1)/2} \exp\left\{i\nu \log\left(\frac{k^2}{Q_0^2}\right)\right\}, \\
\tilde{\phi}_m\left(x_0, \frac{\omega_m^0(\nu)+1}{2} + i\nu\right) &\simeq \tilde{\phi}_m\left(x_0, \frac{\omega_m^0(0)+1}{2}\right) \exp\left\{i\nu[\log\tilde{\phi}]'|_{\nu=0} - \frac{\nu^2}{2}[\log\tilde{\phi}]''|_{\nu=0}\right\}, \\
\left(\frac{x}{x_0}\right)^{\omega_m^0(\nu)} &\simeq \left(\frac{x}{x_0}\right)^{\omega_m^0(0)} \exp\left\{\bar{\alpha}_s \log\left(\frac{x}{x_0}\right) \psi''\left(\frac{\omega_m^0(0)+1}{2}\right)\nu^2\right\}.
\end{aligned}$$

These approximations allow us to put the integral into the standard form

$$\int_{-\infty}^{\infty} d\nu \exp\left\{-A\nu^2/2 + iB\nu\right\} = \frac{1}{\sqrt{2\pi A}} \exp\left\{\frac{-B^2}{2A}\right\}. \tag{A.16}$$

Where we identify the coefficients $A^{\rm CC}$ and $B^{\rm CC}$ as

$$\begin{aligned}
A^{\rm CC} &= [\log\tilde{\phi}]''|_{\nu=0} + \bar{\alpha}_s \log\left(\frac{x}{x_0}\right) \psi''\left(\frac{\omega_m^0(0)+1}{2}\right) \quad \text{and} \\
B^{\rm CC} &= \log\left(\frac{k^2}{Q_0^2}\right) + [\log\tilde{\phi}]'|_{\nu=0}
\end{aligned}$$

The final form for the unintegrated gluon distribution is then

$$\phi(x,k^2) \simeq \left(\frac{x}{x_0}\right)^{\omega_m^0(0)} \left(\frac{k^2}{Q_0^2}\right)^{(\omega_m^0(0)+1)/2} \tilde{\phi}_m\left(x_0, \frac{\omega_m^0(0)+1}{2}\right) \frac{1}{\sqrt{2\pi A^{\rm CC}}} \exp\left\{\frac{-(B^{\rm CC})^2}{2A^{\rm CC}}\right\}. \tag{A.17}$$

Appendix B

Numerical solution to the BFKL equation

Including a running coupling, a second significant source of higher order effects, spoils the scale invariance of the BFKL equation, and precludes an asymptotic solution. In this appendix we look at how a numerical solution to the modified BFKL equation incorporating a running coupling can be implemented by discretizing the unintegrated gluon as a polynomial series on a lattice in (x, k^2) space.

B.1 The BFKL equation with running α_s.

For simplicity we assume that the phenomenologically significant part of the unintegrated gluon distribution is given by the $m = 0$ azimuthally independent term. We take the running coupling, with scale of the order of the transverse momentum of the emitted gluons, under the integration in k'^2. For numerical stability, we treat together the real and virtual gluon pieces that regulate the $k^2 \longrightarrow k'^2$ limit. With a little algebraic manipulation we obtain a form for the modified BFKL equation appropriate for numerical analysis:

$$\phi(x, k^2) = \phi^{(0)}(x, k^2) + \int_x^1 d\xi \int_{k_0^2}^{k_f^2} dk'^2 \tag{B.1}$$

$$\left\{\mathcal{K}_{R'}(x,k^2,\xi,k'^2)\left[\phi(\xi,k'^2)-\phi(\xi,k^2)\right]-\mathcal{K}_{V'}(x,k^2,\xi,k'^2)\phi(\xi,k^2)\right\}.$$

Where $\mathcal{K}_{R'}$ is the kernel piece corresponding to real gluon emission *and* that part of the virtual emission kernel regulating it, and $\mathcal{K}_{V'}$ is the virtual emission term *less* this moderating piece.

$$\begin{aligned}\mathcal{K}_{R'}(x,k^2,\xi,k'^2) &= \frac{1}{\xi k'^2}\frac{\bar{\alpha}_s(k'^2)}{|1-k'^2/k^2|}\Theta\left(\frac{\xi}{x}-\frac{k'^2}{k^2}\right)\\ \mathcal{K}_{V'}(x,k^2,\xi,k'^2) &= \frac{1}{\xi k'^2}\frac{\bar{\alpha}_s(k'^2)}{(1+4k'^4/k^4)^{1/2}}-\frac{1}{\xi k'^2}\frac{\bar{\alpha}_s(k'^2)}{|1-k'^2/k^2|}\Theta\left(\frac{k'^2}{k^2}-\frac{\xi}{x}\right)\end{aligned}$$

These two kernel functions now contain the running coupling, $\bar{\alpha}_s(\mu_R^2)$, where we will take the scale to be of the order of the transverse momentum, $\mu_R^2 \simeq k'^2$.

The Chebyshev polynomials are defined on the interval $[-1,1]$ with the orthogonality condition

$$\int_{-1}^{1} dx\; T_n(x)T_m(x)(1-x^2)^{-1/2} = \delta_{nm}.$$

We map each of the integrations to the relevant domain through the change in variables

$$\sigma = -1+\frac{2\log(x/x_0)}{\log(1/x_0)} \quad \text{and} \quad \tau = -1+\frac{2\log(k^2/k_0^2)}{\log(k_f^2/k_0^2)}. \tag{B.2}$$

Eqn. (B.1) becomes

$$\begin{aligned}\phi(\sigma,\tau) = \phi^{(0)}(\sigma,\tau) + \int_{-1}^{1}d\sigma\int_{-1}^{1}d\tau|J| \\ \left\{\mathcal{K}_{R'}(\sigma,\tau,\sigma',\tau')\left[\phi(\sigma',\tau')-\phi(\sigma',\tau)\right]-\mathcal{K}_{V'}(\sigma,\tau,\sigma',\tau')\phi(\sigma',\tau)\right\},\end{aligned} \tag{B.3}$$

where $|J|$ is the jacobian of the change of variables. We can expand the function $\phi(\sigma,\tau)$ on $[-1,1]$ using Chebyshev polynomials

$$\begin{aligned}\phi(\sigma,\tau) &= \sum_{i,j=0}^{N-1} D_i(\sigma)D_j(\tau)\phi_{ij}\\ D_j(\sigma) &= \left(\frac{2}{N}\right)\sum_{i=0}^{N-1} v_i T_i(\sigma_j)T_i(\sigma),\end{aligned}$$

where $\sigma_j = \cos(2j+1)\pi/N$ and $\phi_{ij} = \phi(\sigma_i,\tau_j)$.

We now evaluate the left hand side of Eqn. (B.1) at the lattice node points (σ_i,τ_j), and expand the unintegrated gluon distribution functions under the integrations on the right hand

side using the Chebyshev polynomials. We obtain

$$\phi_{ij} = \phi_{ij}^{(0)} + \sum_{k,l=0}^{N-1} \phi_{kl} \int_{-1}^{1} d\sigma' \int_{-1}^{1} d\tau' |J| \tag{B.4}$$
$$\{\mathcal{K}_{R'}(\sigma_i, \tau_j, \sigma', \tau') \left[D_k(\sigma')D_l(\tau') - D_k(\sigma')\delta_{jl}\right] - \mathcal{K}_{V'}(\sigma_i, \tau_j, \sigma', \tau')D_k(\sigma')\delta_{jl}\}$$

and we have an equation for the ϕ_{ij} which will then allow us to reconstruct the full behaviour in the (x, k^2) space.

$$\phi_{ij} = \phi_{ij}^{(0)} + \sum_{k,l=0}^{N-1} \mathcal{M}_{ijkl}\phi_{kl}. \tag{B.5}$$

$$\mathcal{M}_{ijkl} = \int_x^1 d\xi \int_{k_0^2}^{k_f^2} dk'^2 \tag{B.6}$$
$$\left\{\mathcal{K}_{R'}(x_i, k_j^2, \xi, k'^2) \left[D_k(\xi)D_l(k'^2) - D_k(\xi)\delta_{jl}\right] - \mathcal{K}_{V'}(x_i, k_j^2, \xi, k'^2)D_k(\xi)\delta_{jl}\right\}.$$

With the kernel functions as given before. These integrals determining the $\mathcal{M}_{ijkl}$ can be evaluated using standard numerical integration algorithms, and Eqn. (B.5) inverted and solved to approximate the unintegrated gluon distribution.

References

[1] F. Halzen and A. D. Martin, Quarks And Leptons, *New York, USA: Wiley (1984) 396p.*

[2] A. D. Martin, Proceedings of the 1993 European school of high-energy physics ed. by N. Ellis and M. B. Gavela, Addendum, CERN yellow report no. 94-04.

[3] M. R. Pennington, Cornerstones of QCD, Rept. Prog. Phys. **46** (1983) 393.

[4] R. K. Ellis, W. J. Stirling and B. R. Webber, QCD and collider physics, *Cambridge, UK: Univ. Pr. (1996) 435p.*

[5] R. P. Feynman, Photon Hadron Interactions, W. A. Benjamin (1972).

[6] J. D. Bjorken, Phys. Rev. **179** (1969) 1547.

[7] M. Gell-Mann, Phys. Lett. **8** (1964) 214.

[8] G. Zweig, CERN-TH-412.

[9] A. C. Benvenuti *et al.* [BCDMS Collaboration], Phys. Lett. **B223** (1989) 485.

[10] J. J. Aubert *et al.* [European Muon Collaboration], Nucl. Phys. **B259** (1985) 189.

[11] A. D. Martin, R. G. Roberts, W. J. Stirling and R. S. Thorne, Phys. Lett. **B443**, 301 (1998).

[12] L. N. Lipatov, Sov. J. Nucl. Phys. **20** (1975) 94;
V. N. Gribov and L. N. Lipatov, Yad. Fiz. **15** (1972) 781;

[13] Y. L. Dokshitzer, Sov. Phys. JETP **46** (1977) 641;

[14] G. Altarelli and G. Parisi, Nucl. Phys. **B126** (1977) 298.

[15] G. Curci, W. Furmanski and R. Petronzio, Nucl. Phys. **B175** (1980) 27.

[16] W. Furmanski and R. Petronzio, Phys. Lett. **B97** (1980) 437.

[17] E. G. Floratos, D. A. Ross and C. T. Sachrajda, Nucl. Phys. **B129** (1977) 66; *ibid.* **B139** (1978) 545(E); *ibid.* Nucl. Phys. **B152** (1979) 493;
A. Gonzalez-Arroyo, C. Lopez and F. J. Yndurain, Nucl. Phys. **B153** (1979) 161;
E. G. Floratos, C. Kounnas and R. Lacaze, Nucl. Phys. **B192** (1981) 417.

[18] T. Kinoshita, J. Math. Phys. **3** (1962) 650;
T. D. Lee and M. Nauenberg, Phys. Rev. **133** (1964) B1549.

[19] E.A. Kuraev, L.N. Lipatov and V.S. Fadin, *Sov. Phys. JETP* **45** (1977) 199;
Ya. Ya. Balitzkij and L.N. Lipatov, *Sov. J. Nucl. Phys.* **28** (1978) 822;
J.B. Bronzan and R.L. Sugar, *Phys. Rev.* **D17** (1978) 585;
T. Jaroszewicz, *Acta. Phys. Polon.* **B11** (1980) 965.

[20] L.N. Lipatov, in Perturbative QCD, edited by A.H. Mueller *Singapore: World Scientific, (1989), 441p.*

[21] J. R. Forshaw and D. A. Ross, Quantum chromodynamics and the Pomeron, *Cambridge, UK: Univ. Pr. (1997) 248p.*

[22] L. V. Gribov, E. M. Levin and M. G. Ryskin, Phys. Rept. **100** (1983) 1.

[23] A. J. Askew, J. Kwiecinski, A. D. Martin and P. J. Sutton, Phys. Rev. **D49** (1994) 4402.

[24] J. Kwiecinski, A. D. Martin and P. J. Sutton, Phys. Rev. **D46** (1992) 921.

[25] L. H. Orr and W. J. Stirling, Phys. Rev. **D56** (1997) 5875;
L. H. Orr and W. J. Stirling, `hep-ph/9811423`.

[26] V. S. Fadin and L. N. Lipatov, Nucl. Phys. **B477** (1996) 767.

[27] V. S. Fadin, M. I. Kotsky and R. Fiore, Phys. Lett. **B359** (1995) 181;
M. I. Kotsky, V. S. Fadin and L. N. Lipatov, Phys. Atom. Nucl. **61** (1998) 641;

V. S. Fadin, R. Fiore, A. Flachi and M. I. Kotsky, Phys. Lett. **B422** (1998) 287;
V. S. Fadin and L. N. Lipatov, Phys. Lett. **B429** (1998) 127;
V.S. Fadin, hep-ph/9807527; *ibid.* hep-ph/9807528;
M. Ciafaloni and G. Camici, *Phys. Lett.* **B386** (1996) 341; *ibid.* **B412** (1997) 396; *ibid.* **B417** (1998) 390 (E); *ibid.* **B430** (1998) 349; M. Ciafaloni, hep-ph/9709390.

[28] D.A. Ross, *Phys. Lett.* **B431** (1998) 161.

[29] G.P. Salam, *JHEP* **9807** (1998) 019.

[30] G. P. Salam, hep-ph/0005304.

[31] J. Kwiecinski, A. D. Martin and P. J. Sutton, Z. Phys. **C71**, 585 (1996).

[32] J. R. Forshaw, P. N. Harriman and P. J. Sutton, Nucl. Phys. **B416** (1994) 739; *ibid.* J. Phys. G **G19** (1993) 1616.

[33] A. H. Mueller and J. Qiu, Nucl. Phys. **B268** (1986) 427;
J. Kwiecinski, A. D. Martin, W. J. Stirling and R. G. Roberts, Phys. Rev. **D42** (1990) 3645.

[34] S. Catani, M. Ciafaloni and F. Hautmann, Phys. Lett. **B242** (1990) 97; *ibid.* Nucl. Phys. **B366** (1991) 135;
J. C. Collins and R. K. Ellis, Nucl. Phys. **B360** (1991) 3;
E. M. Levin and M. G. Ryskin, Sov. J. Nucl. Phys. **53** (1991) 653.

[35] C. Adloff *et al.* [H1 Collaboration], Nucl. Phys. **B497** (1997) 3;
S. Aid *et al.* [H1 Collaboration], Nucl. Phys. **B470** (1996) 3;
M. Derrick *et al.* [ZEUS Collaboration], Z. Phys. **C72** (1996) 399.

[36] J. Kwiecinski, A. D. Martin and A. M. Stasto, Phys. Rev. **D56**, 3991 (1997).

[37] M. Mueller, Nucl. Phys. **B** (*Proc. Suppl.*) **18C** (1990) 125; *ibid.* J. Phys. **G17** (1991) 1443.

[38] J. Kwiecinski, A. D. Martin and P. J. Sutton, Phys. Lett. **B287** (1992) 254.

[39] J. Kwiecinski, A. D. Martin and P. J. Sutton, Nucl. Phys. **B** (*Proc. Suppl.*) **29A** (1992) 67.

[40] W. Tang, Phys. Lett. **B278**, 363 (1992).

[41] J. Bartels, A. de Roeck and M. Loewe, Z. Phys. **C54**, 635 (1992).

[42] J. Kwiecinski, S. C. Lang and A. D. Martin, Eur. Phys. J. **C6** (1999) 671.

[43] A. J. Askew, J. Kwiecinski, A. D. Martin and P. J. Sutton, Phys. Rev. **D47** (1993) 3775.

[44] C. Adloff *et al.* [H1 Collaboration], Nucl. Phys. **B538**, 3 (1999).

[45] J. Breitweg *et al.* [ZEUS Collaboration], Eur. Phys. J. **C6**, 239 (1999).

[46] J. Bartels, V. Del Duca, A. De Roeck, D. Graudenz and M. Wusthoff, Phys. Lett. **B384**, 300 (1996).

[47] E. Mirkes and D. Zeppenfeld, Phys. Rev. Lett. **78**, 428 (1997).

[48] M. Wobisch and T. Wengler, `hep-ph/9907280`.

[49] M. Wobisch, Talk given at the 5th International Workshop on Deep Inelastic Scattering and QCD, Chicago, 1997;
T. Wengler, Private communication.

[50] C. Adloff *et al.* [H1 Collaboration], Phys. Lett. **B462** (1999) 440;
T. Wengler, Ph.D. Thesis, University of Heidelburg, DESY-THESIS-1999-011.

[51] J. Binnewies, B. A. Kniehl and G. Kramer, Phys. Rev. **D52**, 4947 (1995).

[52] J. Kwiecinski, C. A. Lewis and A. D. Martin, Phys. Rev. **D57**, 496 (1998).

[53] G. Kramer and B. Potter, Phys. Lett. **B453**, 295 (1999).

[54] H. Jung, L. Jonsson and H. Kuster, Eur. Phys. J. **C9**, 383 (1999); *ibid.* `hep-ph/9811368`.

[55] G. A. Schuler and T. Sjostrand, Phys. Lett. **B376**, 193 (1996).

[56] V. Del Duca and C. R. Schmidt, Nucl. Phys. Proc. Suppl. **39BC** (1995) 137.

[57] A. J. Askew, Ph.D. Thesis, University of Durham, 1995. DESY-THESIS-1999-011.

[58] I. S. Gradshteyn and I. M. Ryzhik, Tables of Integrals, Series and Products, 5th edition. *London, UK: Academic Press (1981) 1160p.*